REPORT DOCUMENTATION PAGE

1. REPORT DATE (DD-MM-YYYY)	2. REPORT TYPE		3. DATES COVERED (From - To)
22-12-2008	FINAL		01/04/2007-31/07/2008

4. TITLE AND SUBTITLE	5a. CONTRACT NUMBER
Optical Correlation Based Pose Estimation Using Bipolar Amplitude Spatial Light Modulators	N/A
	5b. GRANT NUMBER
	FA9550· 07-1-0266
	5c. PROGRAM ELEMENT NUMBER
	N/A

6. AUTHOR(S)	5d. PROJECT NUMBER
Don A. Gregory and Gregory John Outerbridge II	N/A
	5e. TASK NUMBER
	N/A
	5f. WORK UNIT NUMBER
	N/A

7. PERFORMING ORGANIZATION NAME(S) AND ADDRESS(ES) AND ADDRESS(ES)	8. PERFORMING ORGANIZATION REPORT NUMBER
University of Alabama in Huntsville 301 Sparkman Drive Huntsville, AL 35899	N/A

9. SPONSORING / MONITORING AGENCY NAME(S) AND ADDRESS(ES)	10. SPONSOR/MONITOR'S ACRONYM(S)
Air Force Office of Scientific Research /RSL 875 N. Randolph Street, Room 3112 Arlington, VA 22203	AFOSR
	11. SPONSOR/MONITOR'S REPORT NUMBER(S) N/A

12. DISTRIBUTION / AVAILABILITY STATEMENT
Unlimited   AFRL-OSR-VA-TR-2012- 0028

13. SUPPLEMENTARY NOTES
N/A

14. ABSTRACT

Pose estimation using a bank of filters and a pose search algorithm approach was performed in both the digital and optical domains with sub-degree standard deviations in accuracy. The digital routine required less image processing than the optical method. This is because of the inability of the input SLM to achieve the resolution of the original digital image. The digital method is also capable of implementing complex composite filter designs. These filters generally performed poorly when directly optically implemented. This was not an unexpected result and was due to the limited dynamic range of the filter SLM and its amplitude only (real valued) modulation. Using Matlab as an interface to the correlator for the pose estimation routine and for the development of filter conversion algorithms and image processing of the 3D software generated training images allowed for the programming and generation of the filter bank and image loading sequence for bank of filters with search algorithm proof of concept. This allowed for programmable changes to filter designs or image processing to be implemented within a single software platform. This general approach to pose estimation is therefore more streamlined and less costly in time and hardware from development to simulation than other existing approaches.

15. SUBJECT TERMS
Pose estimation, optical correlation, pattern recognition, target tracking

16. SECURITY CLASSIFICATION OF: N/A			17. LIMITATION OF ABSTRACT	18. NUMBER OF PAGES	19a. NAME OF RESPONSIBLE PERSON
a. REPORT	**b. ABSTRACT**	**c. THIS PAGE**			Dr. Don Gregory
UU	UU	UU	UU	139	**19b. TELEPHONE NUMBER** (include area code) (256)824-2840

OPTICAL CORRELATION BASED POSE ESTIMATION USING BIPOLAR AMPLITUDE SPATIAL LIGHT MODULATORS

Final Report

Air Force Office of Scientific Research

Principal Investigator:

Prof. Don A. Gregory
Physics Department

Comprised primarily of a draft of a Dissertation by:

Gregory John Outerbridge II

Under the direction of Prof. Gregory

The University of Alabama in Huntsville

HUNTSVILLE, ALABAMA

2008

20120918134

TABLE OF CONTENTS

LIST OF FIGURES

LIST OF IMAGES

LIST OF TABLES

Chapter 1

Introduction

1.1. Pattern Recognition

Pattern recognition is a common part of everyday human life. Humans can recognize objects, people, familiar voices, have a sense for distance based on size relative to surroundings and so forth. Machine pattern recognition however must be performed using non-biological means and intuitions. The image of an object to be recognized must be captured either in a format, or converted to a format that is compatible with the rest of the recognition system. The systems today have evolved to include a host of instrumentation such as synthetic aperture radar (SAR) which uses microwaves to obtain high resolution images of the earth, laser scanning technology which uses backscattered information of an object as used in retinal scans, cameras that operate within the visible and/or infrared realm for tracking cooperative and non-cooperative targets and a host of other technologies that are employed for imaging specifics of an object. Optical pattern recognition, the technology focus of this research, has its roots in the experiments performed by Abbe (1) and later confirmed by Porter (2). Their experiments showed that by blocking spatial frequencies in the frequency spectrum of the Fourier transformed object, the resultant image obtained after inverse transformation had that spatial content removed. In their experiments, the vertical or horizontal spatial frequencies of a wire mesh (with vertical and horizontal structure) were independently blocked resulting in an

1

image with only horizontal or vertical structure respectively. Techniques have since been developed for image restoration and enhancement by selectively removing, dampening or altering the spatial frequencies associated with the undesired content. Pattern recognition on the other hand, where the task is to not alter but rather recognize the image, manipulates the frequency spectrum of the object using Fourier plane masks such that the Fourier transform of the product of the mask with the objects frequency spectrum results in a detectable correlation signal which signifies the presence of the object. This signal and a description of the types of masks used will be discussed in later chapters. Using Fourier transformations and Fourier plane masks to identify or extract information about an object using Fourier plane correlation is called Fourier optical processing and is commonly used in pattern recognition.

The advancement of Fourier optical processing came in 1964 when Anthony Vander Lugt, while working at the University of Michigan's Radar Laboratory, demonstrated using holographic techniques, the ability to control the phase and amplitude of light at the Fourier plane by creating the Fourier plane mask, also referred to as a filter mask (and here after referred to only as filter) using a holographic medium (3). Holograms record phase and amplitude information through the interference of two coherent beams of light, resulting in a complex transfer function. If the complex conjugate of the Fourier transform of the object under inspection is used as this transfer function, the filter is called a matched spatial filter (MSF) and results in a maximum valued peak in the correlation plane after inverse transformation. The MSF is commonly used in a template matching application. Template matching, in the simplest sense, is comparing a stored number of templates with the input scenery until a best match is

2

found. The template used which results in the optimum correlation signal is said to be matched to the object under inspection (the MSF will be discussed more in Chapter 3). Pattern recognition is therefore an application that is connected to pattern/image manipulation through the Abbe and Porter experiments with filters designed to give an object detection signal rather than an altered image of the object.

1.2. Optical Correlation

The mathematical foundation of optical correlation can be expressed using two functions $f(x)$ and $g(x)$, and defining their correlation as

$$f(x) \star g(x) = \int_{-\infty}^{\infty} f(x')g^{*}(x'-x)\, dx' \tag{1.1}$$

where $\star$ is the correlation operation and $g^{*}(x)$ is the complex conjugate of $g(x)$. For unit-energy signals, the correlation $f(x) \star g(x)$ reaches its maximum value of 1 only if the signals $f(x')$ and $g^{*}(x'-x)$ are identical for some value x. The maximum value of the correlation is thereby a measure of similarity between the functions $f(x)$ and $g(x)$. In optical pattern recognition, the convolution theorem is used to extend the above spatial representation of the correlation operation to the spatial frequency domain $F(v_x)$ using Fourier transforms. The convolution theorem states that the convolution of two functions can be computed by inverse transforming the product of their Fourier transforms. Stated mathematically, let $F(v_x) = \mathsf{F}\{f(x)\}$ and $G(v_x) = \mathsf{F}\{g(x)\}$ where $\mathsf{F}\{\ \}$ is the Fourier

3

transform operation, and the inverse Fourier transform $\mathsf{F}^{-1}\{\;\}$ are defined respectively as:

$$F = \mathsf{F}\{f\} = \int\limits_{-\infty}^{\infty} f(x)e^{-2\pi ix\cdot v}\,dx$$

$$and$$

$$f = \mathsf{F}^{-1}\{F\} = \int\limits_{-\infty}^{\infty} F(v)e^{2\pi iv\cdot x}\,dv$$

(1.2)

Then the convolution $f(x)\otimes g(x)$ is computed as

$$
\begin{aligned}
f(x)\otimes g(x) &= \int\limits_{-\infty}^{\infty} f(x')g(x-x')\,dx' \\
&= \int\limits_{-\infty}^{\infty} f(x')\left[\int\limits_{-\infty}^{\infty} G(v)e^{2\pi iv(x-x')}\,dv\right]dx' \\
&= \int\limits_{-\infty}^{\infty}\left[\int\limits_{-\infty}^{\infty} f(x')e^{-2\pi ivx'}\,dx'\right]G(v)e^{2\pi ivx}\,dv \\
&= \int\limits_{-\infty}^{\infty} F(v)\,G(v)\,e^{2\pi ivx}\,dv \\
&= \mathsf{F}^{-1}\{F(v)\,G(v)\}
\end{aligned}
$$

(1.3)

This is known as the convolution theorem (4). Similarly, the correlation of the two functions can be shown to be computed as

$$
\begin{aligned}
f(x)\star g(x) &= f(x)\otimes g^{*}(-x) \\
&= \mathsf{F}\{F(v)\,G^{*}(v)\}
\end{aligned}
$$

(1.4)

4

1.3. Optical Correlator System

An optical correlator uses the Fourier transforming properties of lenses and the correlation theorem to correlate an input scene with a reference image. For a coherent optical system, the illumination is a uniform plane wave produced by spatially filtering a monochromatic light source (typically a laser source) through a pinhole and collimating it using a lens. There are two primary types of coherent optical correlators in use; the Vander Lugt type and the Joint Transform type (5). Both systems use coherent illumination which allows the manipulation of the complex amplitude at the back focal plane of a Fourier transforming lens. The optical system architecture of the Vander Lugt type, as used in this research, is commonly referred to by many names including serial correlator, frequency plane correlator and 4-f correlator in reference to the optical path length from input scene to correlation plane being 4 times the focal length of the lenses used if they all have the same focal length f. Illustrated below, the input plane P_1 has image $f(x, y)$ a distance one focal length f in front of lens L_1. Lens L_1 Fourier transforms the image $f(x, y)$ into its spatial frequency representation $F(v_x, v_y)$ at the back focal plane P_2 where a filter $G^*(v_x, v_y)$ is inserted to manipulate the spectrum as it passes through that plane. Lens L_2 located one focal length f behind P_2 Fourier transforms the product $F(v_x, v_y)G^*(v_x, v_y)$ and the final output $c(x, y) = f(x, y) \star g(x, y)$ is produced at the back focal plane of Lens L_2 at plane P_3. It should be noted that the output at P_3 is inverted unless the coordinate axes at P_3 are reversed. This is a result of using two Fourier transforms instead of an inverse Fourier transform as the final optical transformation.

5

Input   Filter   Output

P_1 L_1 P_2 L_2 P_3

$f(x,y)$ $G^*(v_x,v_y)$ $c(x,y)$

← f → ← f → ← f → ← f →
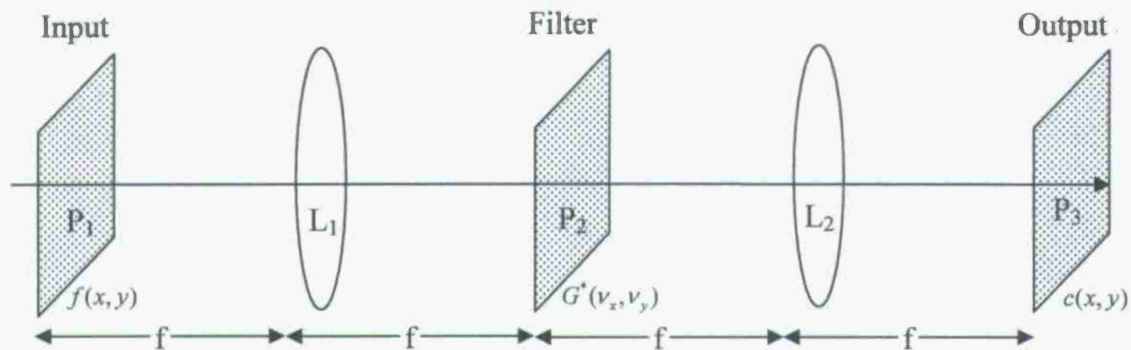
Figure 1-1 4f Optical Processor

The optical correlator has several advantages in image processing in comparison to digital computation. The 2-D FT operations performed by the lenses are done at the "speed of light", essentially an instantaneous operation. The point by point product $F(v_x,v_y)G^*(v_x,v_y)$ is also carried out at the speed of light and in a single step making the optical correlator a parallel processor that can compare an entire input scene to a reference image in three essentially instantaneous operations. Real time optical correlators however require input and filter devices to display the scene and filter images instead of static image and filter transparencies. So although the optical correlator's speed of operation is that of light, practically speaking the speed of the system is limited by the ability to write information at the input and filter planes and retrieve the data from the correlation plane. Nevertheless, optical correlation is much faster than a digital computer which uses the fast-Fourier transform (FFT) to perform the necessary transform calculations and compute the point by point product $F(v_x,v_y)G^*(v_x,v_y)$ serially instead of

6

in parallel. The number of computations (additions and multiplications) used in the FFT process is $N \log_2 N$, where N is equal to the total number of values (pixels) in the image and filter matrices. For a 256 x 256 data array, $N = 65536$ and the number of operations required is $N \log_2 N = 1,048,576$. In an optical correlator, the same number of operations is carried out at the speed of light ($\cong$ 1 ft/ns). In a correlator with an optical path-length of 1 ft, this corresponds to a throughput on the order of 10^{15} operations per second. As the resolution of the data array increases, the number of operations in digital computation also increases whereas in an optical correlator, the increase in the data array size does not affect the speed of the parallel computation. However, the speed of the bus to carry data to and from the correlator must scale according to the data array size to maintain the same speed characteristics as the original configuration.

There are several drawbacks to using real time optical correlators despite their high speed and computational parallelism. The transparencies used in the original work by Vander Lugt were created using holography. The interferometric techniques used to record the complex function $G^*(v_x, v_y)$ allowed an independent variation of magnitude and phase. A real time correlator uses input devices known as spatial light modulators (SLM's) which will be discussed further in the next section. It is sufficient here however to mention that SLM's cannot fully represent an arbitrary complex filter function and their realizable phase and magnitude values are usually coupled instead of being independently controllable. This requires designing filters that are constrained to the operating curves of the SLM. These devices can be binary in phase, single valued in magnitude (constant magnitude of 1) as in phase only modulators, phase magnitude coupled or amplitude only. The input SLM which displays the input scene also has a

7

limited dynamic range in grayscale values. This causes a reduction in resolution and a loss of image detail. The limitations of devices also include the photo-detector used in the correlation plane which detects the correlation function $c(x, y) = f(x, y) \star g(x, y)$. This measurement is an irradiance measurement which is the squared magnitude of the correlation therefore all phase information is lost in the detection along with polarity information (negative magnitudes), all of which are preserved in digital detection.

1.4. Spatial Light Modulators

An SLM is a device capable of modulating the amplitude and/or phase of an incident wavefront. The modulation of the wavefront is a function of position across the wavefront (6). The transmittance $T(x, y)$ of the SLM is controllable by the addressing mechanism. In an electrically addressed SLM, the control is an applied voltage. One method of electrical control is to arrange an array of transparent electrodes on each side of a planar electro-optic material placed between crossed polarizers and to apply an appropriate voltage to each cell in the array. $T(x, y)$ is then a function of prescribed voltage values at the (x, y) location of each cell. The transmitted intensity $I_t(x, y)$ through the SLM device is therefore related to the incident intensity $I_i(x, y)$ and the transmittance $T(x, y)$ by the product $I_t(x, y) = I_i(x, y) \bullet T(x, y)$. If the incident intensity $I_i(x, y)$ is a uniform collimated wavefront, then $I_i(x, y)$ can be treated as unity and $I_t(x, y) = T(x, y)$. The input scene or "image" $T(x, y)$ is then seen to be encoded onto the transmitted wavefront. The encoded image is therefore a conversion from a grayscale valued image to an array of prescribed voltage values $T(x, y)$ whose resultant

8

electro-optic/cross polarizer effect gives a transmitted intensity proportional to the grayscale value.

1.4.1. Liquid Crystals

The electro-optic material used in an electrically addressed SLM can be a liquid crystal (LC) layer which has both electrical and optical properties. LC's are elongated oblong shaped molecules that exist in a state of matter that lacks positional order (like a liquid) but has orientational order much like a crystal, hence the name *liquid crystal*. They respond to electrical forces in that an applied electric field induces a dipole moment in the molecule. The electric field interaction with the dipole imparts a torque to the molecule proportional to the field strength, causing it to twist into alignment with the applied electric field. They also respond to mechanical forces in that LC's will align with physical grooves purposely scratched (also known as rubbing) on a glass plate, often termed a director. If two glass plates are rubbed such that the resulting director axes are perpendicular and a thin layer of LC is sandwiched between them, the molecules will undergo a twist from one boundary to the next as they orient their axes to be aligned with the director at each interface.

There are three phases of LC's which define their type; Nematic, Smectic and Chiral. Nematic LC's have random molecular positions but their molecular orientations tend to be statistically oriented along a preferred axis. Smectic LC's also have orientational order but exist in layers that can slide on one another. Thus the Smectic types have positional order corresponding to the layer they are in. Chiral LC's undergo a helical rotation about an axis perpendicular to the director. Each layer of the helix is comprised of molecules whose long molecular axes are oriented parallel to one another

9

within the layer, and at a given angle with the direction of the axes of the molecules in the preceding layer (7). Twisted nematic LC's are nematic LC's which exhibit a twist much like that found naturally in the chiral type, but are a result of the mechanical forces imposed by the perpendicular directors of two glass plates with the LC material placed in between as mentioned above. Optically, LC's are inhomogeneous and anisotropic meaning that the permittivity of the material is not constant throughout the region of propagation and the optical properties are polarization dependant. For waves traveling perpendicular to the glass plates through the material along an axis defined as the z-axis, the normal modes are linear polarizations in the x and y directions which are parallel and perpendicular to the molecular orientation. Since the medium is anisotropic, the refractive indices are the extraordinary and ordinary indices n_e and n_o for the x and y polarization states. For a linearly polarized wave with vacuum wavelength λ_o traveling through a cell of thickness d, the wave retardation is expressed as $\Gamma = 2\pi(n_e - n_o)d / \lambda_o$. If an electric field is applied across the cell, the molecules will tilt in alignment with the direction of the field changing the extraordinary index n_e. The retardation of the cell then becomes a function of the tilt angle $\theta(V)$ which is itself determined by the strength of the applied voltage V. The retardation is then expressed as $\Gamma = 2\pi(n_e(\theta) - n_o)d / \lambda_o$. For a linear polarization of 45° in the x-y plane the cell is described as a voltage controlled variable wave retarder. For a wave completely polarized in the x direction, $\Gamma = 2\pi n_e(\theta)d / \lambda_o$ and the cell is described as a phase modulator. If the cell is designed such that $\Gamma = \pi$, it is referred to as half-wave retarder. When placed in between two cross polarizers at $\pm 45^\circ$, it becomes a voltage controlled amplitude modulator. An

10

amplitude modulator can also be constructed out of the twisted nematic LC cell (8). As already described, the molecules undergo a helical twist from one glass plate to the next. This twist angle is 90° if the directors of the plates are orthogonal to each other. If the director of the first plate (and therefore the orientation of the LC molecules) is oriented along the x-axis, the polarization of an incident linearly polarized wave (with polarization parallel to the director) will rotate following the helical twist of the molecules. The polarization exiting the LC cell will be polarized along the y-axis. The cell therefore acts as a polarization rotator. If an electric field is applied across the cell, the molecules tilt in the direction of the field (the z-axis) diminishing the polarization rotary power of the cell. If the applied electric field is strong enough, the tilt angle of the molecules (except for those at the glass surfaces) reaches 90° and the twisted state of the molecules is lost and the polarization rotary power of the cell is deactivated. If placed between crossed polarizers whose transmission axes are parallel to the directors of the plates, the cell acts as an optical switch, transmitting light when there is no applied field, and blocks the light when the field is applied. If a variable field is applied, the voltage controlled tilt angle $\theta(V)$ determines how much of the rotary power is lost and therefore partial polarization rotation does occur and the cell then acts as a voltage controlled amplitude modulator. A complete treatment of liquid crystal devices can be found in (7) and (9).

1.4.2. Bipolar Amplitude Spatial Light Modulators

The SLM's used in this research are deformed helix ferroelectric liquid crystal (DHFLC) devices. DHFLC is a Smectic C* type LC with a small molecular pitch. Ferroelectric LC's (FLC's) have a faster response time than the LC's mentioned due to an inherent electric dipole moment possessed by ferroelectric material. The dipole moment

11

interacts with the applied electric field switching the molecules orientation faster than the LC's that require an induced dipole moment. The switching speed of a FLC $(50 - 200\mu s)$ is therefore an order of magnitude faster than the nematic type (20ms) (9) . The helical arrangement of the DHFLC is similar to that of the twisted nematic LC which acts as a polarization rotator. The polarization rotation of the DHFLC works on the same principle but with the switching speed advantage of the FLC. The DHFLC therefore has the polarization rotary power to cause up to a 90° rotation in polarization which, when combined with an analyzer, gives an amplitude transmittance of $0 - 1$ for an incident beam linearly polarized along the director. For an incident beam polarized at 45 degrees to the director axis, the transmitted amplitude ranges from -.7 to .7 with zero to 2pi rotation respectively. This is further illustrated below in Figure 1-2. The black arrow represents the maximum rotation amount of the polarized field due to the modulation; the gray line is the transmission amount along the analyzer axis.

Illustration used from reference (46)
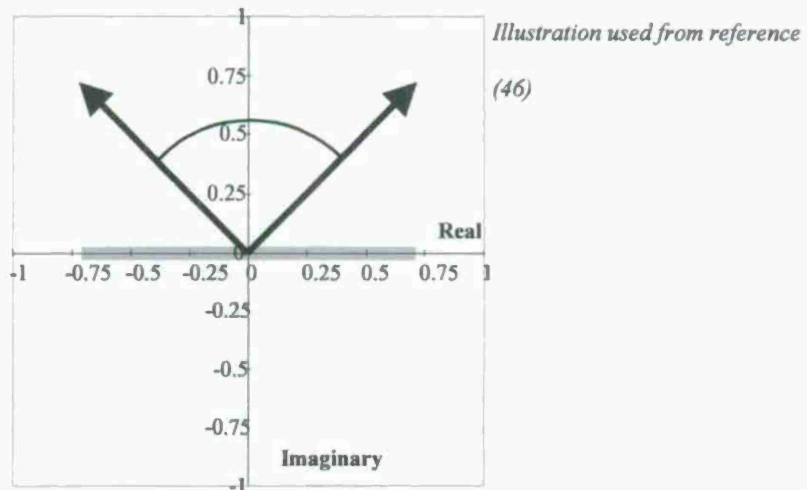
Figure 1-2 Transmission amplitude curve of bipolar DHFLC

The DHFLC device is therefore bipolar in phase and grayscale in amplitude due to a natural linear relationship between applied voltage and LC response. The rotation of the crystals as a response to applied voltage Vm is shown below in Figure 1-3.
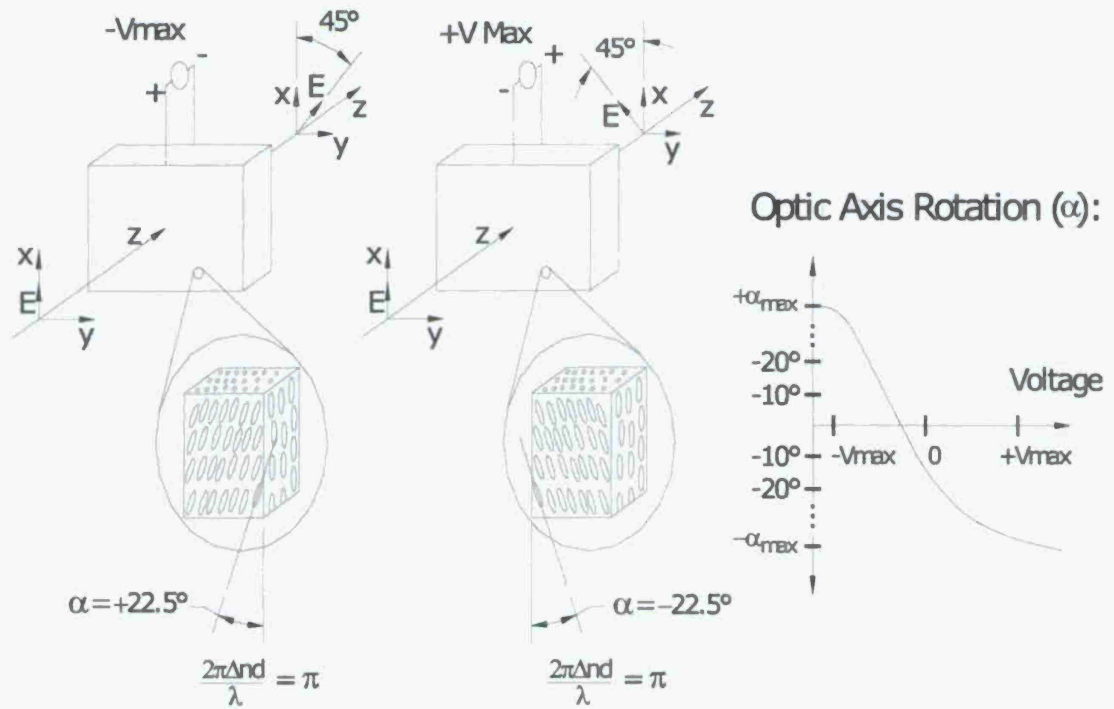
Figure 1-3 Illustration of polarization rotation of FLC to applied field.

Chapter 2

Pose Estimation for Autonomous Rendezvous and Docking

2.1. Science Motivation

The optical correlator has been tested extensively for target recognition and tracking in various military and industrial applications. Space applications are on the horizon, including pose estimation for autonomous rendezvous and docking (AR&D). An autonomous docking solution removes the potential for human introduced error, minimizing the risk to equipment and crew. The George W. Bush administration's 2004 NASA Space Exploration Initiative (10) which involves returning humans to the moon for lunar exploration will serve as a technological stepping stone for the human exploration of Mars and will elevate the importance of AR&D. Present rendezvous and docking technology requires on board human intervention for flight operations during the docking event and extensive ground control support at the Johnson Space Center in Houston. For a lunar operation, the signal delay from craft to ground support will be problematic and for proximity operations as far as Mars, the long signal delay makes Earth based intervention impossible. Therefore, an AR&D system, with less reliance on human participation (both ground and crew) is considered necessary to help accomplish the goals of the Exploration Initiative.

Signal delay however is not the only motivation for AR&D. The dangers associated with manual docking were manifested in 1997 when a 7 ton cargo ship crashed into the Russian MIR space station when it approached too fast to dock safely. The event

14

almost killed all on board after sending the MIR into a slow spin, piercing a module known as Specktr. This damage caused a leak in air pressure before it was sealed off. Power conservation required turning off all air conditioning and urine processing systems causing abrupt disruption to scientific experiments and the on board crew had to conserve oxygen by working in slow motion. This near tragic event brought the need for AR&D technology development to the forefront. Safety and technological demands for further space exploration make AR&D a necessary research element for space exploration.

AR&D technology will be a system integration of many technologies that allow a craft to identify another craft, determine its orientation with respect to that craft, and then approach the craft for either rendezvous or for docking. The identification of a craft and the determination of its pose is the focus of pattern recognition research which has been particularly developed in the digital domain. Research in correlation filters that can be used for pose estimation and target tracking have been developed by Juday et al. (11), Casasent (12), and many others (12-24). Treatments on optical considerations have been addressed by Mohalanobis et al (25) with actual implementation for target tracking being done by Chao (26-29). However, using an optical correlator for pose estimation has not been successfully implemented. With the development of high speed SLM's, the pose estimation problem of AR&D is a good platform for developing techniques that can possibly be extended to faster moving targets.

2.2. Statement of Research Problem

The scope of this research is to investigate pose estimation for AR&D using an optical correlator. For AR&D, the goal is to identify the target vehicle and estimate its rotational and translational state. The application of optical correlation techniques for

15

target tracking and pose estimation has been facilitated by the recent development of high-speed spatial light modulators (SLM). The techniques and filter designs that have been researched for digital methods do not have a trivial implementation when extended to an optical correlator and in some cases may not be possible due to real device limitations versus the flexibility allowed when working in the digital domain.

The demands of pose estimation using optical correlation exceed the demands of target tracking when considering filter design and implementation. In a pose estimation scenario, the peak values of the correlation measurements relative to one another are used to determine the pose of the craft. One method is based on modified composite filter designs that weight the poses in the training set such that the correlation peak value for each pose is predetermined in a way that a post processing algorithm can extract the pose based on the measurement values (16, 21). These techniques work well in a digital routine, however, optical correlation is more challenging. The range of values available for weighting the poses for optical composite filter designs is limited between 0 and 1 whereas digitally they can take on any value. In an optical correlator, the filter SLM does not have the ability to add gain to the signal. It operates between zero and full transmittance and therefore has a weighting ability of 0 to 1. Digitally, a large dynamic range of gain can be added in the filter design. Digital filters can also be, and usually are, complex valued and are not fully realizable on a real SLM device being limited by the operating curve of the SLM. Projecting a complex filter to an optimal real valued realizable filter has been investigated using minimum Euclidean distance (MED) projection to the operating curves of the SLM devices as explained in full detail by Juday (32, 33). However, the limited dynamic range of the SLM cannot accommodate the

16

dynamic range of the original digitally designed filter. Another drawback is the response

of the SLM not being active over all 8 bits which reduces the resolution of the image and

the available values for filter projection. The questions that will be addressed in this

research are:

1. Can an optical correlator be used for the pose estimation of a spacecraft?

2. If so, how does its implementation differ from a digital method?

3. What are the pros and cons of an optical correlation approach?

The first two questions will be addressed in the validation of pose estimation

techniques. The third question will be addressed in the final conclusions chapter where

the pros and cons of pose estimation will be discussed based on the results of the

correlation experiments.

2.3. Limitations of Research

This research will be limited to investigating optical pose estimation only. The digital

pose estimation methods discussed serve only to contrast the limitations between digital

and optical correlation approaches. Optically implementable filters created from the

digital models are presented to highlight the challenge of optical pose estimation using

composite digital filters platforms. New digital filter designs will not be investigated or

developed. The spacecraft docking scenario will be the docking of the space shuttle to

the international space station (ISS). The pose estimation will be done with zero clutter

in the background. Pose estimation with clutter and background noise will be suggested

as recommended future research.

17

Chapter 3

Correlation Filters

3.1. Matched Filter

The matched filter has played a significant role in pattern recognition due to its ability to detect signals corrupted with additive noise. An in depth treatment of the matched filter can be found in (25) whose outline of approach is summarized here. The matched filter maximizes the signal to noise ratio (SNR) performance criterion defined as:

$$SNR = \frac{\left|E\{C_{u,v}(0)\}\right|^2}{\text{var}\{C_{u,v}\}} \tag{3.1}$$

where $E\{\}$ denotes the expected value operation and "var" denotes the variance, $C_{u,v}$ is the correlation between the input signal u and the input signal plus additive noise n where $v = u+n$. Since the noise is assumed to have zero mean, $E\{C_{u,v}(0)\}$ is maximum when the input signal is u. The numerator of equation 3.1 can be further simplified as:

$$\left|E\{C_{u,v}(0)\}\right|^2 = \left|\left\{\int u(t)h(-t)dt\right\}\right|^2 = \left|\left\{\int U(f)H(f)df\right\}\right|^2 \tag{3.2}$$

where $U(f)$ and $H(f)$ are the Fourier transforms of the signal u and impulse response h. The input noise if is further assumed to be wide sense stationary (WSS) with power spectral density (PSD) $P_n(f)$. The output noise of a linear shift invariant (LSI) system

18

is also WSS and has PSD $P_n(f)|H(f)|^2$. The variance of a zero-mean random process is equal to the total area under its PSD (25), therefore the denominator of equation 3.1 can now be expressed as:

$$\text{var}\{C_{u,v}(0)\} = \int P_n(f)|H(f)|^2 \, df \tag{3.3}$$

The SNR can now be expressed in terms of $U(f)$, the FT of the signal $u(t)$, the PSD $P_n(f)$ of the additive noise $n(t)$, and the filter frequency response $H(f)$ by using Eqs. (3.2) and (3.3) in Eq. (3.1).

$$SNR = \frac{\left|\int U(f)H(f)df\right|^2}{\int P_n(f)|H(f)|^2 \, df} \tag{3.4}$$

In this form, the SNR can theoretically be infinite if $P_n(f)$ contains zeros in frequency regions where $U(f)$ does not and the filter magnitude is set to be non-zero in those regions. This generally does not occur so $H(f)$ must be chosen to maximize the SNR differently. The SNR can be re-written using the Cauchy-Schwarz inequality:

$$\left|\int A(f)B(f)df\right|^2 \leq \left[\int |A(f)|^2 df\right]\left[\int |B(f)|^2 df\right] \tag{3.5}$$

which has equality if and only if $A(f) = \beta B^*(f)$, where β is a complex constant. An upper bound on the SNR can be obtained by applying Eq. (3.5) to the numerator of Eq. (3.4) to get

19

$$SNR = \frac{\left|\int U(f)H(f)\,df\right|^2}{\int P_n(f)|H(f)|^2\,df} = \frac{\left|\int\left[\dfrac{U(f)}{\sqrt{P_n(f)}}\right]\left[H(f)\sqrt{P_n(f)}\right]df\right|^2}{\int P_n(f)|H(f)|^2\,df}$$

$$\leq \frac{\left[\int\dfrac{|U(f)|^2}{P_n(f)}\,df\right]\left[\int P_n(f)|H(f)|^2\,df\right]}{\int P_n(f)|H(f)|^2\,df} = \int\frac{|U(f)|^2}{P_n(f)}\,df = SNR_{max}$$

(3.6)

Because the PSD $P_n(f)$ is real and non-negative, taking the square root of it is allowed to obtain the above expression for maximum SNR which depends only on the FT of the signal $u(t)$ and $P_n(f)$. Using the equality condition $A(f) = \beta B^*(f)$ of Eq. 3.5, the maximum SNR can be obtained if and only if

$$\left[\frac{U(f)}{\sqrt{P_n(f)}}\right] = \beta\left[H(f)\sqrt{P_n(f)}\right]^* \Rightarrow H(f) = \alpha\frac{U^*(f)}{P_n(f)}$$

(3.7)

where α is any complex constant. For the case where the input noise is white noise, the PSD is a constant ($P_n(f) = N_0$) and the maximum SNR is simply

$$H(f) = \alpha_N U^*(f)$$

(3.8)

where $\alpha_N = \dfrac{\alpha}{N_0}$. This maximal-SNR filter is known as the matched filter (MF) since it is "matched" to the input signal by conjugating the FT $U(f)$. This is best interpreted optically where MF $H(u,v) = U^*(u,v)$ is inserted in the Fourier plane and input scenery $u(x,y)$ is in located in the input plane of the optical correlator. Incident on the filter is $U(u,v)$, the FT of $u(x,y)$. The filter $H(u,v)$ transmits a field proportional to UU^* which is purely real. Optically, this translates into the phase curvature of the

20

incident field being cancelled by the filter $H(u,v)$, which results in a transmitted plane wave. The second FT lens focuses the plane wave to a spot one focal length distance away at the correlation plane. The MF is therefore a *phase canceling* filter which results in a maximum SNR.

3.2. Inverse Filter

The inverse filter (IF) maximizes the peak to correlation energy (PCE) ratio defined as

$$PCE = \frac{\left|C_{u,v}(0,0)\right|^2}{E_c} \tag{3.9}$$

where E_c is the energy contained in the correlation signal $C_{u,v}$ defined as

$$E_c = \iint_{-\infty}^{\infty} \left|C_{u,v}(x,y)\right|^2 dxdy \tag{3.10}$$

The inverse filter is defined as

$$H(f) = \frac{U^{\bullet}(f)}{\left|U(f)\right|^2} \tag{3.11}$$

which can be seen to have a maximum PCE when the input scene is the reference object $U(f)$ (Incident on the filter is field $U(f)$ which transmits

$U(f) \cdot H(f) = \frac{U(f)U^{\bullet}(f)}{\left|U(f)\right|^2} =$ unity .) The FT of a constant is a delta function. The IF

therefore, by design, produces the sharpest correlation peaks and therefore the highest PCE. The IF however suffers serious drawbacks. Where the spectrum $U(f)$ contains zeros is ill defined in the IF and therefore cannot be realized. The IF also does not

21

account for any noise that may be in the signal and boosts the frequency components that have the worst SNR. The Wiener Filter defined as

$$H(f) = \frac{U^*(f)}{|U(f)|^2 + \frac{P_n(f)}{P_o(f)}}$$

(3.12)

where $P_n(f)$ and $P_o(f)$ are the PSD of the noise and object respectively, solves the above mention problems associated with the IF. It is defined for zeros in the spectrum of $U(f)$ and takes into account the noise that may be present in the signal. For high SNR, the WF reduces to the IF. For low SNR, it reduces to the matched filter $H(f) \approx \frac{P_o(f)}{P_n(f)} U^*(f)$.

3.3. Binary Phase Only Filter

The binary phase only filter (BPOF) is defined as

$$BPOF(u,v) = Sgn\{Re(POF)\}$$

(3.13)

where

$$Sgn(x) = \begin{cases} 1 & if \ x \geq 0 \\ -1 & if \ x < 0 \end{cases}$$

(3.14)

and the phase only filter (POF) is defined as

$$POF(u,v) = \frac{U^*(u,v)}{|U(u,v)|}$$

(3.15)

The BPOF has been studied extensively since its introduction (35-39) with one of its advancements being that of a threshold line angle (TLA) where the binarization axis is allowed to be arbitrarily rotated. Eq. (3.13) then becomes

$$BPOF(u,v) = Sgn\{Re(POF)\exp(i\beta)\}$$

(3.16)

22

where β is the TLA as illustrated below in figure 2.
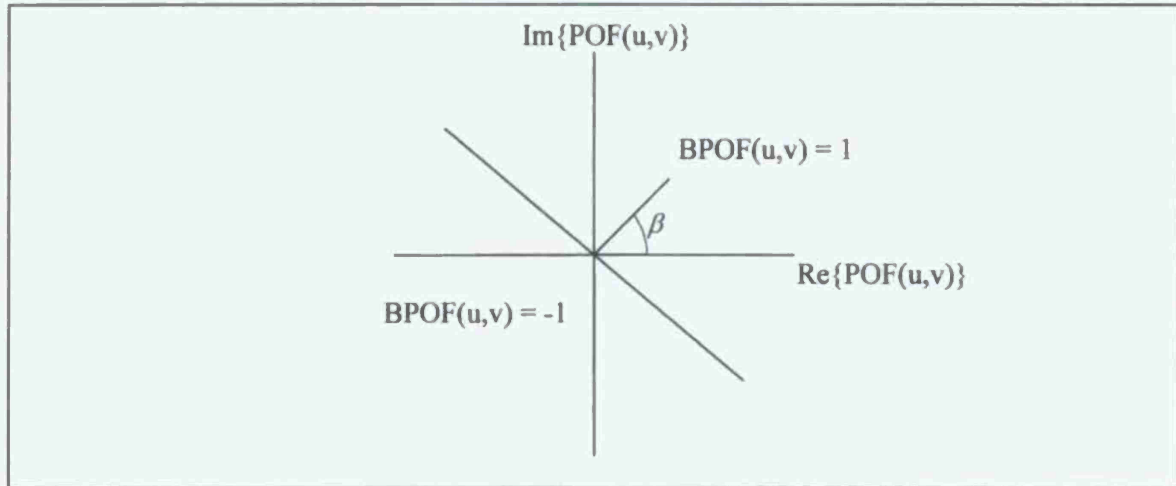
Figure 3-1 Illustration of TLA as used in BPOF

The optimum TLA usually involves a search algorithm and it is often selected as either

$0^0, 90^0$ or 45^0 corresponding to the real, imaginary, or real + imaginary parts of POF

respectively. BPOF's are light efficient since the transmission for all filter values are ± 1.

They are also easily computed requiring little processing time. They are of significant

interest in optical correlation since many SLM devices are binary in phase such as the

Magneto-Optic SLM (MOSLM) and can only implement BPOF's. A complete treatment

of BPOF and implementations using binary SLM's can be found in references (34-39).

3.4. Synthetic Discriminate Function Filters

One of the most useful advances in correlation filters has been the development of

synthetic discriminate function (SDF) filters. The idea behind an SDF is to weight the

frequency content of N training images used in its construction such that the peak

correlation of the filter with any image in the training set is determined by the weight

assigned. The general formulation (40) of an SDF filter H is given by the equation

23

$$H = X(X^+X)^{-1}u \qquad (3.17)$$

where $X = [x_1, x_2, x_3, ..., x_n]$ is the matrix whose columns x_i are the Fourier transforms of the N images in the construction set lexicographically rearranged as column vectors, + indicates complex conjugate transpose and u is a weighting vector containing the desired auto-correlation peak values for each image in the construction set. Typically, these filters are created to achieve invariance to distortions such as in-plane and out-of-plane rotations. This design has traditionally been geared more toward automated target tracking and recognition (ATR). In contrast to pose estimation, the ATR parameters of interest are the identification and tracking of the target as it translates through space. Pose estimation consists of identification, tracking, and the extraction of the 3 degrees of rotational freedom of the craft, hence making pose estimation a more difficult task requiring a different approach in filter design.

3.4.1. The Minimum Average Correlation Energy (MACE) Filter

The MACE filter (41) minimizes the correlation plane energy and produces very sharp correlation peaks over the recognition class. The correlation function c_i of the ith training image x_i with the filter h is denoted as $c_i = x_i \star h$. With the discrete Fourier transform (DFT) of the correlation function denoted as C_i, and X_i and H the DFT of the training image and filter respectively, the energy in the correlation plane is computed by

$$
\begin{aligned}
E_i &= \sum_{n=1}^{N} |c_i(n)|^2 = \frac{1}{N} \sum_{m=1}^{N} |C_i(m)|^2 \\
&= \frac{1}{N} \sum_{m=1}^{N} |H(m)|^2 |X_i(m)|^2
\end{aligned} \qquad (3.18)
$$

24

This can also be expressed using the vectorized image form as

$$E_i = H^+ D_i H \qquad (3.19)$$

where D_i is a diagonal matrix with the power spectrum of the image x_i as its diagonal

elements. The average energy in the correlation over all training images is then

$$E_{avg} = \frac{1}{N}\sum_{i=1}^{N} E_i \qquad (3.20)$$

The MACE filter minimizes this average energy function while constrained to having

peak amplitude $c_i(0) = X_i^+ H = u_i$. Its general formulation is given by the element by

element matrix operation

$$H = D^{-1}X(X^T D^{-1}X)^{-1}u \qquad (3.21)$$

where D is the average power spectrum of the N training images contained in X,

$$D = \frac{1}{N}\sum_{i=1}^{N} D_i \qquad (3.22)$$

The MACE filter is equivalent to a cascade of a whitening filter followed by a linear

associative memory (41).

Introduced by Kumar (16), focused MACE filters are designed to have one pose

as the "focus" of the filter, with the neighboring poses suppressed. The weighting of the

poses is Gaussian with the target pose at the origin. As the target vehicle deviates away

25

from the focus pose, the signal peak degrades in a controlled manner. The filters are designed to cover a wide range of poses with each filter focused on a particular pose. When presented with a target image, the peak response of each filter is collected in a vector. The shape of the vector elements is then compared to signature shape vectors of known poses generated during the design of the filter. The ability to generate a focused MACE filter with controlled responses after data compression for real valued implementable filters is a research challenge but the approach is worth consideration.

3.4.2. The Maximum Average Correlation Height (MACH) Filter

The MACH filter (25) is designed to maximize the correlation peak of the average of the training images. The MACE filter produces maximum peaks for images inside of the training set, but has decreased correlation energy for distortions of the image in between those used for the training set. The MACH filter maximizes the average correlation height of all distortions in and out of the training set. Its general formulation is given below. The FT of the vectorized training image set is again represented as $X = [x_1, x_2, x_3, ..., x_n]$, where column vectors x_i are the FT of each training image of size d x d lexicographically rearranged as vectors of size d^2. The correlation peak of the ith training image (found at the origin) with filter h is found as $c_i(0,0) = x^*_i h$. The Average Similarity Measure (ASM) is a metric used to characterize the tolerance in distortions and is defined as

$$ASM = \frac{1}{N} \sum_{i=1}^{N} \sum_{m}^{d} \sum_{n}^{d} \left| c_i(m,n) - \bar{c}(m,n) \right|^2 \tag{3.23}$$

26

where $c_i(m,n)$ is the correlation of the ith training image and $\bar{c}(m,n) = \dfrac{1}{N}\sum_{j=1}^{N}c_j(m,n)$ is

the average of the correlation surfaces of all training images. Using Parseval's theorem, the ASM can be rewritten as

$$ASM = \frac{1}{d\square N}\sum_{i=1}^{N}\sum_{m}^{d}\sum_{n}^{d}\left|C_i(m,n)-\overline{C}(m,n)\right|^2 \tag{3.24}$$

$\overline{C}(m,n)$ is referred to as the average correlation height (ACH) and is given by

$$ACH = M^{*}H \tag{3.25}$$

where $M = \dfrac{1}{N}\sum_{i=1}^{N}X_i$, the average of the training images FT's. The ASM can then be

derived to be

$$\begin{aligned}
ASM &= \frac{1}{d\square N}\sum_{i=1}^{N}\left|X_i^{*}H - M^{*}H\right|^2 \\
&= \frac{1}{d\square N}\sum_{i=1}^{N}H^{+}\left(X_i-M\right)\left(X_i-M\right)^{*}H \\
&= H^{+}\left[\frac{1}{d\square N}\sum_{i=1}^{N}\left(X_i-M\right)\left(X_i-M\right)^{*}\right]H \\
&= H^{+}SH
\end{aligned} \tag{3.26}$$

where $S = \left[\dfrac{1}{d\square N}\sum_{i=1}^{N}\left(X_i-M\right)\left(X_i-M\right)^{*}\right]$. By method of Lagrange Multipliers, H is

found to be

$$H = S^{-1}X(X^{+}S^{-1}X)^{-1}u \tag{3.27}$$

27

where u is a weighting vector used to weight the spectrum of the training set. For equal correlation peak weighting, $u = [1,1,...,1]$ and is of length X. A complete treatment on the MACH filter can be found in reference (25).

3.4.3. The Optimum Tradeoff Mach (OTMACH) Filter

The OTMACH Filter has been implemented with reasonable success by Chao (42) for target tracking applications. It optimizes several performance measures such as the ACH, ASM, ACE and output noise variance (ONV). The filter minimizes the energy function

$$
\begin{aligned}
E(H) &= \alpha(ONV) + \beta(ACE) + \gamma(ASM) - \delta(ACH) \\
&= \alpha CH + \beta DH + \gamma SH - \delta |M^* H|
\end{aligned}
\tag{3.28}
$$

The OTMACH filter that satisfies the minimized equation is

$$
H = \frac{M^*}{\alpha C + \beta D + \gamma S}
\tag{3.29}
$$

where C is the PSD of the additive input noise. M, D and S are as defined above and α, β, and γ are non-negative OT parameters. The selection of α, β, and γ values determine the performance behavior of the filter as required by application. For $\alpha = \beta = 0$, the filter behaves like a MACH filter which is good for tracking over a range of object distortions. For $\alpha = \gamma = 0$, the filter reduces to the MACE filter which gives sharp peaks but varies significantly over distortions of the object. For $\beta = \gamma = 0$, the filter reduces to a minimum variance (MV) SDF which was introduced by Kumar to reduce the output noise variance

28

in the correlation. For other values, the filter trades off performance in one area to be optimal in another according to the application need.

3.4.4. The Minimum Euclidean Distance Optimal Filter (MEDOF)

The MEDOF is designed to be implemented on SLM devices which have a limited realizable range of amplitude and phase values in which they operate. Therefore, the filter values must be fitted to this operating curve. The Minimum Euclidean Distance (MED) principle introduced by Juday (32) can be summarized as a mapping of the complex values of the filter design to the MED values of the complex operating curve of the SLM. For a binary phase-only SLM device, its MED mapping is given by:

$$H_{MED} = \begin{cases} +1, & \text{Re}(H) \geq 0 \\ -1, & \text{Re}(H) < 0 \end{cases} \tag{3.30}$$

where H_{MED} is the projected MED filter of H. This is illustrated below in Figure 3-3.
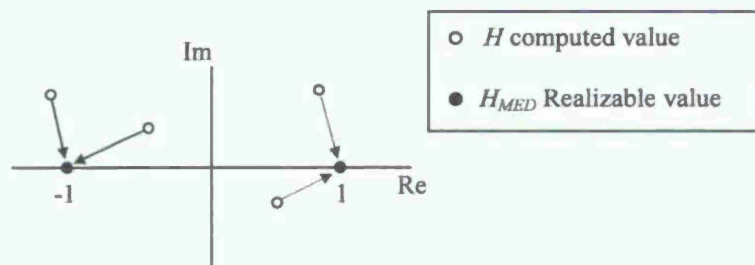
Figure 3-2 MED mapping for binary SLM

For a ternary SLM device, its MED mapping is:

$$H_{MED} = \begin{cases} +1, & +0.5 < \text{Re}(H) \\ 0, & -0.5 \leq \text{Re}(H) \leq +0.5 \\ -1, & -0.5 < \text{Re}(H) \end{cases} \qquad (3.31)$$

For a bipolar amplitude only SLM (AOSLM), the MED mapping is simply a projection

of the complex valued filter H to the real axis. This mapping is given as

$$H_{MED} = \begin{cases} +1, & +1 < \text{Re}(H) \\ \text{Re}(H), & -1 \leq \text{Re}(H) \leq +1 \\ -1, & \text{Re}(H) < -1 \end{cases} \qquad (3.32)$$

and is illustrated below in Figure 3-4.
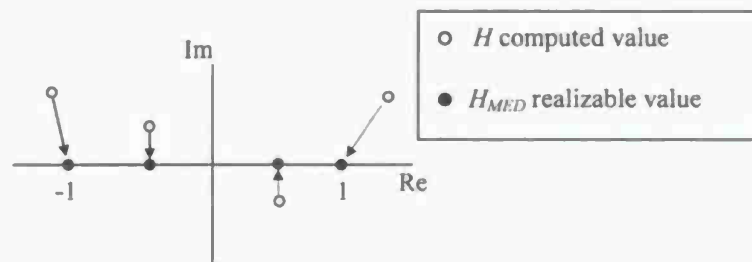
Figure 3-3 MED mapping for AOSLM

For coupled amplitude/phase response SLM's, the MEDOF is mapped to the complex

operating curve of the device by selecting the MED value of the SLM to the ideal

computed value. Because the dynamic range and the information capacity of the digitally

designed filter will have to be compressed to the allowed dynamic range limited to that

achievable by the SLM's, the MEDOF performance will decline rapidly with the number of training images used and limit the designer to additional constraints. The conversion from digital to a constrained realizable filter is one of the main hurdles in achieving optical correlation based pose estimation using composite filter designs.

3.5. Application of Correlation Filters

Composite correlation filters have been used extensively in the recognition of targets in synthetic aperture radar (SAR) imagery, in the growing field of biometric recognition, industrial automated inspection, space applications and defense. Images used for developing filters for detecting targets in SAR are mostly taken from the moving and stationary target recognition (MSTAR) database. The MSTAR database contains SAR image sets of particular targets at specific depression angles and multiple poses. These images are used to develop algorithms for ATR applications. Chao at the Jet Propulsion Laboratory (JPL) has reported success using OTMACH filters implemented on a grayscale optical correlator for ATR applications (41). The problem of pose estimation has been investigated initially by Juday where correlation targets are placed on the vehicles to aid in the pose estimation task. Castro (43) and Kumar (16) used weighted composite filter schemes whose complex designs may necessitate a digital implementation. Conversion from the digital to an optically implementable filter has been suggested by using binary phase only SDF's which binarize the digital filter. These binarization techniques have not been shown to result in filters whose performances are on par with the original complex digital version and have many constraints and drawbacks (44).

31

rendezvous simulations for test which eliminates hardware simulation cost. The software used to render the 2D images is © 3ds Max version 9. This software is designed for animation and has the necessary tools built in such that anticipated scenery and precise control of the movement of the craft can be simulated and tested. Various camera options are available with controlled lighting such that the docking event can be as closely simulated to match real world docking scenarios. This approach is not limited to spacecraft or space applications and is useful for the generation of training images for any target of interest in any environment.

The craft used for this research is the NASA space shuttle. The docking procedure with the International Space Station (ISS) will be reproduced and used as the test docking scenario for study. Mainly, pose estimation at the alignment ranges of 100m, 50m and 10m will serve as the test ranges for study. A simulated light and camera are situated inside the docking port of the ISS used to illuminate and view the craft as it approaches as shown in Image 3-1. Image 3-2 is a rendition of the shuttle at each alignment plane as it prepares to dock to the ISS as used in the research model. The tools available in the 3D software create a virtual laboratory where the effects of lighting, shadows, and camera can be designed into the filters which can compensate for these effects.

3.6. Research Contribution

The optical correlator has been successfully used for ATR but limited application to pose estimation has been performed. This research will investigate the viability of optical correlation based pose estimation using bipolar amplitude spatial light modulators. The approach taken will briefly highlight why weighted composite filters, one of the main components of digital pose estimation, cannot successfully be implemented on real devices which makes optical pose estimation more difficult to achieve and a more complicated problem to solve than the digital solution. However, this research effort will show that a brute force method using a bank of filters and a minimum amount of image processing can result in accurate pose estimates using a minimum amount of filters per estimation cycle. This research will also suggest a method of mapping large dynamic range digital filters to 8bit real valued SLM's resulting in higher signal to noise ratio correlations than non amplitude (bipolar) modulation.

The technical approach to this research will differ from that using cooperative correlation targets. The aim of this research is to develop pose estimation techniques of a craft by using only the geometry of the craft to obtain the correlation result. This goal of this approach introduces 3D simulation software generated images for the training set of the craft which can be generated by importing the CAD design of the craft or a simulated model of the craft. It is typical in research to obtain training images by using physical models of the desired target using cameras and rotation platforms in a laboratory environment. This requires equipment and setup time which adds overall cost to the project. Using 3D animation software to generate the training images for the correlation filters eliminates this hardware cost and also allows for the generation of docking and

32
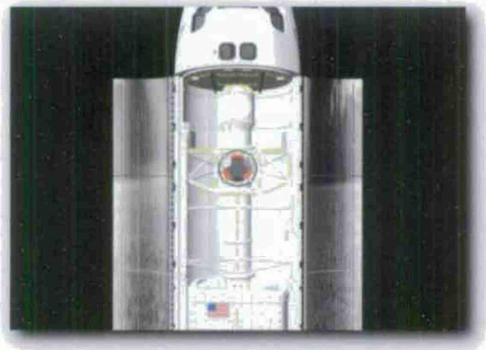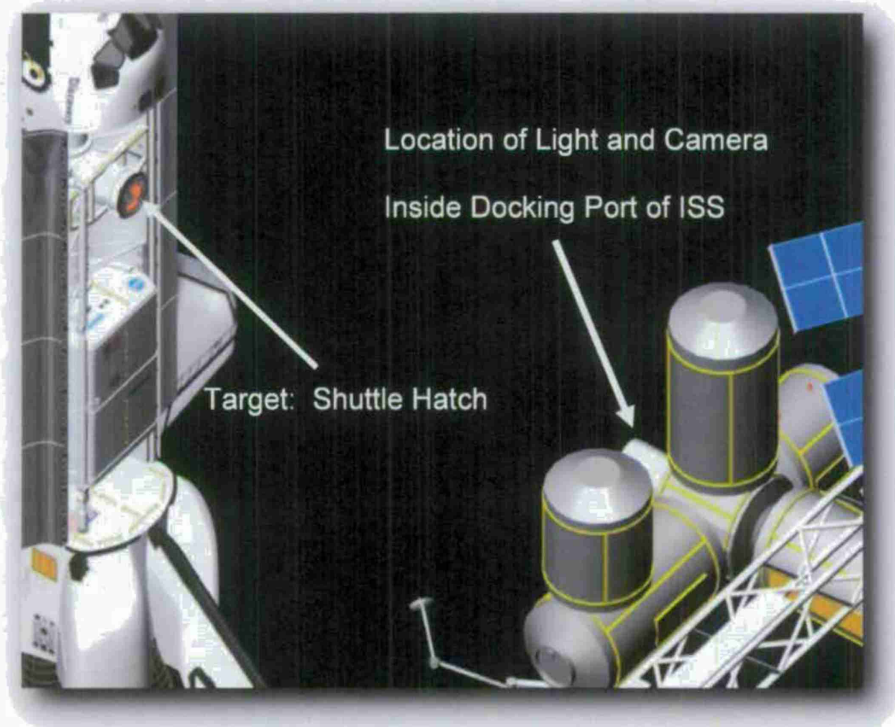
Image 3-1 3D pose estimation setup of camera and light (Top) and view from camera of illuminated craft (Bottom)
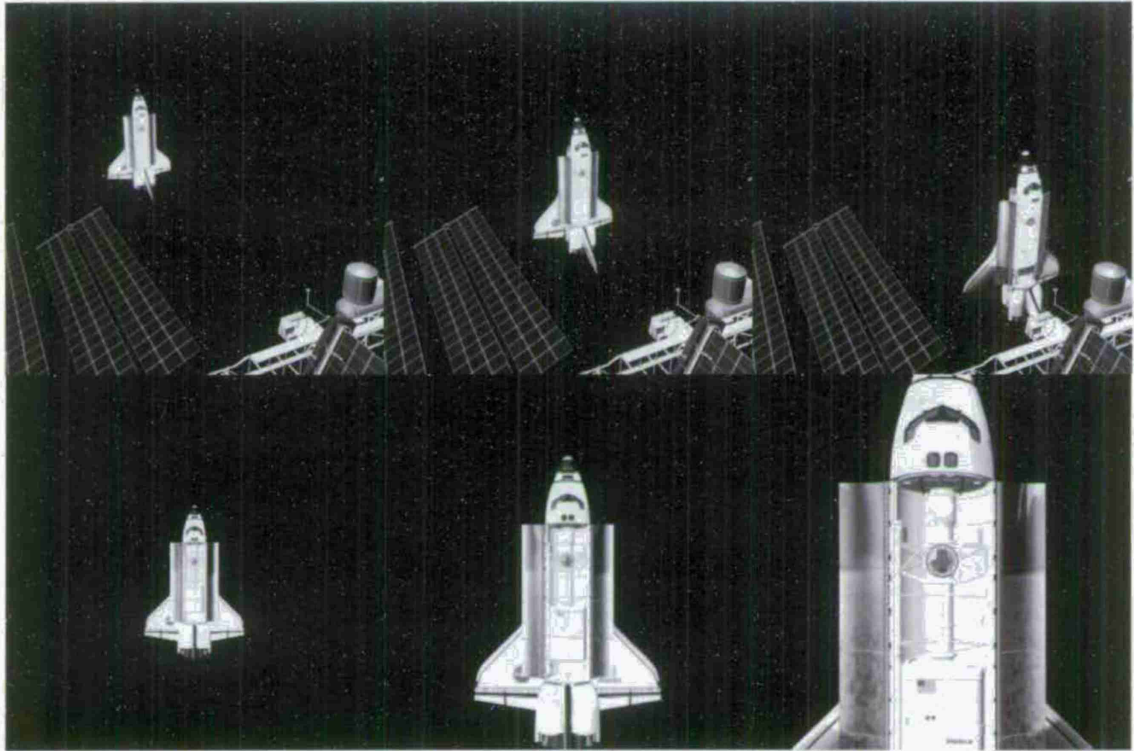
Image 3-2 Shuttle at each alignment plane (100m, 50m, and 10m left to right). Top row shows docking event from an angled view camera. The bottom row is the camera view as seen from the docking port on the ISS.

Chapter 4

Research Procedures

4.1. Research Methodology

The most ideal pose estimation method would involve the fewest correlations per detection using the fewest number of correlation filters. This is best achieved with composite correlation filters where information exists for many poses within a single filter. The characterization of the SLM's is the first step in preparing any filter design for optical implementation. The images and filters were mapped to the amplitude response of the input and filter SLM's respectively. After SLM characterization, filter designs using weighted composite filters are designed, mapped and the obtained correlations are compared to the digital results. To implement the composite filters, a linearly stretched histogram mapping of the filters to the filter SLM response as successfully used by Chao (45) is compared to logarithmically mapping the dynamic range of the filter design to the filter SLM response. This mapping has greater optical efficiency than histogram stretching and produces a higher signal to noise ratio than bipolar modulated filters.

After mapping the filters, the composite filter designs are tested for the ability to selectively weight poses in a controlled and predetermined manner. The inability to meet this goal resulted in using a bank of filters approach using logarithmically mapped (LM) distortion sensitive filters. To improve the discrimination ability of each filter, edge detection and image scaling were performed on the images with the results

36

compared to that obtained with no image preprocessing. The following sections outline the procedure of each validation technique.

4.2. Characterization of SLM's

Because both SLM's are amplitude modulators, the phase characteristics are already known to be bipolar and therefore only amplitude characterization is necessary for complete characterization of the SLM's. The SLM's are assumed to be uniform with a non-uniform approach considered if uniformity becomes a dominant issue in error analysis. The amplitude response of the input and filter SLM is characterized by doing the following:

Input SLM

1. Write full transmittance filter array to filter SLM (256x256 array with values of 0 or 255).

2. Increment input SLM array from 0 to 255 and record average intensity value in correlation plane.

Filter SLM

1. Write array on input SLM with four active pixels in the center (2x2) of the 256x256 array at full transmittance (255) values with the rest of the array at zero transmittance values. The Fourier transform of a small active region will fill most of the Filter SLM.

2. Increment the array values at the Filter SLM from 0 to 255 and record average intensity value in central region of correlation plane.

The amplitude response is proportional to the square root of the obtained values and the response of both input and filter SLM's are stored as vectors for further use.

37

4.3. Dynamic Range Compression

All filter designs are generated digitally and will have to be converted to an optically implementable filter design. This primarily involves dynamic range compression and mapping of the filter amplitudes to the amplitude response of the filter SLM. For the bank of matched filters approach, the initial filter designs used to test the search algorithm will be BPOF's since they are easily computed and implementable on an optical correlator. Dynamic range compression is required for the composite filter designs and for compression of the distortion sensitive Weiner filters. Both the linearly stretched mapping and the creation of LM filters are presented in more detail in Chapter 5 with the results of each as illustrations. The two methods were compared based on the following:

- Light efficiency of filter design
- Number of filter values on SLM modulation curve.
- Effect of compression technique on optical correlations

The light efficiency of the filter is calculated by normalizing the magnitude of the resultant filter to 1 after shifting the filter values such that zero optical throughputs correspond to a value of zero, and then summing the magnitude of all filter values. This is discussed further in Chapter 5.

4.4. Disqualification of Composite Filters

Using weighted composite filters for pose estimation requires the control of the peak values of selected poses. Equal correlation peak (ECP) filters ideally have a constant response for all poses in the training set. This is the ideal requirement for target tracking where the correlation peaks have to be present, but their individual values with

38

respect to one another does not have to be meaningful. However, pose estimation is a more challenging task by requiring the relative pose measurements to have a consistent predictable weighted response. Weighted correlation filters are therefore designed and tested as follows:

1. Design MACE, MACH and OTMACH filters with weighted correlation peaks.

2. Verify filter design using digital correlation and obtain peak values of weighted training set.

3. Create LM MED version of filters and obtain optical correlation results for each image in training set.

4. Compare optical results to expected digital results.

If the above validation had proven to be successful, then pose estimation techniques using weighted composite filters could have been investigated. The results shown in chapter 5 will cover the details of additional constraining factors not encountered digitally. The bank of matched filters approach was then considered as an alternative solution.

4.5. Validation of the Bank of Filters Technique with Pose Search Algorithm

The traditional bank of filters (BOF) approach requires generating a large number of filters and scanning through them until a correlation peak is found which is determined to be a best match according to the metric chosen (peak value, SNR, etc). This approach is more of a brute force approach but if an algorithm is used that intelligently selects and loads filters to be used to determine the pose, the number of correlation filters used per

39

cycle decreases dramatically. Because of the number of filters needed, a simple filter design that is sensitive to distortions and computationally efficient was chosen to prove the concept. The binary phase only filter (BPOF) has such characteristics and is computed by binarizing the phase φ of the MSF for each image in the filter bank according to equation (3.30). One method of taking the BOF approach with a pose search algorithm is as follows:

Consider a three dimensional pose space corresponding to the 3 degrees of freedom (DOF) pitch, yaw, and roll. For this illustration, the range for all axes of rotation will be limited to $0 - 4$ degrees for clarity and demonstration purposes. Pose points are constructed on the x, y, and z axes corresponding to the pose parameters pitch, yaw, and roll respectively. The cubic space describing this is shown below in Figure 4-1.
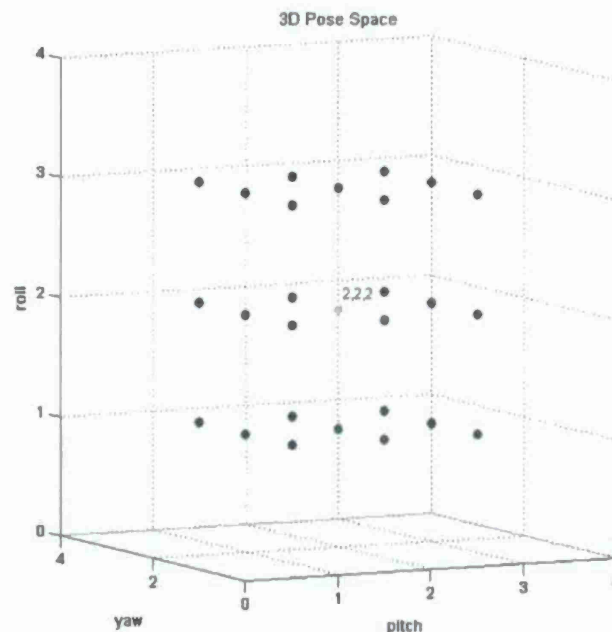
Figure 4-1 Illustration of 3D pose space as used in search algorithm

In this example, the craft was found oriented such that it corresponds to the pose point 2,2,2 (highlighted in center). On the next image capture the algorithm checks that pose parameter again in case the craft has not moved, and then checks the correlation of the image with the filters of the nearest neighboring poses (poses surrounding 2,2,2). The maximum correlation value found determines which direction the craft has moved and its new orientation. The steps involved are:

1. Perform Image Capture

2. Correlate image with each filter in bank storing maximum value of each correlation

$$Corr(k) = \max(I \star F_k)$$

$$I = \text{ Image from initial image capture}$$
$$F_k = k^{th} \text{ filter in bank of } N \text{ filters}$$
$$k = \{1,...,N\}$$
$$\star = \text{ correlation operation}$$

3. Determine pose with greatest correlation peak

4. Perform next image capture

5. Use algorithm to determine pose matrix
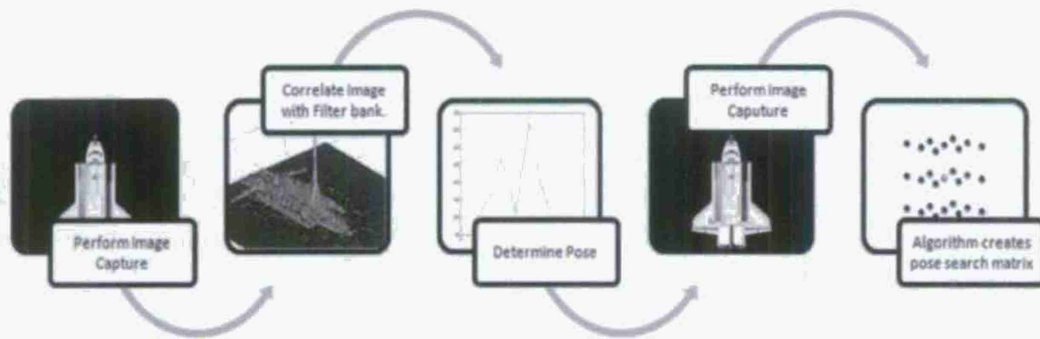
Figure 4-2 Initial steps in pose estimation routine

Once the pose of the craft has been determined from the initial image capture and the next image and pose search matrix has been acquired, a loop of the following steps is initiated:

1. Correlate captured image with filters from pose matrix

$$Corr(n) = \max(I_m \star F_n)$$

$I_m = m^{th}$ Image capture
$F_n = n^{th}$ filter determined by pose matrix
$n = \{1, ..., 27\}$
$\star$ = correlation operation

2. Determine pose corresponding to maximum correlation value found in Corr(k). Display and/or feed pose information to operator/craft.

3. Perform next image capture

4. Create new pose matrix

5. Repeat from step 6

42
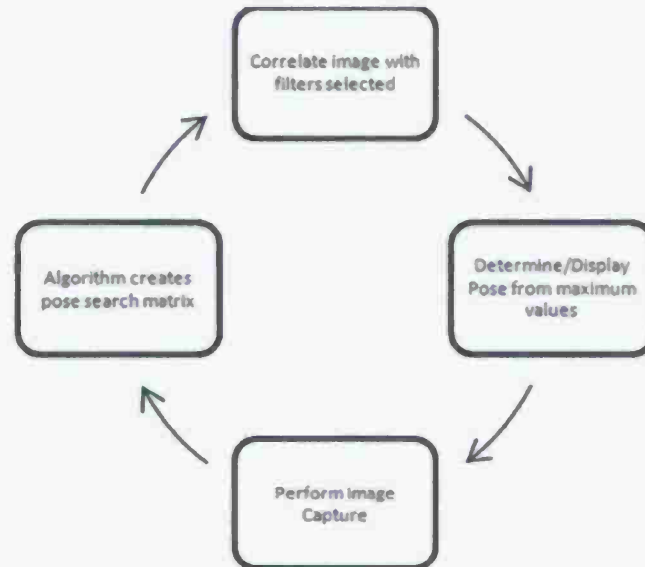
Figure 4-3 Pose estimation cycle

Each cycle produces a single pose estimate which is stored and compared to the actual pose of the craft. The validation set of poses found in Table 5-3 were used to test the algorithm. The standard deviations of the errors of the pose estimates is the data reported.

A statistical analysis of the performance of the algorithm described above was performed by generating a set of poses to be tested and comparing the SNR and the peak values of the autocorrelations with the 26 neighboring pose cross-correlations of each pose. Ideally, the autocorrelations will always exceed the value of the cross correlations in both SNR and peak value. However, it was found that the autocorrelation values are not of consistent magnitude and cross-correlations can at times exceed the autocorrelation peak value in a data set spaced apart in 1° increments. This requires filters very sensitive to distortions to be for the algorithm to select the correct pose. The statistical analysis of the algorithm is determined by evaluating a portion of its function. Specifically, the

43

correlation of a pose with its neighboring poses. However, the next pose input into the algorithm is not determined by the algorithm, but predetermined as the next pose in the set. The data will be composed of the autocorrelation and neighboring pose cross-correlations values. The value of each interest for each data set is the number of cross correlations that exceed the value of the autocorrelations. The ideal value which will produce zero error in the pose estimation of the training images in the set is zero.

4.6. Edge Detection

Preprocessing the images using edge detection will compensate for the limited dynamic range of the input SLM by writing only binary images with full transmittance values (255) where edges are present and zero elsewhere. However, the optical throughput decreases by having few values in the image as "on" so there is a tradeoff between optical throughput and the ability of optically reproducing images at the input SLM that were used in the construction of the filter. Edge detection was performed on the images using the Sobel method found in the Matlab image processing toolbox. The edge detected images were compared to the unprocessed images by doing the following:

1. Perform edge detection of selected images.

2. Create filters from edge detected images.

3. Perform algorithm performance test using edge detected images/filters

4. Obtain auto and cross-correlation peak values

5. Compare to statistics of unprocessed image correlations

44

4.7. Additive White Gaussian Noise Tolerance

The effect of adding noise to the images will ultimately determine the robustness of the pose estimation routine. For this exercise, additive white Gaussian noise (AWGN) is added to the image in increasing amounts such that the SNR decreases for each successive image set used for the pose estimations. The SNR used decreased from 20dB to 10dB. No effect on the pose estimation was found for SNR's higher than 20dB with 10dB being the lower threshold before the algorithm could not track the target. The AWGN algorithm in the Matlab image processing toolbox is used to measure the signal of the image and add the specified amount of noise to the images.

4.8. Instrumentation

Each SLM has drive electronics that consist of three boards: a PCI Driver Board, a DAC Board and an Op-Amp Board. The PCI Driver Board is located in the PCI slot of the computer. Image data is sent from the PC to the PCI Driver Board and then to the DAC Board. From the DAC Board, data along with the control signals is transferred to an Op-Amp Board where voltage levels are amplified to the level for which the SLM is designed. The input SLM is used to encode an image onto a coherent beam of light and the filter SLM is used to display the filter image. Each SLM is an electrically addressed 8bit 256x256 pixel array device that can operate at up to 4000 frames per second. The correlator, including the SLM's, was manufactured by Boulder Nonlinear Systems.

The overall layout of the correlator electronics and cabling is shown in Figure 4. The Laser/Power Board provides an external power source for the DALSA Camera and provides cabling routing out of the PC for the laser power and laser control signals. The Frame Grabber board retrieves the image from the camera and sends it to the software to

be displayed and analyzed. A diagram of the system and optical schematic is shown

below in figures 4 and 5 respectively.

Controller Unit

Camera
Trigger

Frame Grabber

Laser
Control

Laser/Power
Board

Input Driver
Board

Image
Sync

Filter Driver
Board

Power
SCSI

DAC
Module

Power
SCSI

DAC
Module

Data/Control

Camera Power

Laser Power

Laser Gain Control

Timing Sync

Cables

Optical Head

Dalsa
Camera

Laser

OP
AMP

Input SLM

OP
AMP

Filter SLM
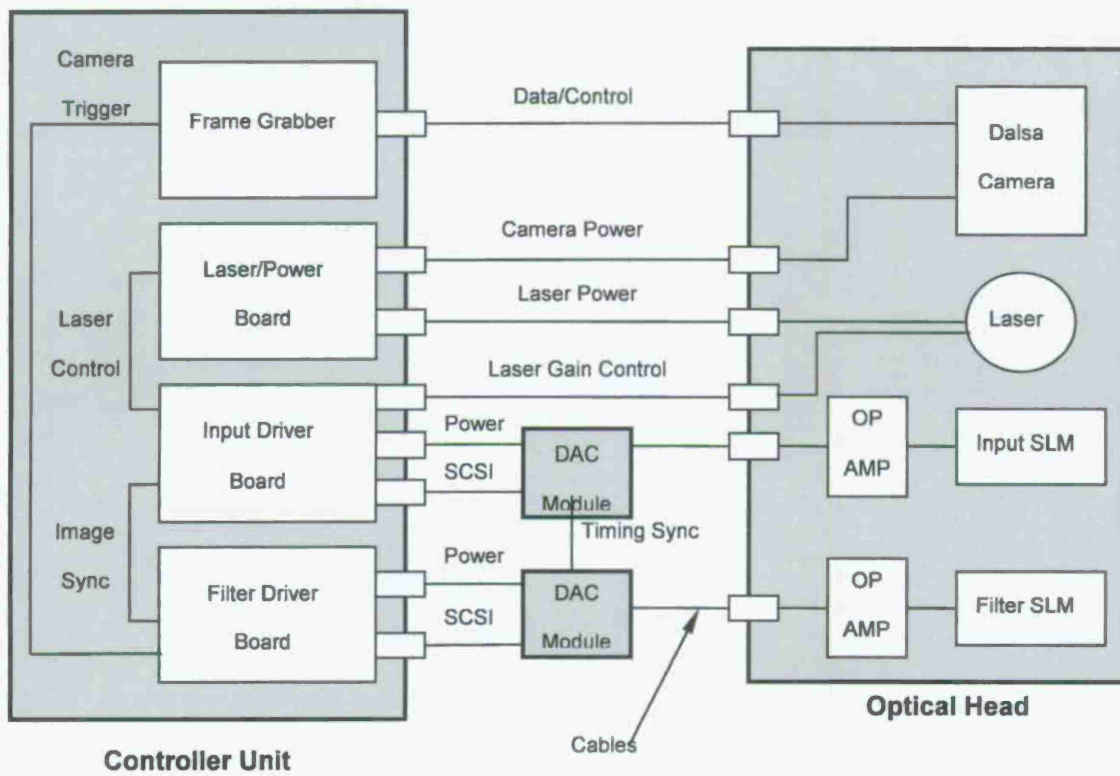
Figure 4-4 Optical Correlator System Diagram

Illustration taken from reference (46)

47
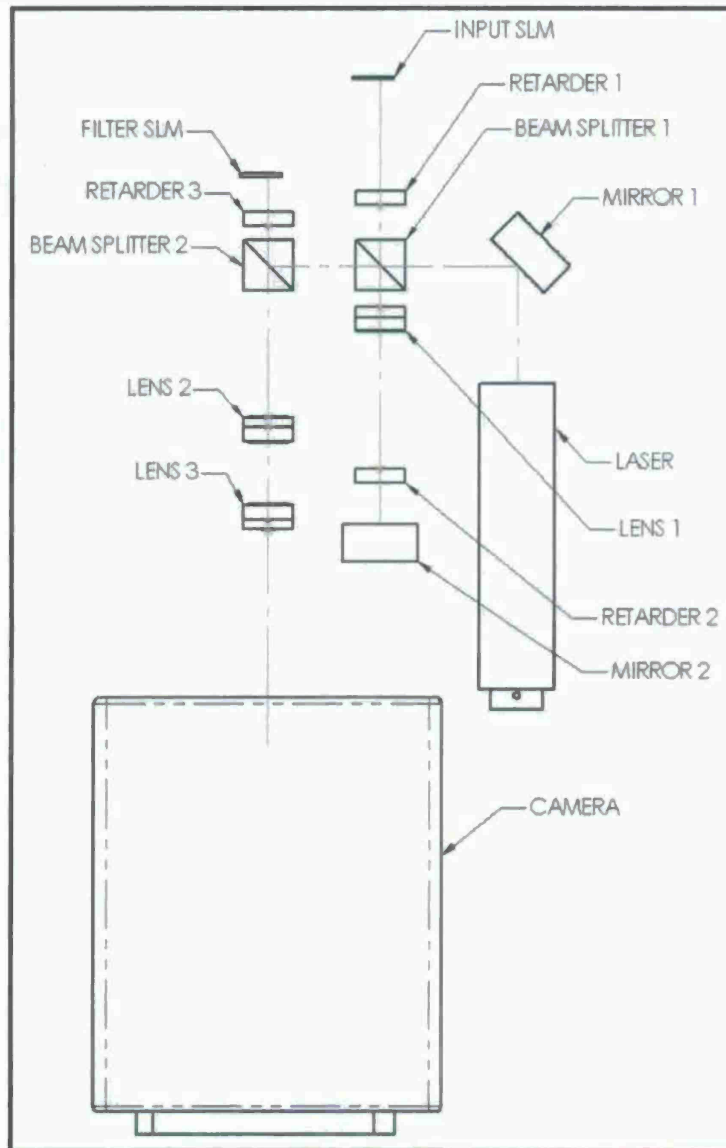
Figure 4-5 Optical Schematic of Correlator

The optical path through the correlator is as follows:

6. Linearly polarized light exits Laser and is reflected at folding Mirror 1.

7. Light is reflected at polarized Beam Splitter 1

8. Retarder 1 rotates light reflected from Beam Splitter 1 into optical orientation of Input SLM.

9. Input SLM reflects encodes image onto beam and reflects beam back to Retarder 1.

10. Retarder 1 rotates beam into the transmission axis of the polarized beam splitter 1.

11. Beam Splitter 1 transmits the beam through Lens 1, through quarter wave (QW) Retarder 2 and is then reflected at Mirror 2. The beam is reflected back through Retarder 2 and through Lens 1. The double pass through Lens 1 Fourier transforms the encoded image. The double pass through QW Retarder 2 rotates the polarization of the beam into the reflection axis of Beam Splitter 1.

12. The beam is reflected from Beam Splitter 1 to Beam Splitter 2.

13. Beam Splitter 2 reflects the beam through Retarder 3 which rotates the beam into the optical orientation of the filter SLM.

14. Filter SLM reflects the beam through Retarder 3 which rotates the beam into the transmission axis of Beam Splitter 2.

15. The beam is then passed through Lens 3 and Lens 4 and focused at the CCD camera. Lens 3 and Lens 4 perform the second Fourier transform.
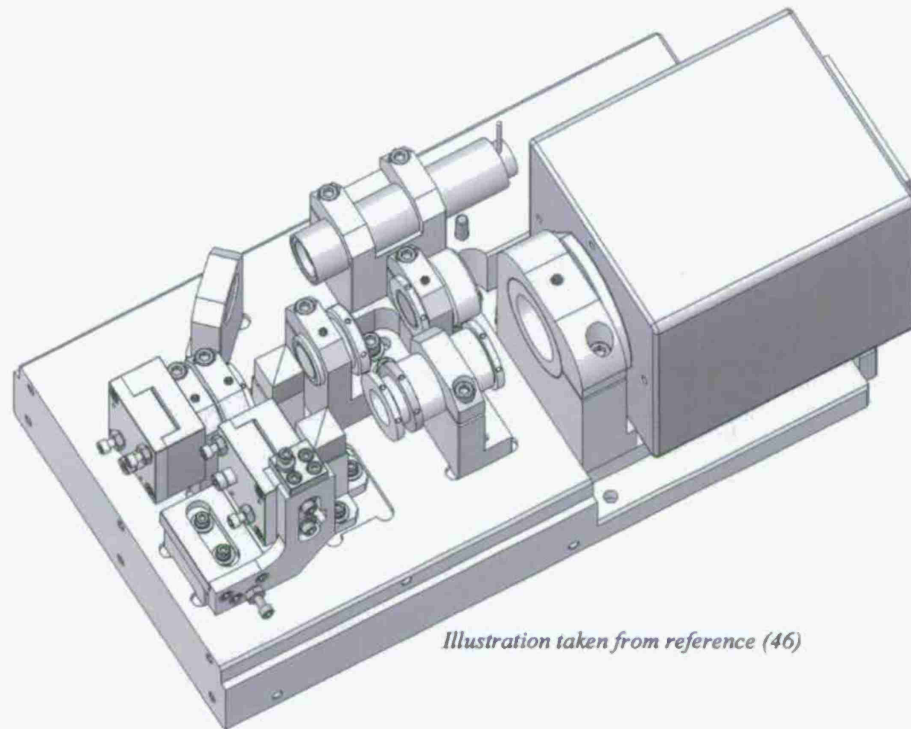
Illustration taken from reference (46)

Figure 4-6 3D Cad rendering of optical correlator

4.9. Summary

The validation of pose estimation using an optical correlator poses many

challenges for the use of composite filters. Although the composite filter approach is the

most desirable approach because it minimizes the number of correlation filters for

detection, it faced the most difficult challenges for implementation. Because the

correlation peak values must be meaningful with respect to all other measurement values,

the weighting of the image spectrum is the most critical in the digital filter design. This

weighting is made simpler for a training set with autocorrelation values that has

minimum variance from one pose measurement to the next. This difference makes pose

estimation a more difficult challenge than ATR where the correlation peaks must be

present, but not meaningful with respect to all previous or future measurement values.

The alternative bank of matched filters approach faces the same meaningful value challenge as the composite filter approach; however, the filter is designed to have a maximized correlation response at only one pose and sensitive to other pose distortions. The cross correlation values do not have to be meaningful with respect to the autocorrelation pose measurement or with respect to each other; they just have to be less than the autocorrelation pose measurement for the search algorithm to work. This simplicity compensates for the inability to weight the correlation response of each pose in a predictable and repeatable manner. The downside to this approach is the generation of a filter database which increases system storage requirements. The impact of this requirement to system cost has decreased significantly over the last decade as memory and disk storage has increased in data density while decreasing in cost per gigabyte. The use of a pose search algorithm that only loads neighboring poses decreased the number of pose measurements from the entire filter bank for each alignment plane to that which is comparable to theoretical pose estimation routines using weighted composite filters.

Chapter 5

Findings

5.1. SLM Characterization

The amplitude response of the SLM's was characterized as outlined in section 4.2. The mean of 30 data sets is plotted in Figure 5-1. The amplitude response for both the input and filter SLM's is proportional to the square root of the intensity values measured in the correlation plane. The mean values were then normalized to unity transmission after subtracting off the minimum offset value such that the magnitude of the transmission values ranged from 0 to 1. To prepare the filter response data to be used for mapping the digital filters to optically implementable filters, the polarity of the amplitudes was applied by multiplying the left hand side of the zero crossing by -1 to obtain the solid line plot. The dashed line plot is before polarity is applied.
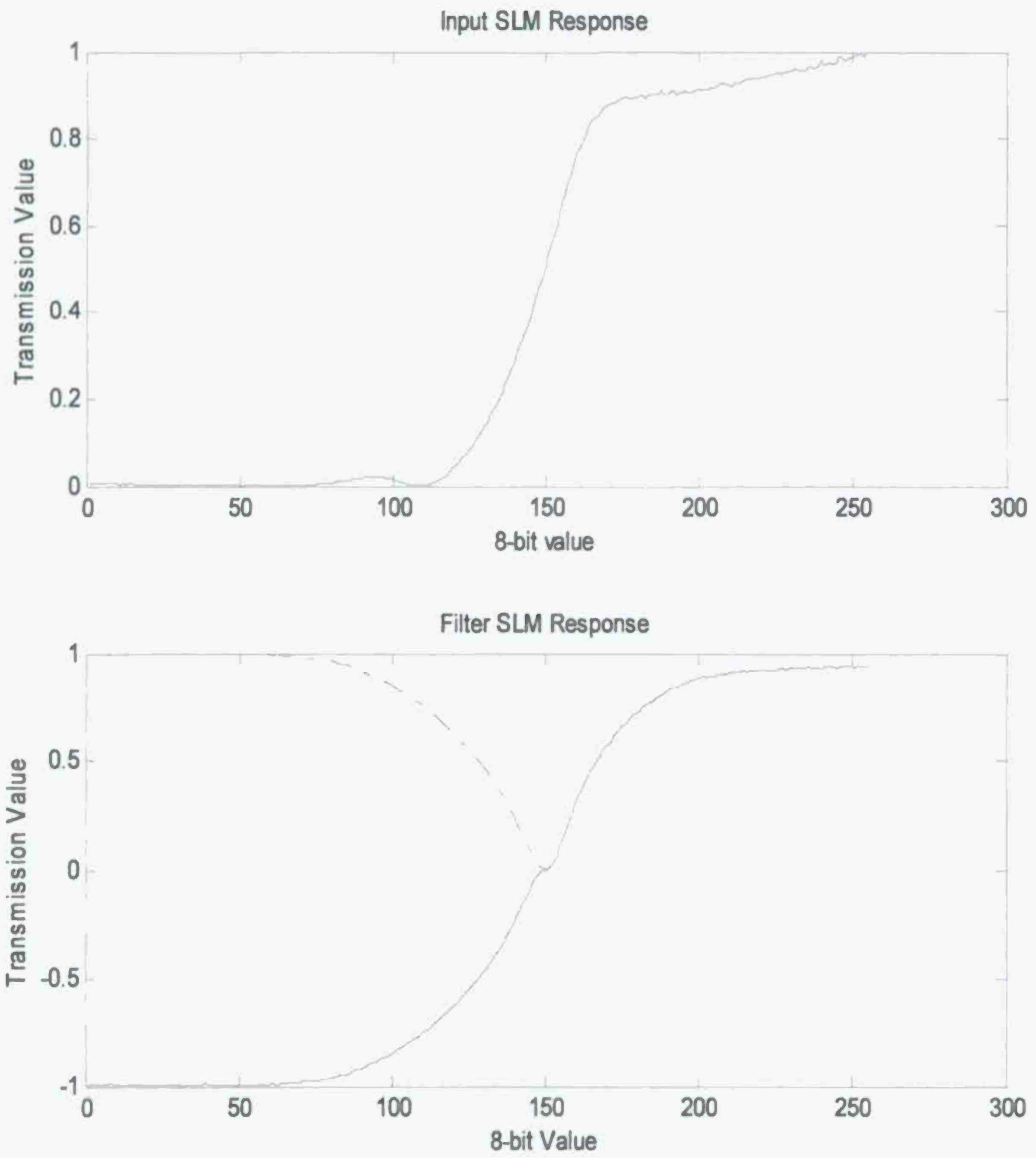
Figure 5-1 Input and Filter SLM Amplitude Responses

5.2. Dynamic Range Compression

To compress the dynamic range of the digital filters such that the filter values can be mapped to the filter SLM operating curve, a logarithmic compression technique is compared to a histogram linear stretched method as described by Chao (45). The MACE and MACH filters to be implemented have a dynamic range comparable to that of the Weiner filter which is essentially a MACE filter with a single training image. The Weiner filter was therefore the filter chosen to compare the dynamic range compression techniques. This dynamic range can be on the order of 10^5 to 10^6 which is beyond the dynamic range capability of the SLM's. The linearly stretched method is best described using histograms and refers to pushing the values outside of a given standard deviation out to the saturation value of maximum transmittance, and linearly stretching the rest of the pixel values towards that maximum (45). For the SLM's used in this research, the maximum values are the full transmittance values of 0 (for negative polarity) and 255 (for positive polarity). Creating a linearly stretched inverse filter is demonstrated in the following section.

5.2.1. Linearly Stretched Filter Generation

The training image used for the filter generation of a linearly stretched Weiner filter is the craft oriented with zero rotation on every axis located 50m away from the docking port and is shown below in Image 5-1. Inverse filter H_{IF} is generated using equation (3.11) then doing a MED projection onto the real axis and is therefore a real valued filter.
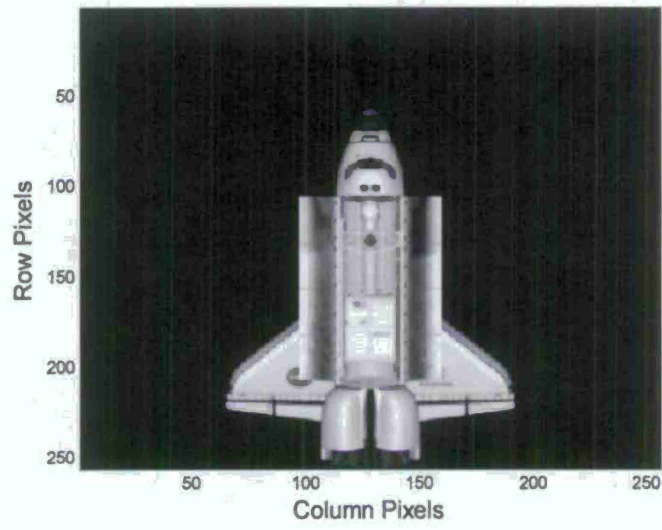
Image 5-1 Image of craft used for generation of H_{IF}
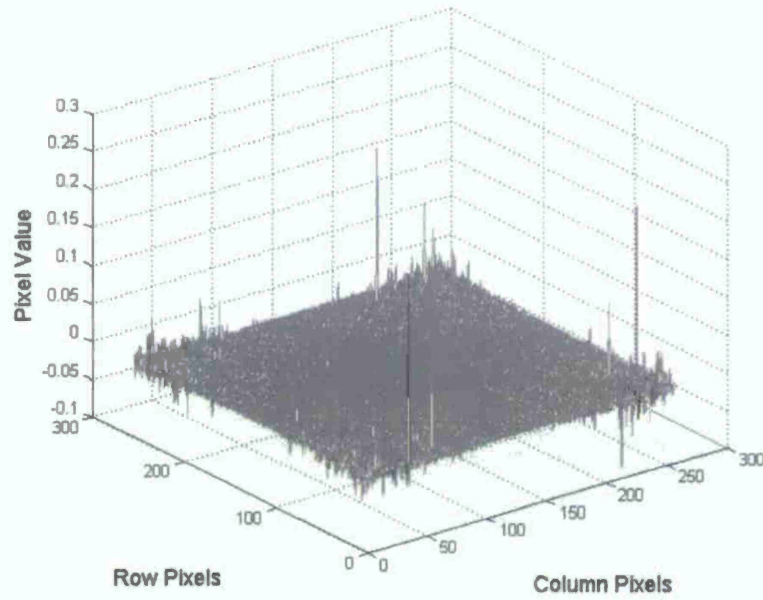
Figure 5-2 Inverse filter H_{IF}

The linearly stretched filter is created by stretching the histogram values of H_{IF} such that all values that lie outside $\pm3\sigma$ from the zero mean value are pushed into saturation and all values that are within $\pm3\sigma$ are then linearly stretched out to the maximum transmittance values. A histogram of H_{IF} before linear stretch, after a $\pm3\sigma$ stretch, and after a $\pm0.5\sigma$ stretch is shown in Figure 5-3 plots A,B and C respectively. The digital pixel values of H_{IF} are seen to be narrowly distributed about a zero mean transmittance as shown in Figure 5-3 A. After a $\pm3\sigma$ stretch of pixel values as seen in Figure 5-3 B, only a few pixels are at a full transmittance value of ±1. More pixels are seen to be at full transmittance after a $\pm0.5\sigma$ stretch as shown in Figure 5-3 C.
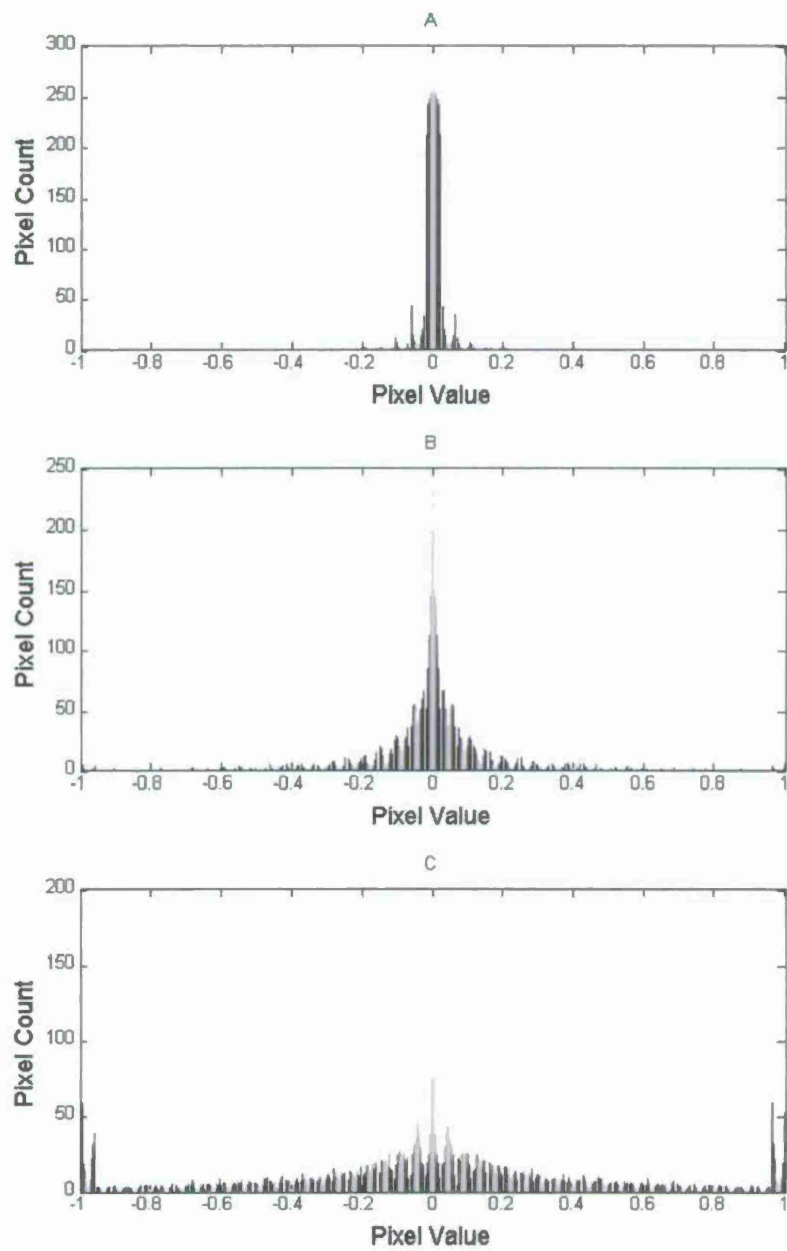
Figure 5-3 Histogram of H_{IF} with A) no linear stretch B) $\pm 3\sigma$ stretch and C) $\pm 0.5\sigma$

57

5.2.2. Logarithmic Compression Procedure

To reduce the number of near zero transmission values for the above filter H_{IF}, a logarithmic dynamic range compression is applied to the magnitudes of H_{IF}. This is performed by doing the following:

1. Take Logarithm of filter H_{IF} creating new filter H_{LF}.

$$H_{LF} = \log(H_{IF})$$

Since $|H_{IF}| \leq 1$, $H_{LF} \leq 0$ so the polarity information of the original filter is not retained. The dynamic range of the filters in this instance is:

$$H_{IF} \sqcap 10^6$$
$$H_{LF} \sqcap 6$$

Filter H_{LF} now gives a much narrower range to map to. Both filters are shown in Figure 5-4.

2. The standard deviation σ and mean value μ of H_{LF} is then calculated. In this instance,

$$\sigma = .5625$$
$$\mu = -2.5668$$

The filter response R_F is scaled such that $|R_F|$ spans 6σ of the values of the reduced dynamic range of H_{LF}.

3. Scale R_F to cover $\pm 3\sigma$ of filter H_{LF}

$$R_L = 6\sigma \sqcap |R_F|$$
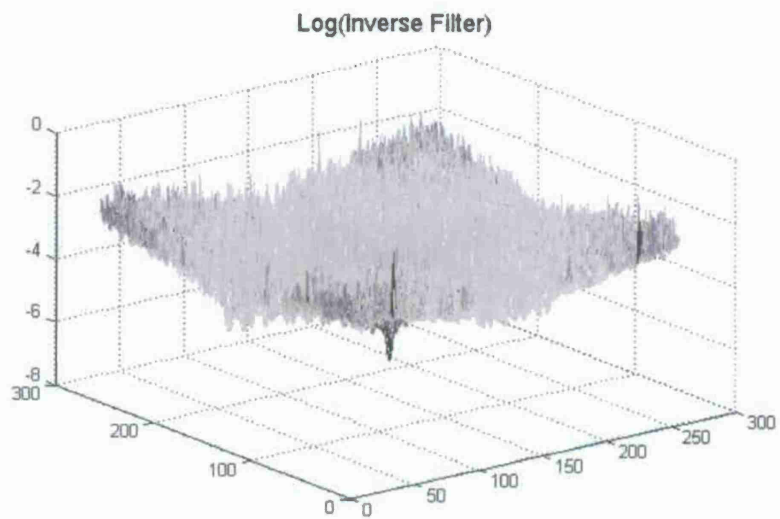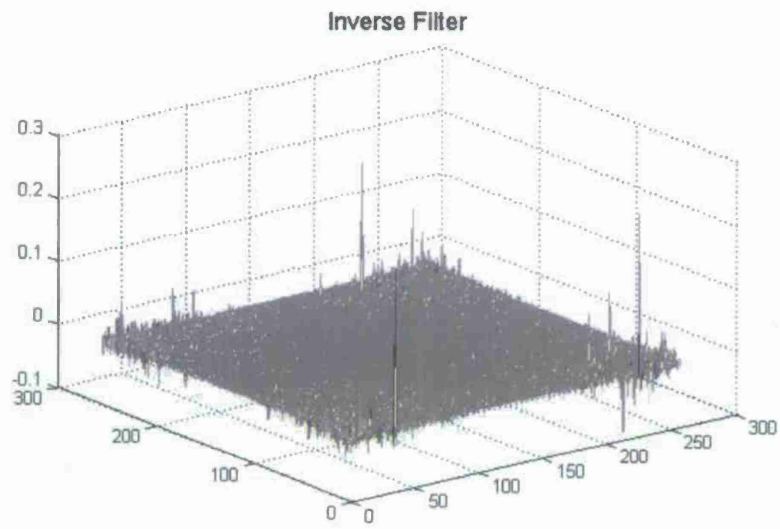
Figure 5-4 3D Filter plots. Top: Inverse Filter Bottom: Logarithm of Inverse Filter

The vector used for the mapping of H_{LF} must have values that coincide with the desired

overlap. That is, R_L must be shifted such that its values overlap the desired range of

values in H_{LF}. R_L and the shifted mapping vector R_{MED} are shown in Figure 5-5.

4. Compute shifted mapping vector R_{MED} as:

$$R_{MED} = R_L - |\mu| - 6\sigma$$
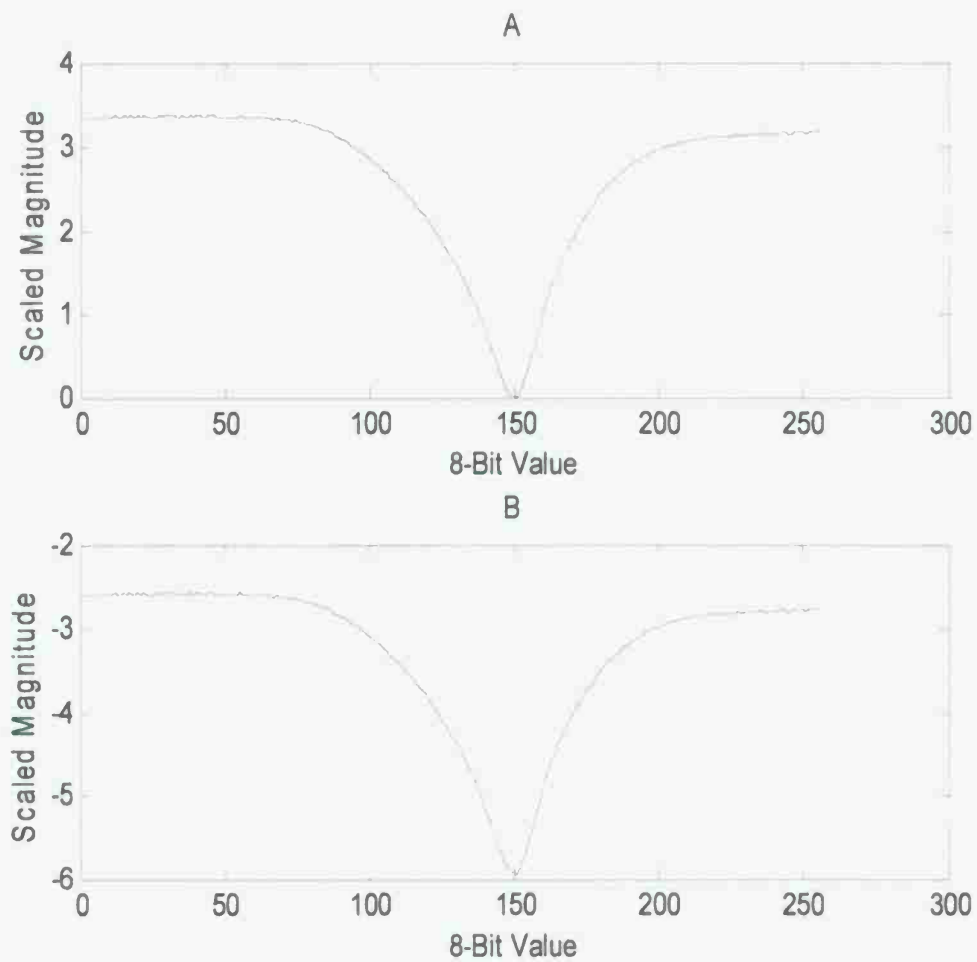
Figure 5-5 R_L (top) and the shifted mapping vector R_{MED} (bottom)

The values of H_{LF} are then mapped to R_L by choosing the MED of H_{LF} to R_L. The polarity of the original filter H_{IF} must be taken into consideration when doing the mapping.

5. Map H_{LF} to R_L by doing the following:

   a. If $H_{IF}(m,n) < 0$, then $H_{LF}(m,n)$ is mapped to the 8-bit values of

      R_{MED} corresponding to negative polarity. These are the 8-bit values to

      the left of the zero transmission value in R_L.

   b. If $H_{IF}(m,n) \geq 0$, then $H_{LF}(m,n)$ is mapped to the 8-bit values of

      R_{MED} corresponding to positive polarity. These are the 8-bit values to

      the right of the zero transmission value in R_L.

The optical and digital histograms for filter H_{LF} are shown in Figure 5-6. The transmission of H_{LF} and the transmission of a 1σ linearly stretched filter H_{LS} are shown in Image 5-2. The amplitude transmission of each filter is calculated by:

$$T = \frac{\sum\limits_{m,n} |H(m,n) \cdot F(m,n)|}{\sum\limits_{m,n} |F(m,n)|} \tag{5.1}$$

where the incident field F is the FFT of the input image I.

$$F = FFT(I)$$
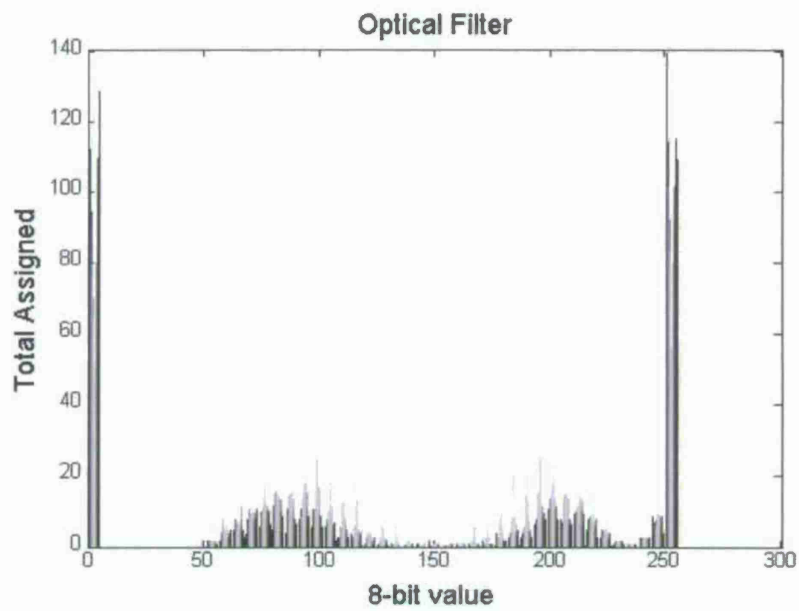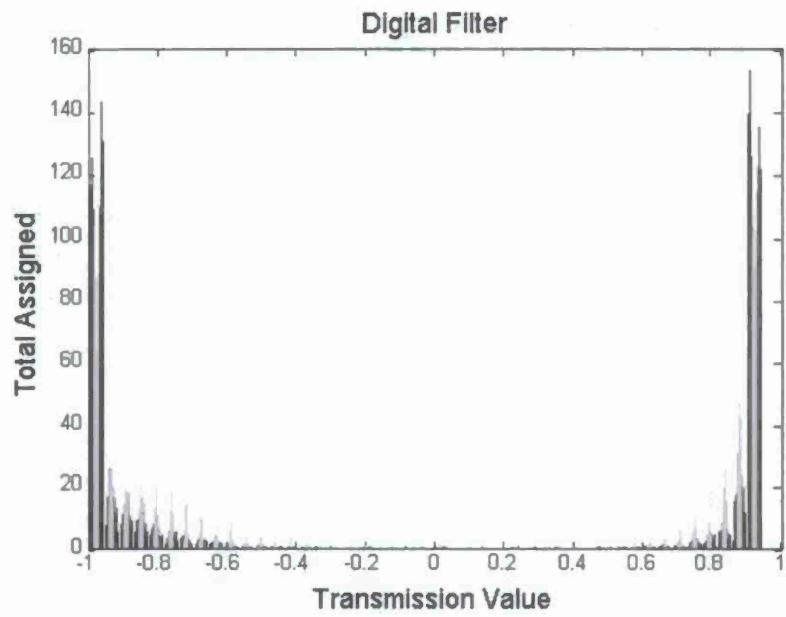
Figure 5-6 Top: Histogram of transmission values of H_{LF}

Bottom: Histogram of 8-bit converted filter H_{LF}

Logarithmic Filter. T = 0.77

1 sigma Linearly Stretched Filter. T = 0.054
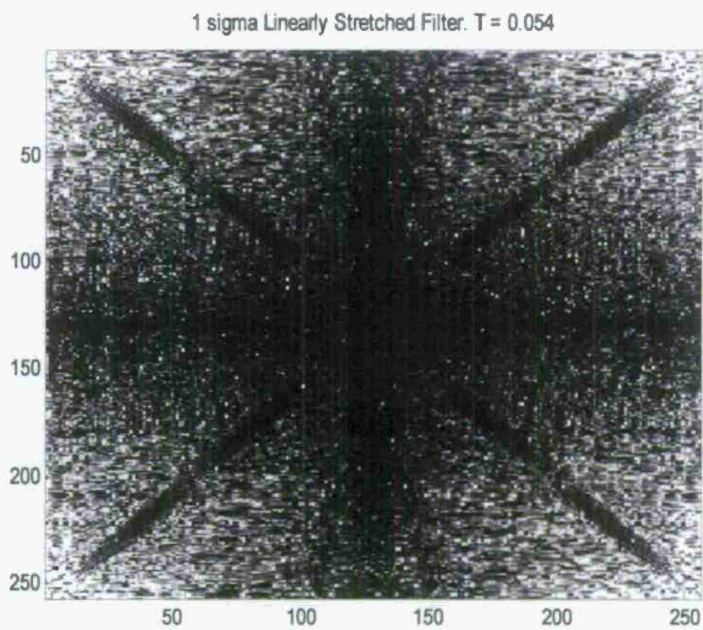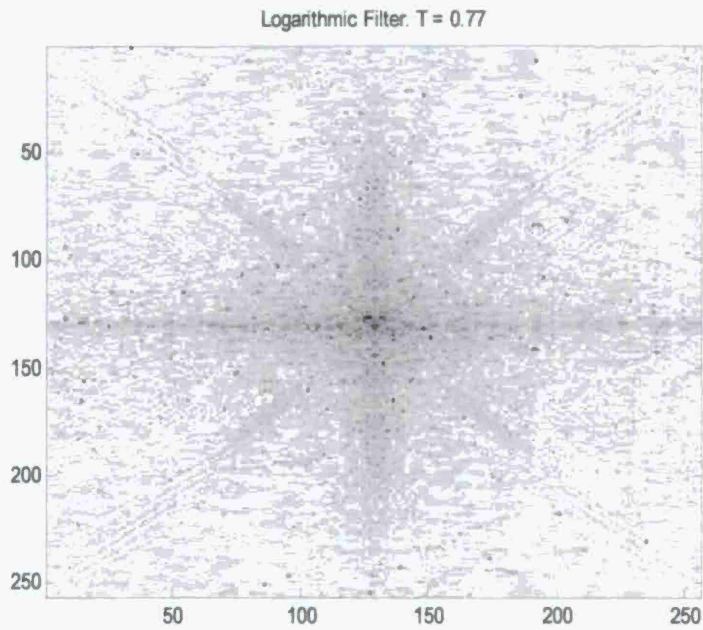
Image 5-2 Grayscale transmission images of filters H_{LF} (top) and H_{LS} (bottom)

63

The calculated transmission values for pose ranges 0,0,0 (pitch,yaw,roll) through 0,9,9 are plotted for the logarithmically compressed filter and linearly stretched filters with $1\sigma, 0.5\sigma$ and 0.1σ stretch values in Figure 5-7. An increase in transmission is shown if the starting point for the linear stretch is closer to the zero throughput value.
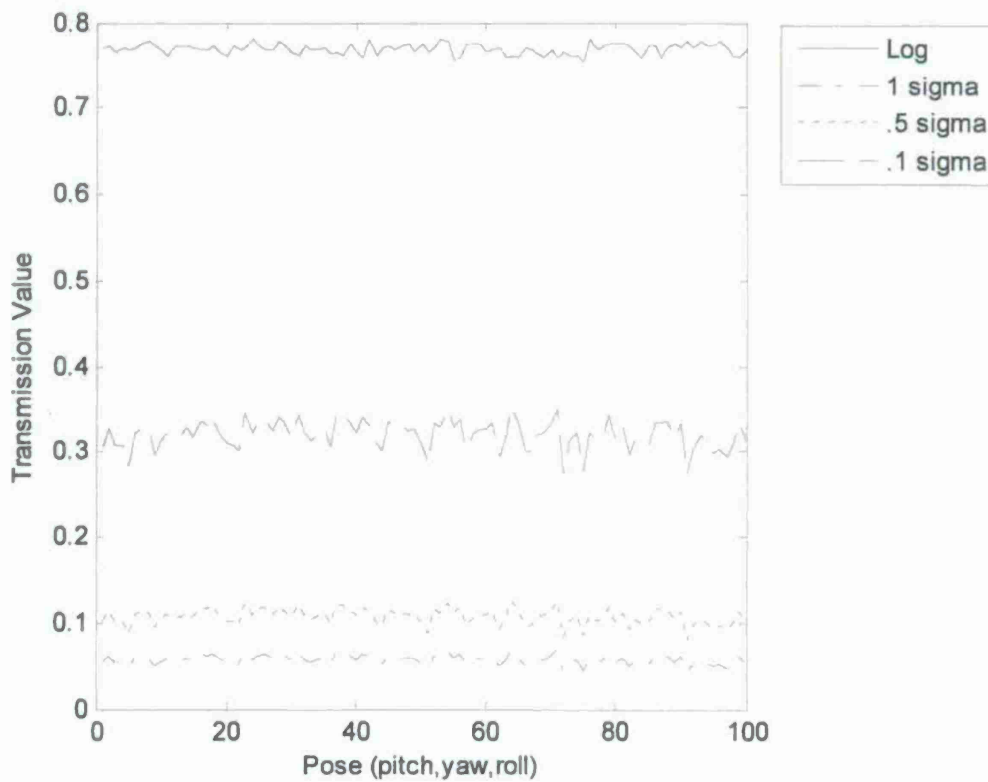
Figure 5-7 Transmission values for poses 0,0,0 to 0,9,9 for logarithmically compressed and linearly stretched filters

5.3. Disqualification of Weighted Composite Filters

5.3.1. Focused MACE Filters

MACE filters were designed digitally using equations (3.21) with
weighting vector u assigned values such that the filter response is maximized for a
single pose parameter. Training set poses were selected to be:

Pitch	0	0	0	0	2	2	2	2
Yaw	0	0	2	2	0	0	2	2
Roll	0	2	0	2	0	2	0	2
Pose #	1	2	3	4	5	6	7	8

Table 5-1 Training set poses used for focused MACE filter

for a total of 8 training images. The effect of weighting the filters digitally is compared
to the optical correlation values. All optical correlation values are normalized to 1. The
effect of the weighting on the digital correlation values and optical correlation values for
weighting vectors $u1$ and $u2$ are shown in Figure 5-8. The weighting vector values were
chosen to only illustrate the digital weighting ability.

Pose #	1	2	3	4	5	6	7	8
$u1$	100	100	100	100	100	100	100	100
$u2$	100	150	225	300	225	150	125	100

Table 5-2 Pose weights assigned for weighted MACE filter.
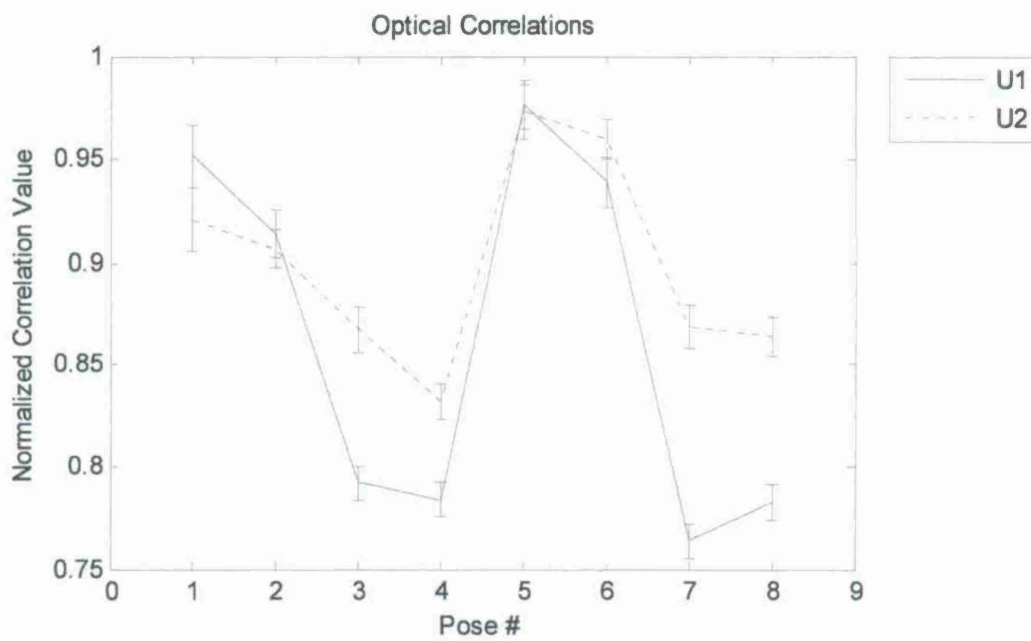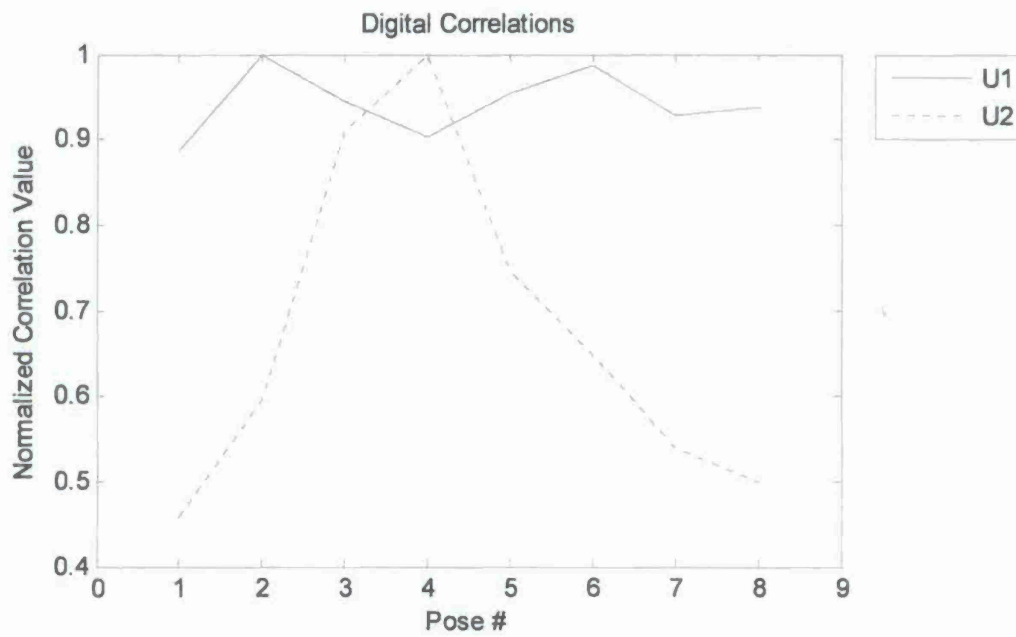
Figure 5-8 Digital and optical correlation peak values using focused MACE filter

5.3.2. MACH Filter

The MACH filter is designed according to equation (3.27) with training set poses from Table 5-1. The digital correlations with images from the training set are compared to the cross correlations values to the BPOF designed for target pose # 4 from the focused MACE filter set. The optical filter created by using logarithmic compression is compared to the cross correlations for the same target BPOF. This comparison is to illustrate the response of a single MACH filter to the cross-correlations of the set of poses versus the cross correlations of a single BPOF from the set. The correlation results are plotted in Figure 5-9. The error bars correspond to $\pm 1\ \sigma$ standard deviation of 30 measurements taken.
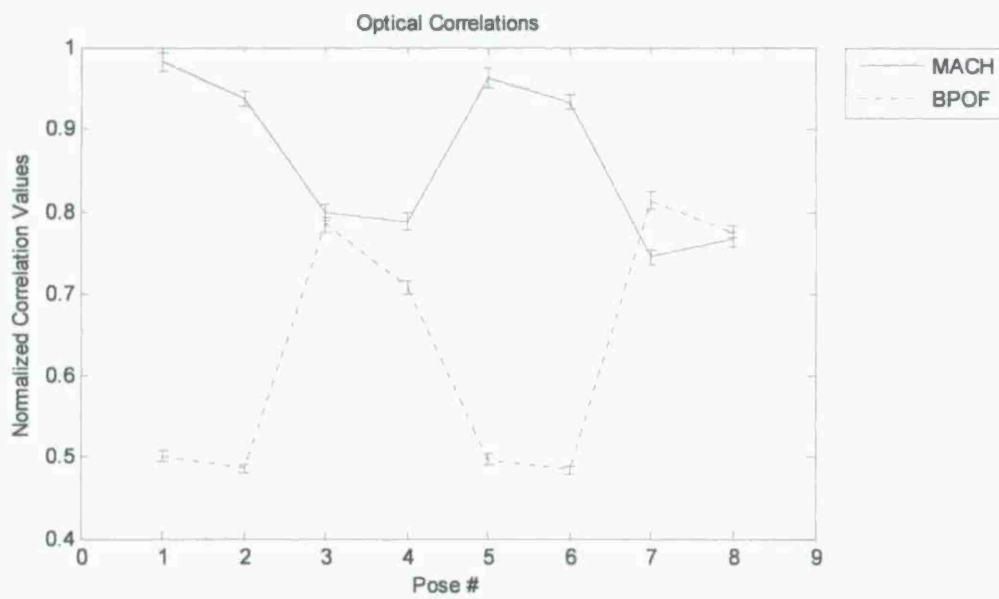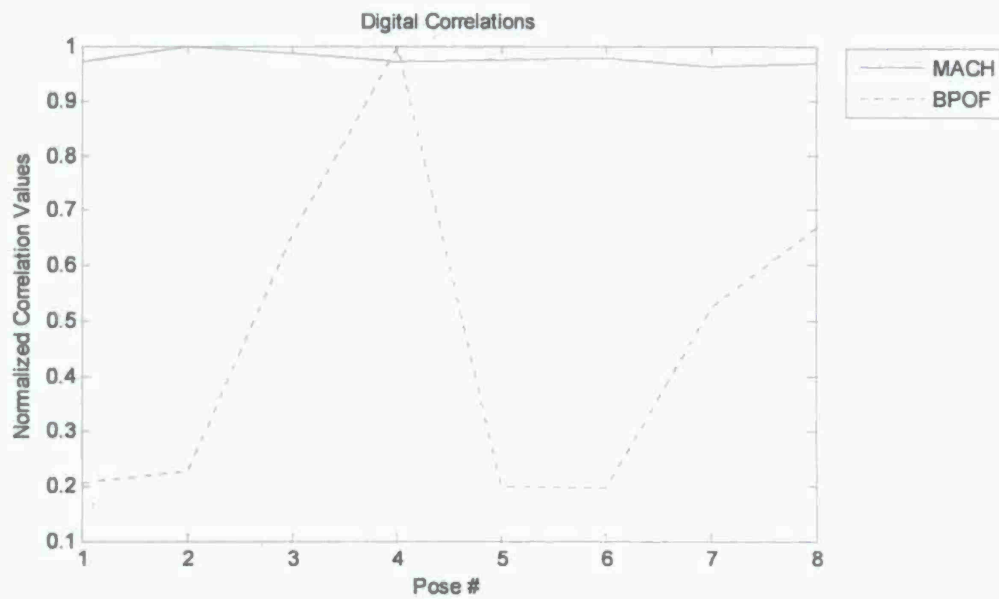
Figure 5-9 Digital and optical MACH filter results

5.4. Validation of Bank of Filters

The BOF approach is tested according to section 4.5. The poses used to test the pose search algorithm are listed below in Table 5-3.

P	0	0	0	1	1	1	2	2	2	3	3	3	4	4	4	5	5	5	6	6	6	7	7	7	8	8	8	9
Y	0	0	1	1	1	2	2	2	3	3	3	4	4	4	5	5	5	6	6	6	7	7	7	8	8	8	9	9
R	0	1	1	1	2	2	2	3	3	3	4	4	4	5	5	5	6	6	6	7	7	7	8	8	8	9	9	9

Ascending

Descending

P	9	8	8	8	7	7	7	6	6	6	5	5	5	4	4	4	3	3	3	2	2	2	1	1	1	0	0	0
Y	9	9	8	8	8	7	7	7	6	6	6	5	5	5	4	4	4	3	3	3	2	2	2	1	1	1	0	0
R	9	9	9	8	8	8	7	7	7	6	6	6	5	5	5	4	4	4	3	3	3	2	2	2	1	1	1	0

Table 5-3 Ascending and descending poses used to test Bank of Filters method

Standard deviations for pose measurements of the craft at 50m using the BOF approach with BPOF and Logarithmically mapped Weiner filters (LMWF) of unprocessed training images are shown in Table 5-4 and Table 5-5 respectively. Data at 100m and at 10m was not attainable due to poor correlation signal and therefore no data is reported at these alignment planes with unprocessed images using BPOF or LMWF's.

69

BPOF	Data Set 1	Data Set 2	Data Set 3
Pitch	.57	.41	.52
Yaw	.30	.27	.23
Roll	.77	.59	.48

Table 5-4 Standard deviations of pose estimates using BPOF

LMWF	Data Set 1	Data Set 2	Data Set 3
Pitch	.82	.91	.85
Yaw	.61	.23	.14
Roll	1.0	1.0	1.5

Table 5-5 Standard deviations of pose estimates using LMWF

The bank of filters approach using digital correlation had zero error across the entire pose set using BPOF. This is due to the autocorrelation value of the target always exceeding the cross-correlation values of the neighboring poses. This was true at all alignment planes. Optically, pose estimates at 100m were inconsistent and at 10m the correlations were of poor quality and difficult to obtain using unprocessed images. To address both issues and to improve the distinction between the auto and

cross correlation at all alignment planes, edge detection and image scaling were implemented.

5.4.1. Edge Detection and Image Scaling

Using edge detection of the images does two things that improve the performance of the optical correlator:

1. Binarized images are easier to reproduce on the input SLM

2. Increases high frequency components for correlation with LMWF

The edges were detected using the Sobel method in the Matlab image processing toolbox. An example of an edge detected image of the craft at each alignment plane with no rotation introduced is shown below in Figure 5-13. Edge detection alone improved the correlations at 100m such that pose estimates could be performed repeatedly and consistently. However, edge detection was not sufficient to produce correlations at the 10m alignment plane. The edges in the image still did not have enough high spatial frequency information to be used with the distortion sensitive Weiner filters. To increase the high spatial frequency information, the image at 10m was scaled from 256x256 to 32x32 and reinserted in a blank 256x256 matrix. The correlations showed a marked improvement over the un-scaled images and the pose estimates obtained were repeatable with high SNR correlations. Scaling the image at 50m from 256x256 to 64x64 and reinserting into a blank 256x256 matrix also improved the correlation SNR and pose estimates. With edge detection at 100m, and scaling the edge detected images at 50m and 10m alignment planes, pose estimates were obtained for each

71

	Alignment Distance		
	10m	**50m**	**100m**
Pitch	0	0	0
Yaw	0.15	0.15	0.15
Roll	0	0	0

Table 5-6 Standard deviation of error in pose estimates using edge
detection and image scaling (at 50m and 10m)

alignment plane taking 30 measurements at each plane. The standard deviation

for the accuracy of each rotation at each alignment plane is shown above in Table

5-6. The standard deviation for the entire pose estimation sequence and the pose

estimates obtained are shown in Table A-2 through A-4 for each alignment plane.

The effect of edge detection and image scaling on the pose estimation

routine can best be seen by looking at the statistical performance of the engine of

the search algorithm which loads the filters for the pose set (selected pose and its

neighboring poses) given to it and correlates them with the input scene. Doing

this for each pose in the selected pose set, a comparison of the LMWF is

compared to the BPOF for the same edge detected/scaled image. The correlation

peak values obtained for each pose and its neighboring poses is presented in the

Appendix in Figure A - 1 through Figure A - 27 for 100m, 50m and 10m

alignment planes. For the 50m alignment plane, the improvement using edge

detection and image scaling can be seen by comparing the results from using

unprocessed images and the edge detected images. The 50m alignment plane was

the only plane initially that could give semi-repeatable measurements to take a

statistical set. It is therefore the only plane where data is reported for unprocessed

72

images and serves as the representation of the improvement from using edge detection and image processing. The complete set of plots can be found in the Appendix. Figure 5-10 below shows the effect of edge detection and scaling for poses (1,1,2), (1,2,2), (2,2,2) and (2,2,3). It can be seen that the first pose correlation peak value (the autocorrelation/target pose) exceeds the values for all the neighboring poses when using edge detection and scaling. The unprocessed images have multiple neighboring pose cross-correlations whose values exceed the target. This condition leads to pose estimation errors in the algorithm.
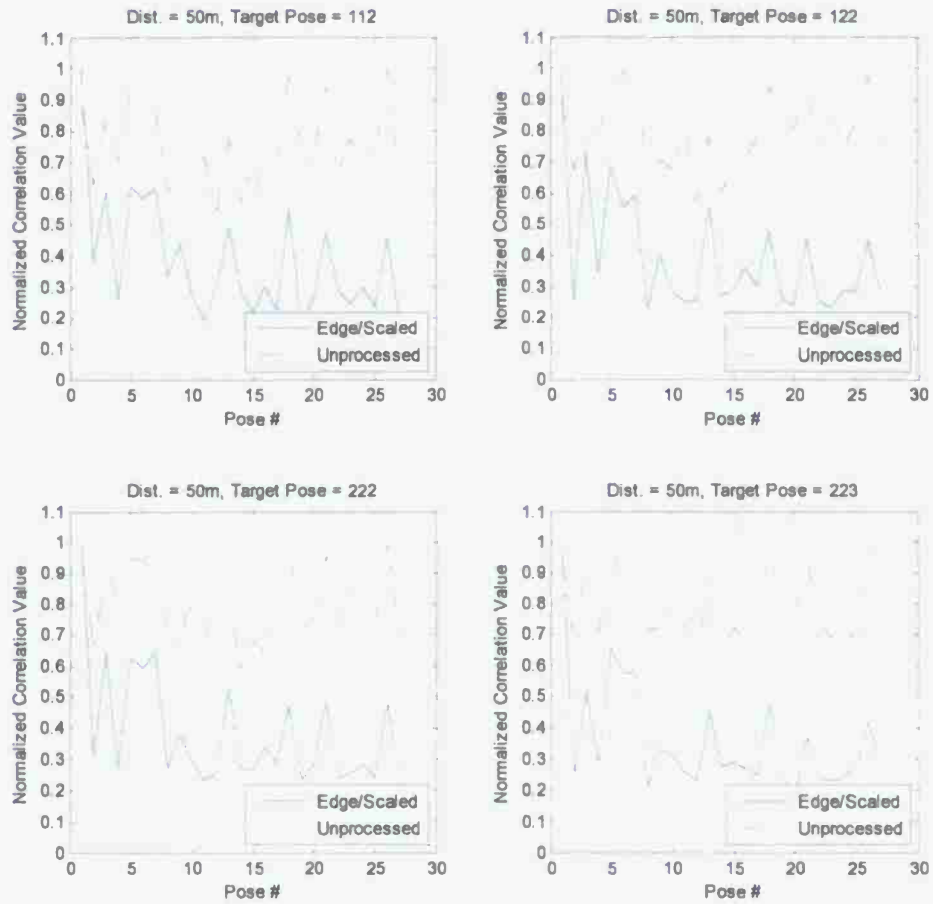
Figure 5-10 Normalized correlation values for edge detected and scaled images versus unprocessed images with craft at 50m alignment plane.

The number of poses whose cross-correlations exceed the autocorrelation in the pose set at the 50m alignment plane is plotted below in Figure 5-11. The value at each target # is the number of cross correlations in that target's neighboring pose set (26 neighboring poses) that exceeds the value of the target correlation. The target # corresponds to the target specified in Table 5-3 Ascending and descending poses used to test Bank of Filters methodTable 5-3 in the ascending section. A significant difference in the opportunity for error can be seen when going from unprocessed to edge detected and scaled images. This data is plotted in Figure 5-12 for each alignment plane using edge detected scaled images (image scaling at 50m and 10m only).
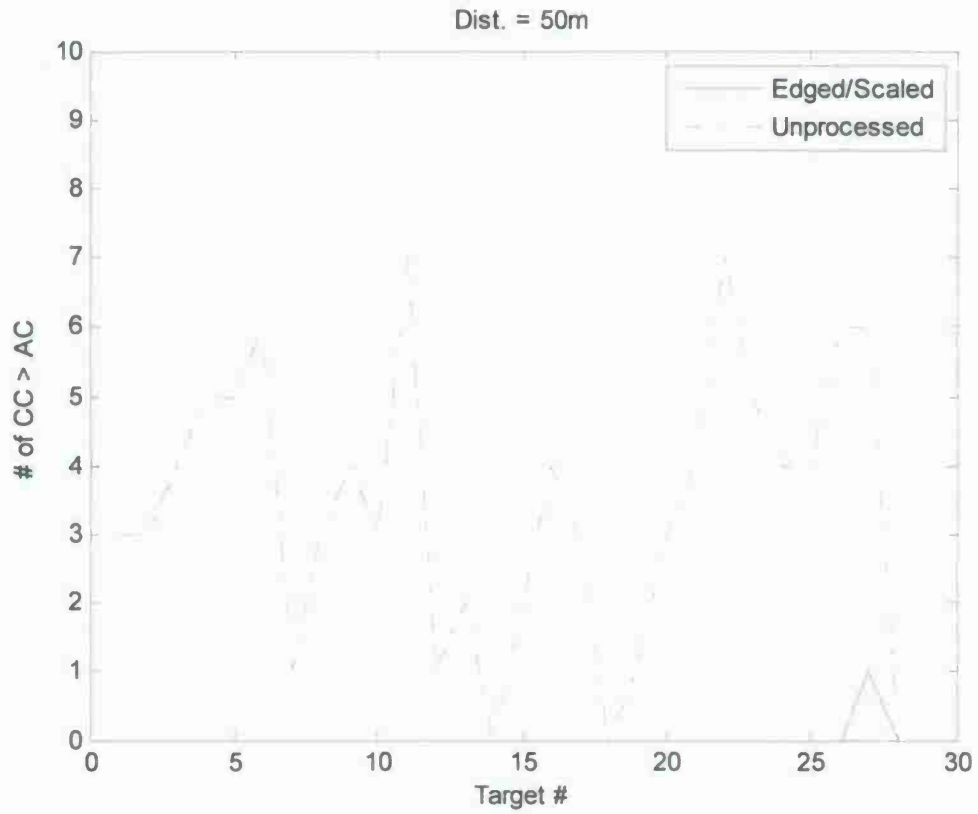
Figure 5-11 Comparison of the number of cross-correlation values that exceed the target autocorrelation values for each target in the target set with the target craft at 50m using edge detection and image scaling vs unprocessed images.
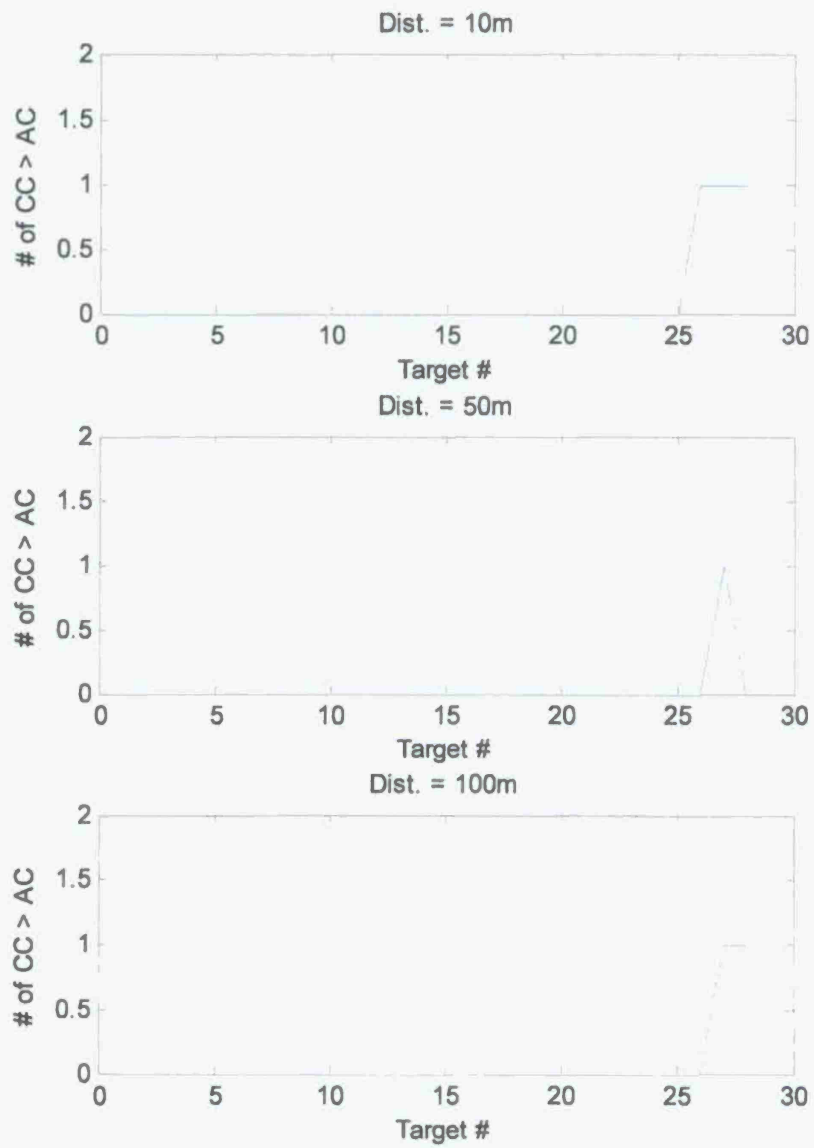
Figure 5-12 Number of cross-correlation values that exceed the target autocorrelation values for each target in the target set with the target craft at 50m.

Unprocessed - 100m

Edge Detected - 100m

Unprocessed - 50m

Edge Detected - 50m

Unprocessed - 10m
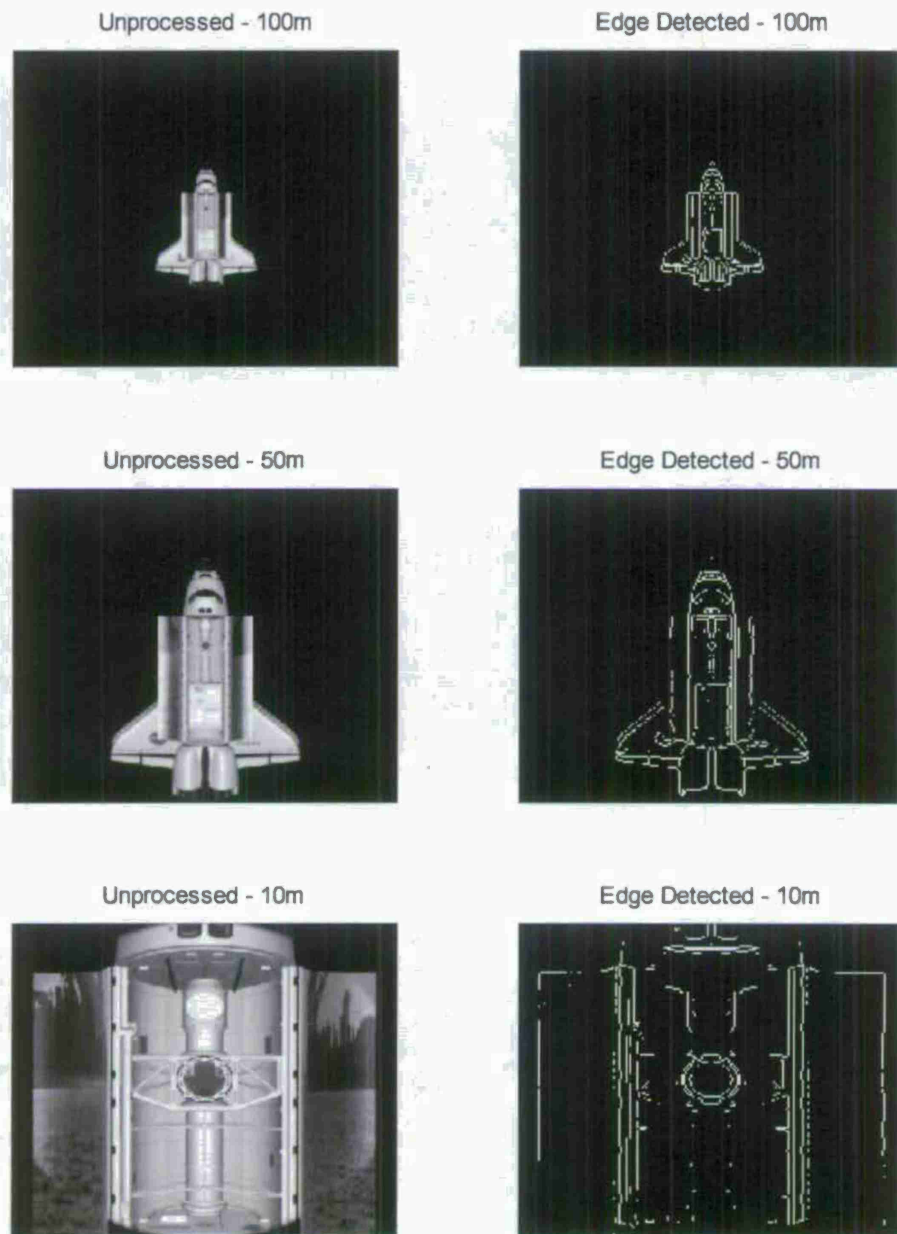
Edge Detected - 10m

Figure 5-13 Unprocessed and edge detected images at 100m (top), 50 m (middle) and 10m (bottom) alignment planes.

Unprocessed - 10m

Unprocessed Correlation

Edge Detected - 10m

Edge Detected Correlation

Edge Detected/Scaled - 10m

Edge Detected/Scaled Correlation
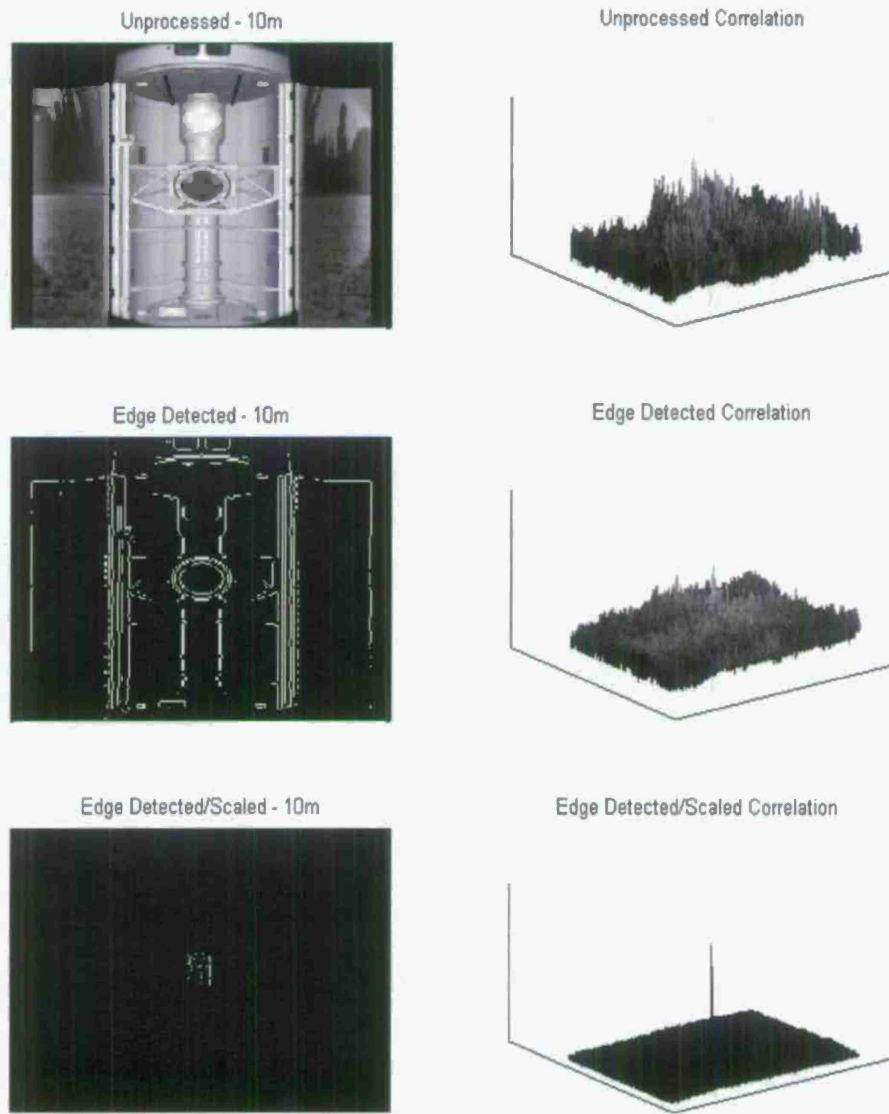
Figure 5-14 10m correlations using unprocessed (top), edge detected (middle) and edge detected images with scaling (bottom).

Unprocessed - 50m

Unprocessed Correlation

SNR = 70
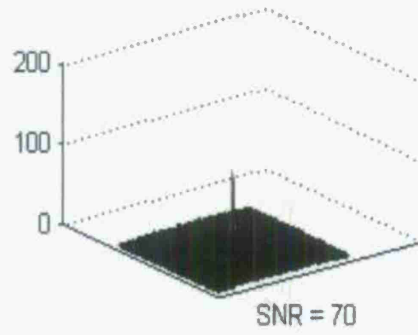
Edge Detected - 50m

Edge Detected Correlation

SNR = 65
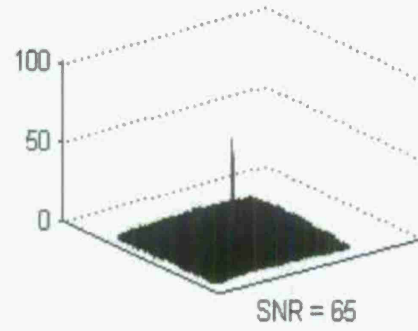
Edge Detected/Scaled - 50m

Edge Detected/Scaled Correlation

SNR = 79
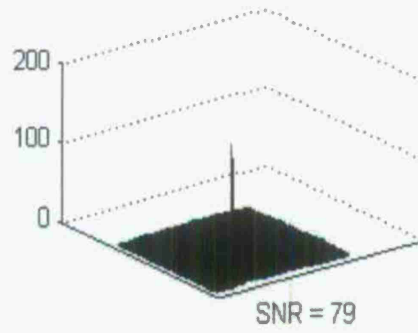
Figure 5-15 50m correlations using unprocessed (top), edge detected (middle) and edge detected images with scaling (bottom).

5.4.2. Additive White Gaussian Noise Effects

To determine how sensitive the pose estimation is to noise, Additive white Gaussian noise was added to the images using the additive white Gaussian noise (AWGN) command in the Matlab communications toolbox. The signal power of each image is measured and AWGN is added such that the SNR is as specified. No impact was noticed in the standard deviations of the pose estimation accuracy until the SNR was 20dB and below. The AWGN was added to the unprocessed images and the edge detection and image scaling was applied to the noisy image. The noisy edge detected image was then written to the input SLM and the filter created from the noiseless image was written to the Filter. This is repeated for each image associated with each pose in the pose set. The visual effect of the AWGN to the images and on the edge detected images is shown below in Figure 5-18 to Figure 5-16 for each alignment plane. The scaled edge detected images corrupted with noise for the 50m and 10m alignment plane is shown in Figure 5-19 and Figure 5-20. The standard deviation of the error in the pose estimates obtained using noise corrupted images is shown in Table 5-7. As the noise is increased, the standard deviations of the error in the pose estimate is seen to increase at varying degrees depending on the alignment plane with the 50m plane showing the most robustness. This is due to the image containing more information than the clipped 10m image and the scaling at 50m results in an image that is further reduced in size than the un-scaled 100m image, an interesting and unexpected result. The further craft appears to be, the more accurate the pose

81

estimation suggesting scaling at all alignment planes improves the correlations

and algorithm performance.

	Dist = 10m		
	20dB	15dB	10dB
Pitch	0	0	1.37
Yaw	0.19	0.26	0.35
Roll	0	0	1.06

	Dist = 50m		
	20dB	15dB	10dB
Pitch	0	0	0
Yaw	0.15	0.13	0.13
Roll	0	0.13	.19

	Dist = 100m		
	20dB	15dB	10dB
Pitch	0.32	2.19	2.72
Yaw	0.33	0.88	1.15
Roll	0.13	1.75	1.59

Table 5-7 Standard deviation of pose estimate error using noise corrupted images

	Dist = 50m SNR = 5dB	
	BPOF	LMWF
Pitch	2.23	0.13
Yaw	2.3	0.19
Roll	2.36	0.45

Table 5-8 Standard deviation of pose estimate error using BPOF's vs LMWF's

The advantage of using the LMWF's instead of BPOF's is the ability to

suppress noise. This will be useful in applications when clutter is being

considered. When performing pose estimates with 5dB SNR at the 50m

alignment plane, the difference between the BPOF and the LMWF can be seen in

Table 5-8. The error using BPOF's is seen to be much greater than the LMWF's.

10m, No noise

SNR = 20dB   SNR = 15dB   SNR = 10dB

Edge Detected Images

SNR = 20dB   SNR = 15dB   SNR = 10dB

Figure 5-16 Unprocessed and edge detected images after AWGN has been added to the input
scene at the 10m alignment plane

50m, No noise

SNR = 20dB   SNR = 15dB   SNR = 10dB

Edge Detected Images

SNR = 20dB   SNR = 15dB   SNR = 10dB
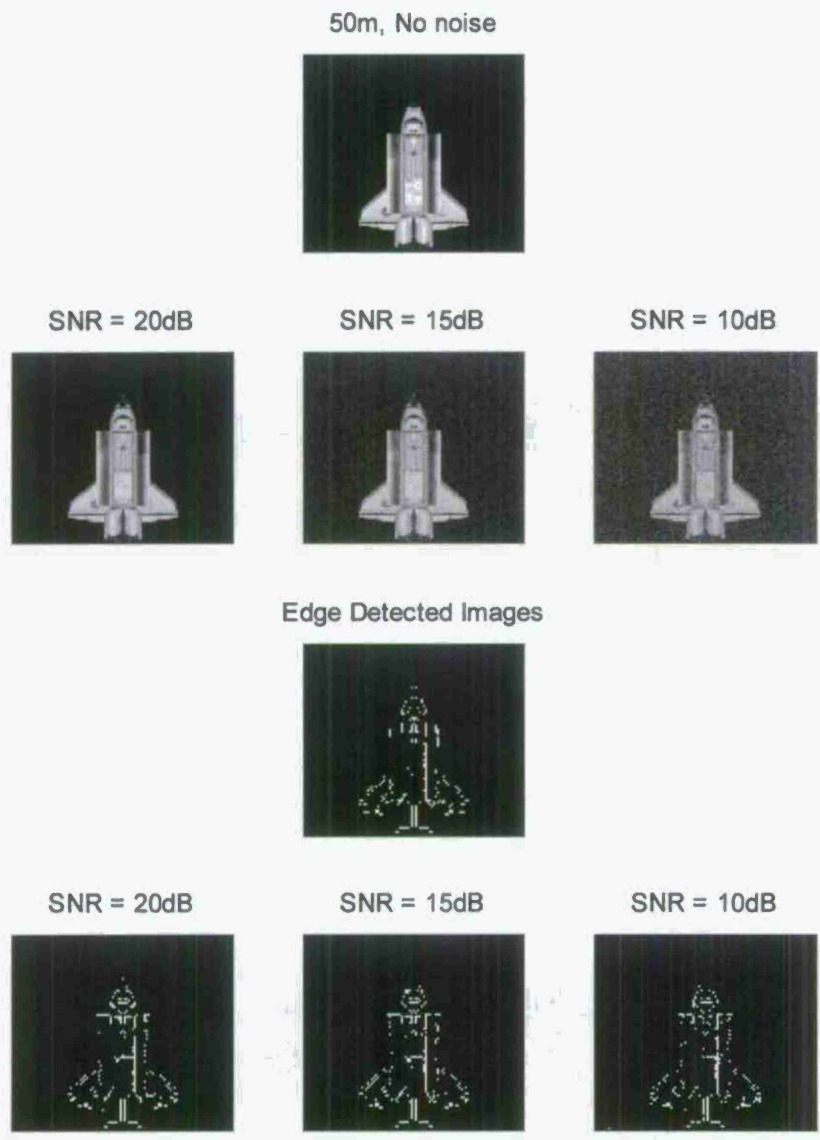
Figure 5-17 Unprocessed and edge detected images after AWGN has been added to the input scene at the 50m alignment plane

100m, No noise

SNR = 20dB   SNR = 15dB   SNR = 10dB

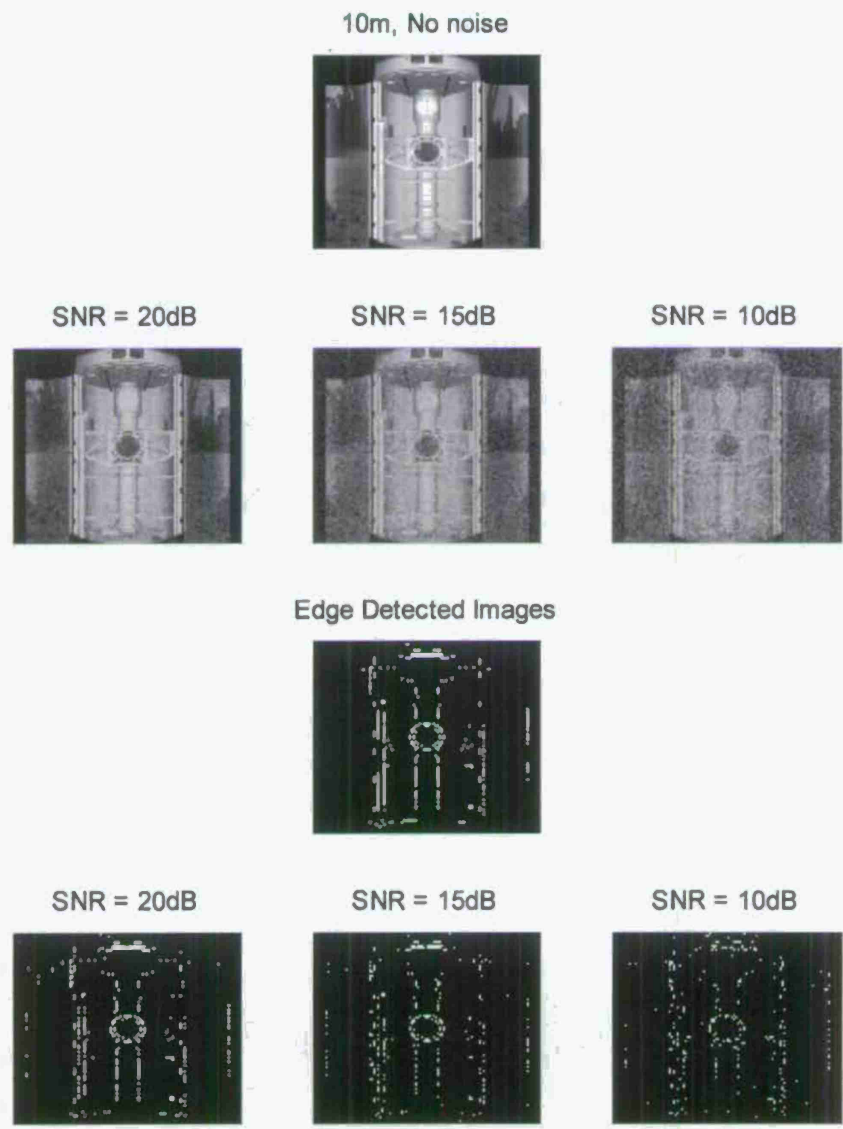Edge Detected Images

SNR = 20dB   SNR = 15dB   SNR = 10dB
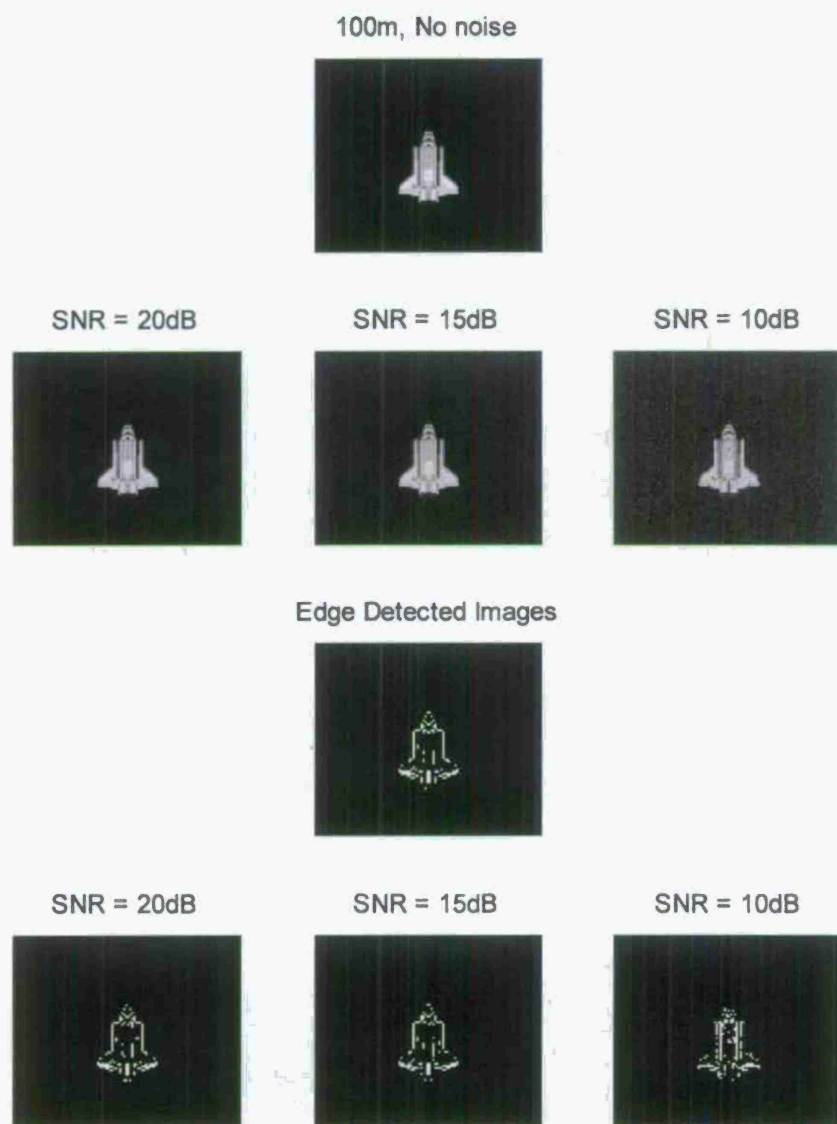
Figure 5-18 Unprocessed and edge detected images after AWGN has been added to the input scene at the 100m alignment plane
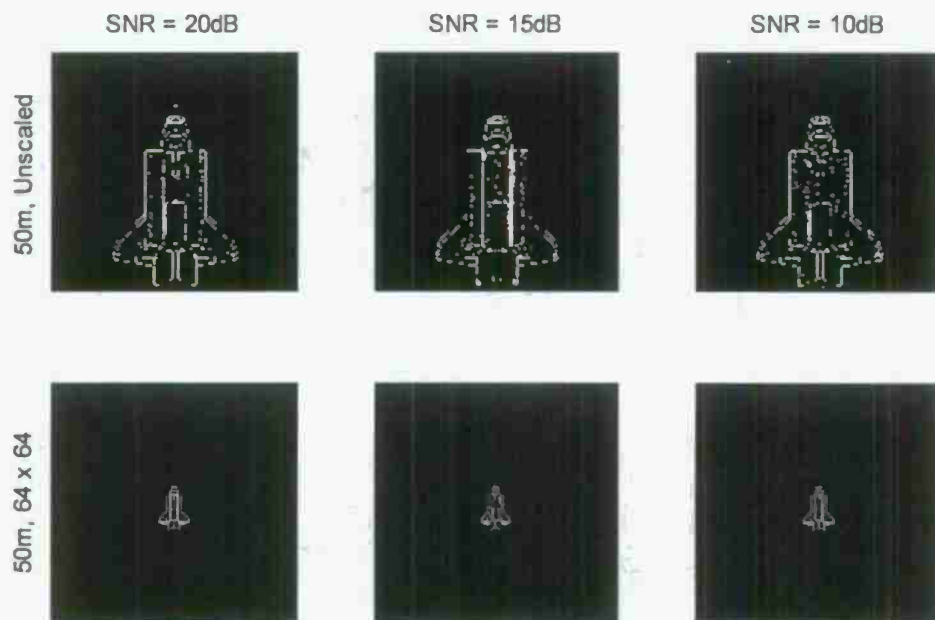
Figure 5-19 Scaled edge detected images corrupted with AWGN at the 50m alignment plane
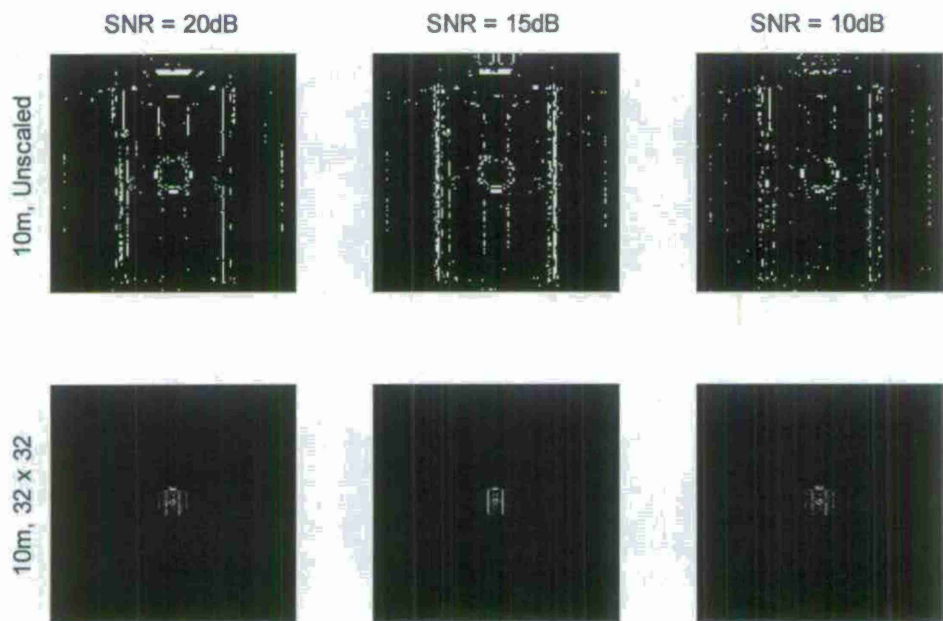
Figure 5-20 Scaled edge detected images corrupted with AWGN at the 50m alignment plane.

5.5. Optimum Rotation Angle Selection

Up to now, all filters have had a constant phase rotation of $\pi/2$ introduced before binarization or projection to the real axis. This is equivalent to binarizing or projecting the imaginary axis, the axis of symmetry. This is a common approach in research; however, the filter can be arbitrarily rotated in the complex plane as suggested with the TLA mentioned in section 3.3. To create a projected filter with minimum energy difference with the original filter, the energy equation

$$E = \left| h_p - h e^{i\varphi} \right|^2 \tag{5.2}$$

must be minimized for projected filter h_p by rotating filter h by a phase amount φ. Another method of determining the optimum rotation angle is mentioned by Chao using the equation (45)

$$\varphi = \frac{\pi}{4} - \frac{1}{2} \tan^{-1} \left(\frac{-\sum 2 h_r h_i}{\sum h_r^2 - h_i^2} \right) \tag{5.3}$$

where h_r and h_i are the real and imaginary parts of filter h. Autocorrelations of the craft rotated in yaw 360 degrees is shown below in Figure 5-21. The autocorrelations are taken using the optimum rotation angles calculated using equations (5.2) and (5.3). They are plotted versus the autocorrelations using a fixed rotation of $\pi/2$ and the normalized digital autocorrelation values. The optimum rotation angle has little to no effect on the general shape of the yaw rotation correlation peak values. All three optical methods are have a similar profile in comparison to the digitally obtain correlation response. In Figure 5-12, the error introduced begins when the yaw rotation approaches 8-9 degrees. The data was taken on the portion of the plot below ranging from 180 – 190 degrees where it is a relatively flat region. In locations where the rotation is at 25 to 30 degrees,

88

the correlation peak disappears. This is not found to happen in the digital model and the optimum rotation angle does not compensate for it. Further investigation will need to be performed to determine the root cause of the degrading correlation with yaw rotation.
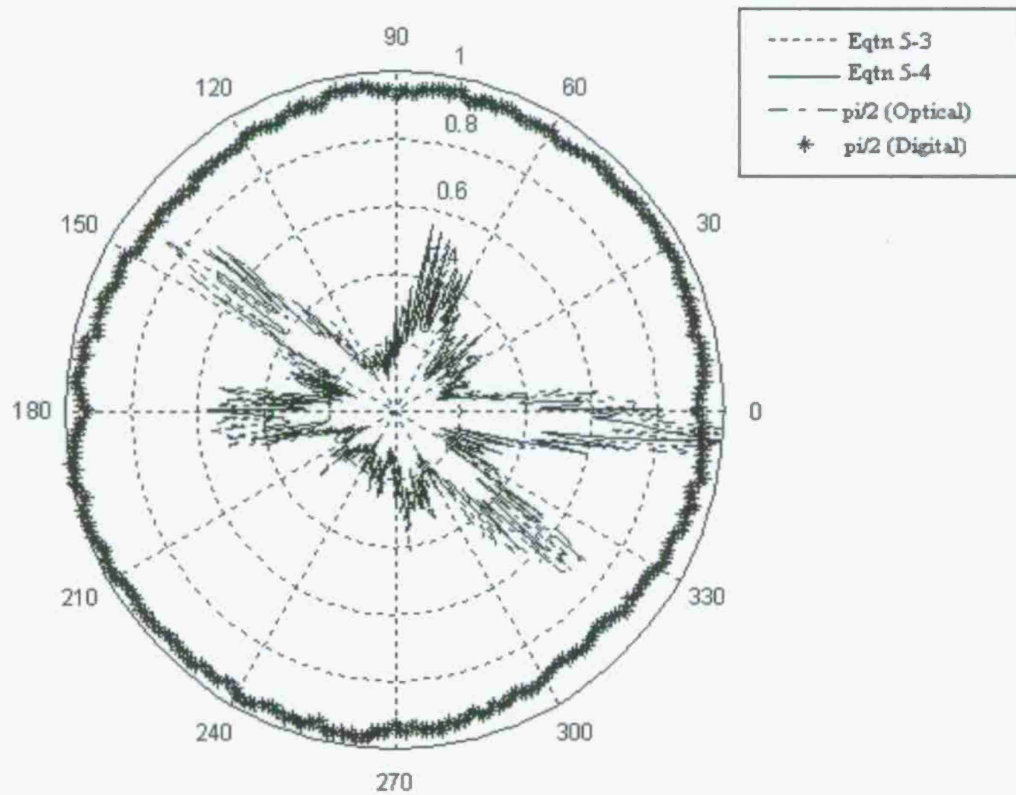
Figure 5-21 Normalized auto-correlation values of craft rotated in yaw 360°

5.6. Summary

The SLM characterization showed an active applied voltage region between the
8bit values of approximately 100 to 190 in the input SLM with a steady gradual
increase in transmittance value from 190 to 255. The filter SLM has an active region
between the 8bit values of approximately 70 to 210. In the input SLM, this reduction
was overcome using binary edge detected images and at the filter SLM, mapping the
logarithm of the dynamic range of the correlation filter showed improved results over
the BPOF. Logarithmic mapped filters also showed greater optical efficiency than
the linearly stretched filters (Figure 5-7) with more pixels being modulated,
particularly in the mid to high frequency range as seen in Figure 5-6.

The composite filter designs were not useful when considering pose estimation
using weighted filter responses across a training set of poses. The response of the
autocorrelation of one pose to the next is seen to exhibit greater variance than the
digital response. Controlled weighting is therefore not possible when gain cannot be
added optically to compensate for the autocorrelations with decreased values such
that a controlled response can be obtained. In Figure 5-8 and Figure 5-9, the
difference in digitally and optically weighted composite filters can be seen. In the
case of Figure 5-8 where the filter is designed to be "focused" at a single pose, this is
easily accomplished with the digital filter. The optical filter results clearly disqualify
this approach for an optical correlator based pose estimation routine. The optical
MACH and OTMACH filters were however implementable using logarithmic
mapping for distortion invariance across a training set of poses in a target tracking

90

scenario. Composite filter designs have already been demonstrated in this capacity using an amplitude modulated optical correlator by Chao (42).

The BOF approach using logarithmically mapped Weiner filters relied on the sensitivity of each filter to distortions, creating a stronger response for the autocorrelation (target pose) and a weaker response to the cross correlations (neighboring poses). The edge detected images using the Sobel method improved the SNR and the pose estimation of the craft at 100m using the BOF approach. At 50m and 10m, edge detection and image scaling combined gave the best results. Removing the low frequencies and creating a binary input image compensated for the reduced resolution in the input SLM due to the delayed response of the liquid crystals to the magnitude of the applied field. The image scaling increased the high spatial frequency content which the Weiner filters were designed to detect. The alignment plane at 10m showed the most improvement when implementing the image scaling. The pose estimates at 50m also showed an improvement with image scaling suggesting that image scaling can be performed at all intermediate alignment planes as the craft approaches for docking. Performing edge detection and image scaling also contributed to a noise tolerant approach. As seen in Table 5-7, the additive Gaussian noise did not affect the pose estimates until the SNR dropped between 20 to 10dB. At the 50m plane, a SNR of 5dB still has acceptable pose estimates as shown in Table 5-8 in comparison to using the BPOF.

The error in the pose estimation routine was seen to be introduced consistently as the yaw rotation approached 8-9 degrees. In Figure 5-21, the correlation dependence on the yaw rotation is seen to change drastically with rotation angle. This yaw

91

dependence did not show up in the digital correlation model using the BOF approach.

It is therefore not a fundamental correlation issue, and is suspiciously a modulator

issue. Further investigation into the source of the yaw dependence on the correlation

needs to be performed.

Chapter 6

Conclusions

6.1. Conclusion

Pose estimation using a bank of filters and a pose search algorithm approach worked in both the digital and optical domain with sub degree standard deviations in accuracy. The digital routine did not require as much image processing as the optical method due to the optical inability of the input SLM to achieve the resolution as the original digital image. The digital routine is also capable of implementing complex composite filter designs which performed poorly when optically implemented when designed for the optical weighting of poses for pose estimation. This was not an unexpected result and was anticipated due to the limited dynamic range of the filter SLM and its amplitude only (real valued) modulation. It was however worth pointing out to distinguish the composite filter implementation in tracking using an optical correlator and to explicitly show why this approach cannot be extended to pose estimation using digitally weighted filter models.

Using 3D software to render the training images eliminated otherwise necessary hardware acquisition and setup of models and rotation platforms. The lighting and camera options with readily available models of both space and military craft make 3D modeled training images a modern solution to the generation of training image sets for pose estimation and target tracking algorithm development. The 3D approach also has

the utility of CAD import. For edge detected images, the CAD model without surface texturing or other 3D enhancements used to add realism (which is typical in gaming applications) can be used as is to generate the training set. The BOF approach using a pose search algorithm and 3D software is a fully automatable process which would not require the use of cooperative targets on the craft. The simulation and debugging of algorithms can also be done using only a computer and correlator instead of hardware setup. Using Matlab as an interface to the correlator for the pose estimation routine and for the development of filter conversion algorithms and image processing of the 3D software generated training images allowed for the programming and generation of the filter bank and image loading sequence for bank of filters with search algorithm proof of concept. It allowed for programmable changes to filter designs or image processing to be implemented within a single software platform. This general approach to pose estimation is therefore more streamlined and less costly in time and hardware from development to simulation than other existing approaches.

The primary difficulty in this research was creating and mapping distortion sensitive filters. Many unsuccessful attempts in the mapping resulted in inconsistent correlation results from one pose to the next. The autocorrelations must exceed the cross correlations of the neighboring poses in order for the BOF approach to be successful with a minimum amount of error being introduced from one detection cycle to the next. With too many poses with cross correlations exceeding the target pose, the search algorithm is rendered ineffective. Using BPOF's during the initial qualification testing of the search algorithm resulted in encouraging but not repeatable results. Implementing logarithmic amplitude modulation showed a significant improvement in the SNR in both unprocessed

94

and edge detected image correlations. However, the BPOF, when using edge detected images, did exhibit repeatable behavior, but had more noise in the correlation than the LMWF's. The LMWF's are therefore more suitable for pursuing correlation detection in a cluttered environment.

The SNR of the correlations, although tending to follow the peak values, was not more effective than using the peak values of the correlations to distinguish the target from the neighboring poses. The logarithmic mapping outlined in section 5.2.2 along with the edge detection and image scaling yielded the best results. This was due to a combination of three primary contributing factors:

1. The modulation of more pixels in the filter design by mapping more values of the logarithmically compressed filter to the active region of the SLM.

2. Using edge detected images removed the low spatial frequency content of each training image helping to distinguish one image from the other

3. Scaling the images increased the high spatial frequencies at the close ranges where the correlation signal was the weakest and at times, non existent.

The ability to get repeatable near zero error measurements across the training set after implementing the three step approach briefly summarized above resulted in an optical method that is on par with a digital method in accuracy. The speed of the optical correlators SLM's have been the most favorable feature of the correlator which gives it an edge over digital routines. The drawback of not being able to implement the digital composite filters on an optical correlator is one of the primary reasons digital pose

95

estimation has been the most likely solution. It enables pose estimation using a minimum number of correlation filters. However, if the number of filter images can be reduced to cover only anticipated realistic docking ranges of rotation, the size of the optical correlators filter bank can be kept to a minimum. Composite filters also use an interpolative result which is not as accurate as a 1:1 comparison of image to matched filter with 1 degree resolution. It has been shown in this research that the BOF approach can yield accurate pose estimates, even with the craft buried in a large amount of additive noise (with an SNR of 10dB), with 1 degree resolution using 27 correlations per detection cycle. A digital pose estimation approach using weighted composite filters that can achieve the same level of accuracy in resolution in 3 degrees of rotational freedom could not be found by the author. This approach may therefore be favorable for applications where accuracy to within 1 degree resolution in pose measurement is critical and a higher detection frequency is desired. To keep the filter bank size to a minimum, only cooperative targets with limited expected rotational range for docking or rendezvous is recommended.

6.2. Recommendations for Future Research

In this research, pose estimates using a bank of filters was demonstrated using a pose search algorithm with logarithmically mapped distortion sensitive filters using Sobel edge detection and image scaling. This approach was shown to be effective at each alignment plane in the space shuttle to ISS docking scenario of 100m, 50m and 10m with the craft buried in significant additive noise. The next logical step in research would be to perform pose estimates of the craft at any distance while it is in transit from one

96

alignment plane to the next. This would allow for continuous monitoring of the crafts orientation. In a rendezvous scenario when the crafts may be approaching one another, keeping track of their respective orientations while in transit is useful to prevent collision hazards from unexpected changes in trajectory. However, with the current approach, this would require many filter banks with overlapping effective scale (which corresponds to distance) ranges to achieve a continuum in detection without loss of signal. There will also be an additional number of necessary correlations; the pose detection cycle and the scale detection cycle to determine how the craft is oriented and if it has moved within the range of the neighboring filter banks respectively. With the improved results that image scaling provided, instead of having multiple scaled filter banks, a single bank can be used by scaling the input image to the most effective scale size used by the correlator which provides the most sensitive and highest SNR correlations. One method of implementation would be to have a rangefinder provide continuous distance measurements to the pose algorithm such that the correct scale factor can be applied to the input image before edge detection is applied and the data then sent to the input SLM. All correlations will then be made using a single filter bank instead of multiple banks to cover the entire range.

Another method would utilize the correlator to track distance and pose by taking two additional correlations. The first cycle being the pose detection cycle and the second cycle (using two additional correlations) would be:

1. Correlation of input image with detected pose filter using additional scaling.

2. Correlation of input image with detected pose filter using less scaling

97

With an optimum correlator operating speed of 1000Hz, 29 correlations to track pose and determine scaling from change in distance is easily achieved in controlled docking and rendezvous scenarios with cooperative vehicles. The pose selection and the scaling for the next input image will be determined using the peak associated with both pose and best scale measurements.

The loss of resolution from one scaled distance to the next will result in identical poses being slightly different from one another due to the range of the craft before scaling. The effect of this difference on the pose detection cycle will have to be determined and must be less than the effect of the neighboring poses for the performance of the algorithm to be consistent and accurate across the translation range. This small difference in resolution losses is expected to have a negligible impact.

Another solution may be to create the filter bank from an image which is a composite of edge detected scaled images of identical poses. The filter will therefore give a correlation peak for the same pose over a range of distance without having to scale the input image while also discriminating against neighboring poses. This would require generating many training images that cover the anticipated translation range at a scale interval that does not exceed the scale response of the filter. For close distances when portions of the craft begin to be clipped by the field of view of the camera, feature extraction of the craft determined by the features seen at the closest desired position can be used (such as the docking port) as correlation targets. This therefore would require two filter banks to be created; one for the far field and one for the near field. All of these proposed methods however can be implemented digitally with a BOF for low detection

98

frequency requirements. The range of poses can still be limited to realistic approach poses of the craft which will limit the size of the necessary filter bank.

Further investigation needs to be performed to determine the root cause of the unexpected strong correlation dependence on yaw rotation. This dependence is assumed to be the cause of the error being introduced near the edge of the yaw range in the pose ranges used. The data is seen to be consistent in zero error until the yaw range approaches 8-9 degrees. This is not a fundamental correlation issue and is more than likely modulator specific.

Appendix

Figure A - 1 Auto and cross correlation peak values for craft at 10m. Target pose is labeled on graph. Neighboring poses are in Table A - 1
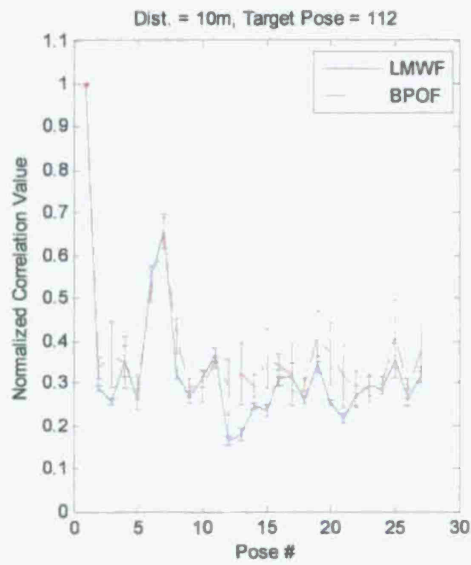
Figure A - 2 Auto and cross correlation peak values for craft at 10m. Target pose is labeled on graph. Neighboring poses are in Table A - 1
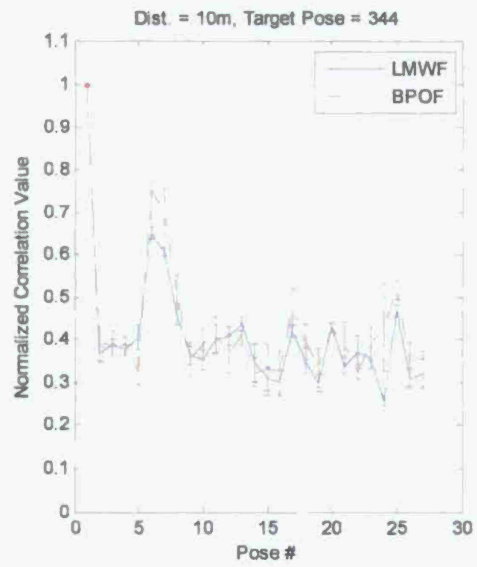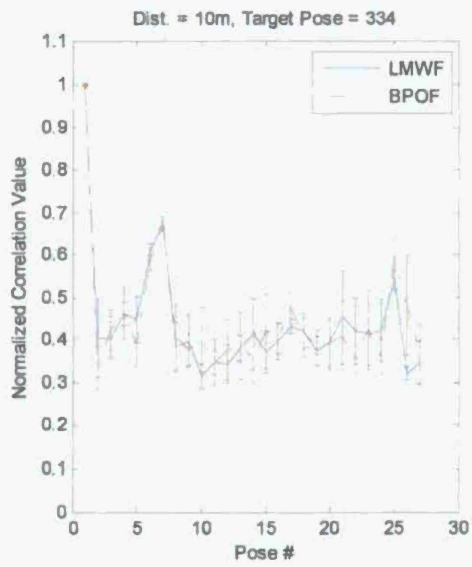
Figure A - 3 Auto and cross correlation peak values for craft at 10m. Target pose is labeled on graph. Neighboring poses are in Table A - 1

Figure A - 4 Auto and cross correlation peak values for craft at 10m. Target pose is labeled on graph. Neighboring poses are in Table A - 1

Figure A - 5 Auto and cross correlation peak values for craft at 10m. Target pose is labeled on graph. Neighboring poses are in Table A - 1

Figure A - 6 Auto and cross correlation peak values for craft at 10m. Target pose is labeled on graph. Neighboring poses are in Table A - 1
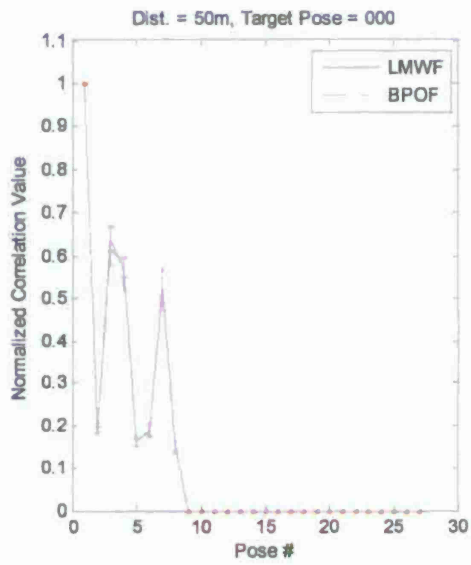
Figure A - 7 Auto and cross correlation peak values for craft at 50m. Target pose is labeled on graph. Neighboring poses are in Table A - 1
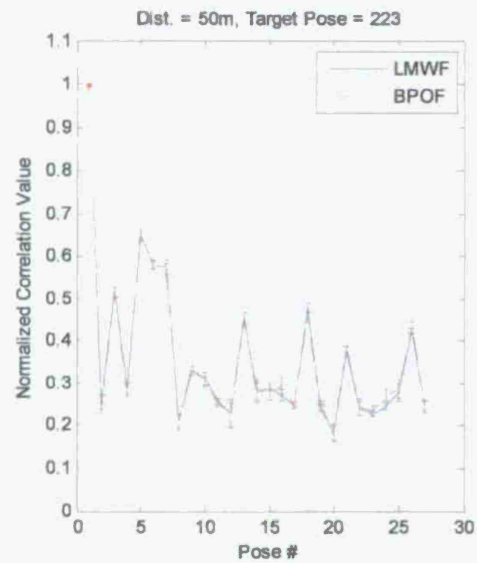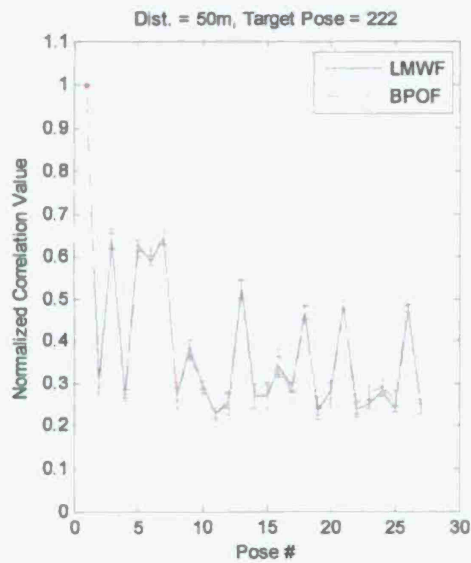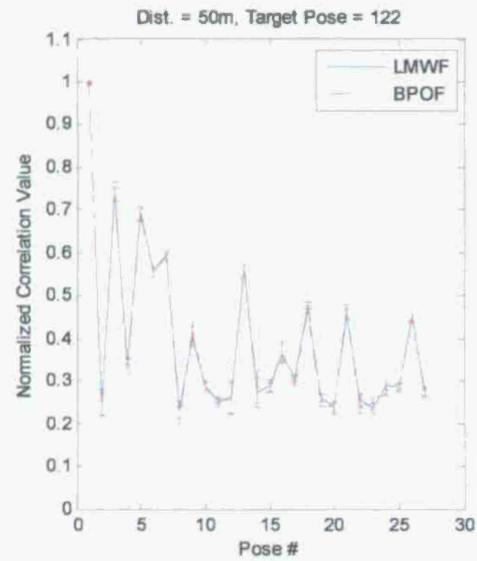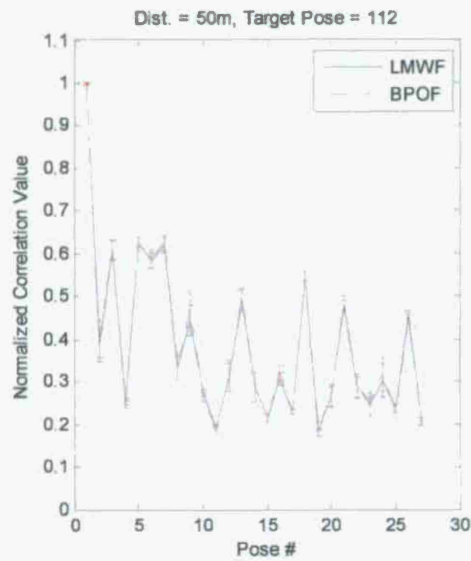
Figure A - 8 Auto and cross correlation peak values for craft at 50m. Target pose is labeled on graph. Neighboring poses are in Table A - 1
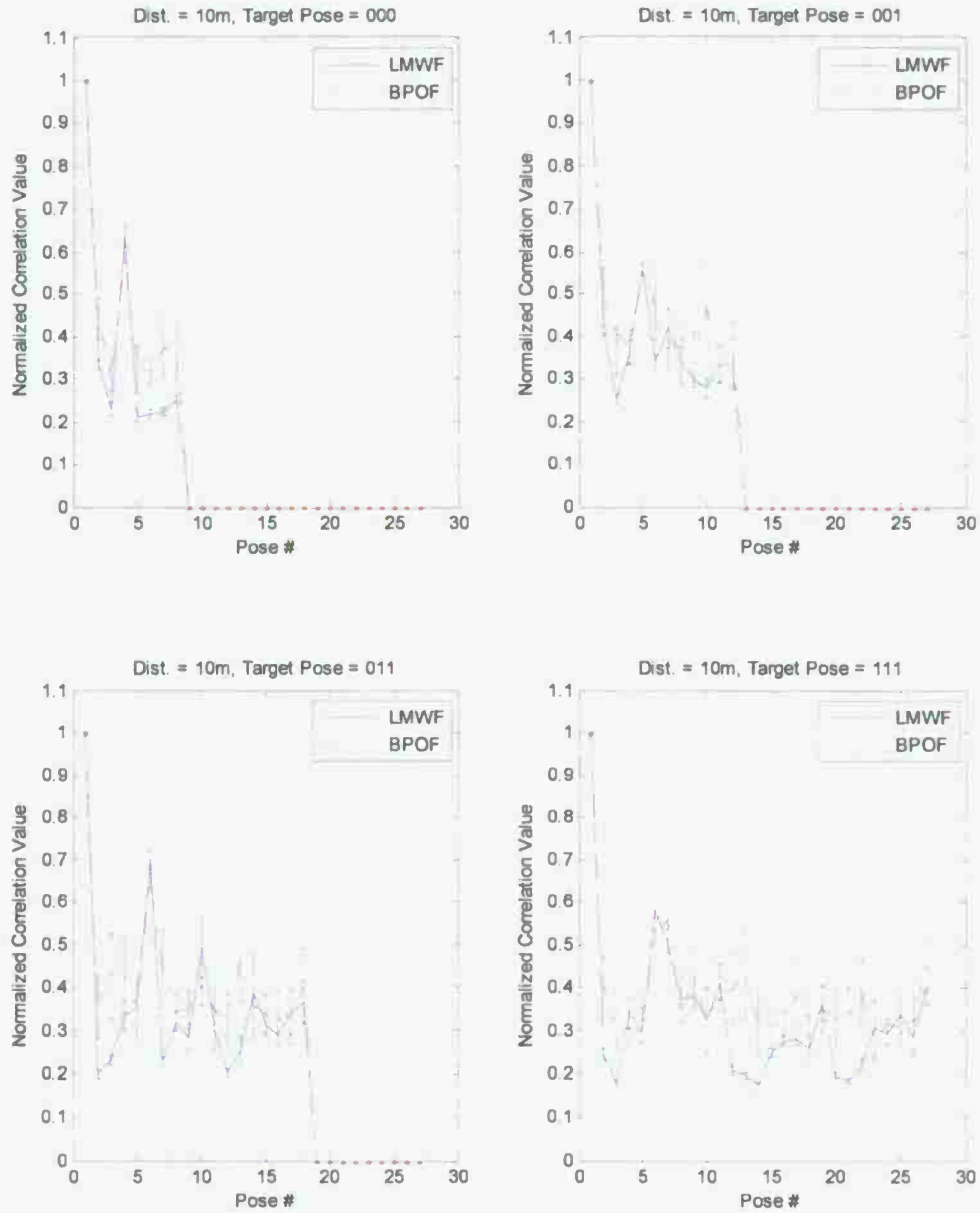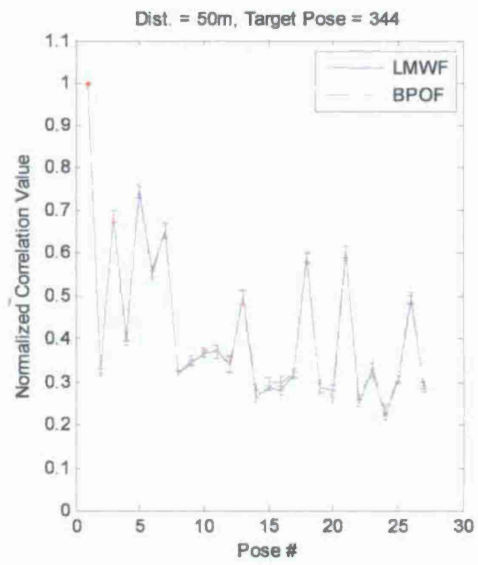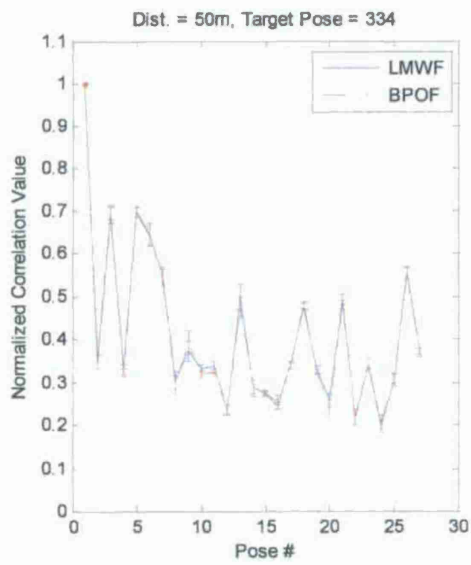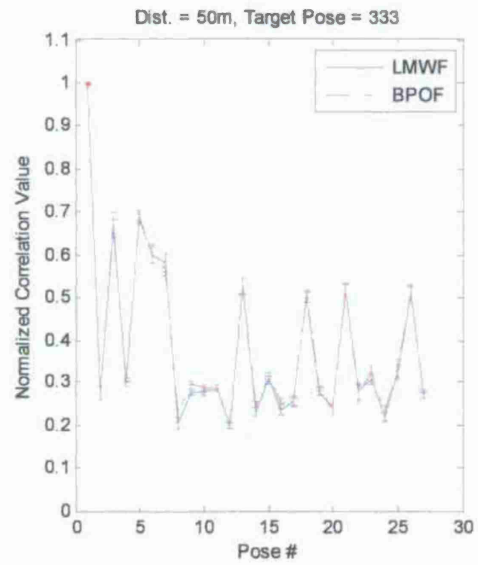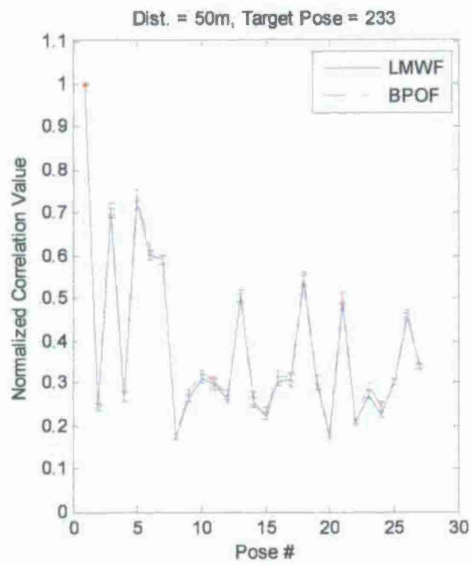
Figure A - 9 Auto and cross correlation peak values for craft at 50m. Target pose is labeled on graph. Neighboring poses are in Table A - 1

108
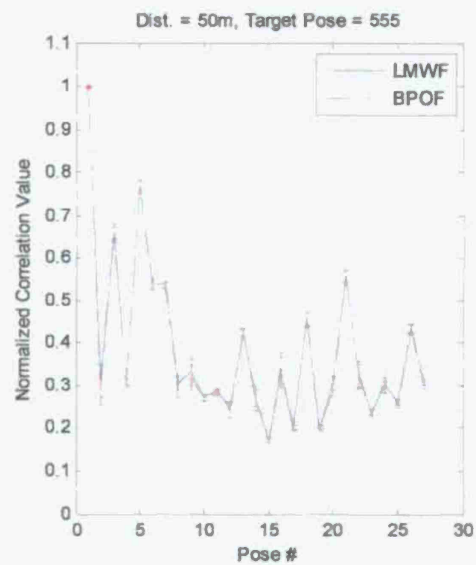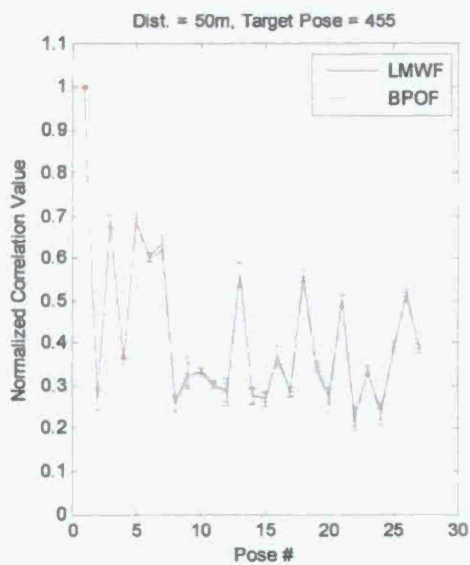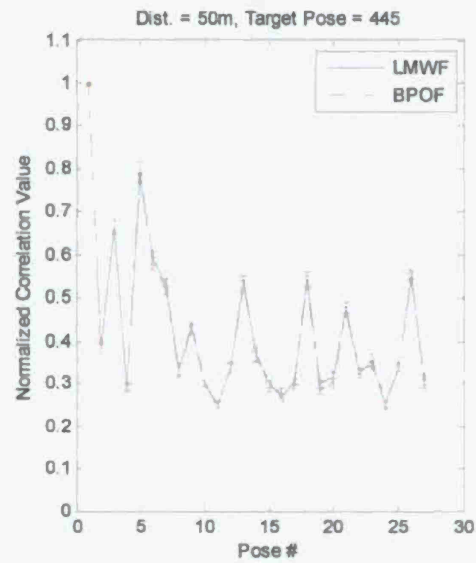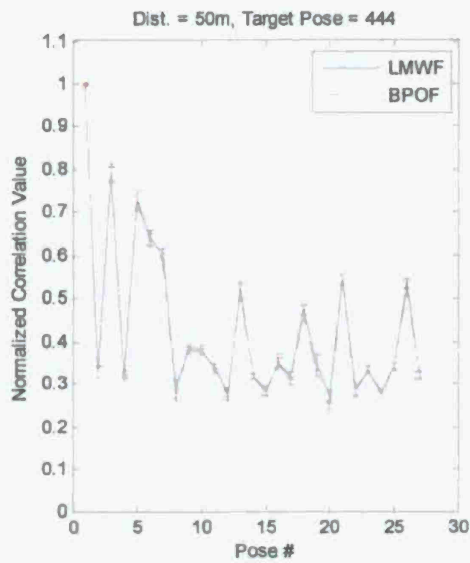
Figure A - 10 Auto and cross correlation peak values for craft at 50m. Target pose is labeled on graph. Neighboring poses are in Table A - 1
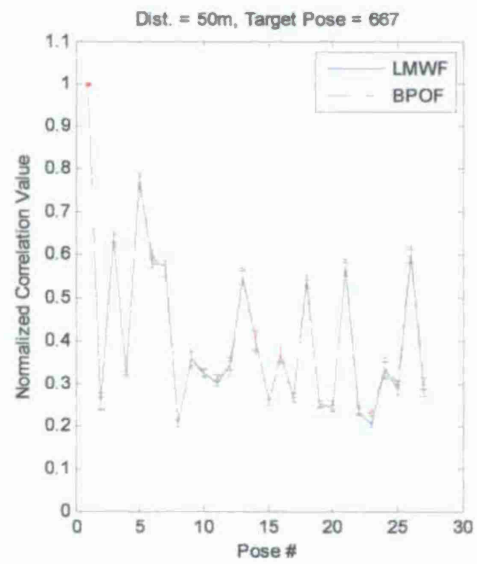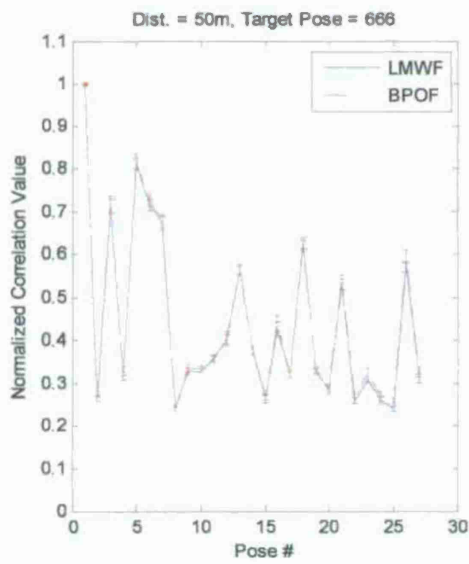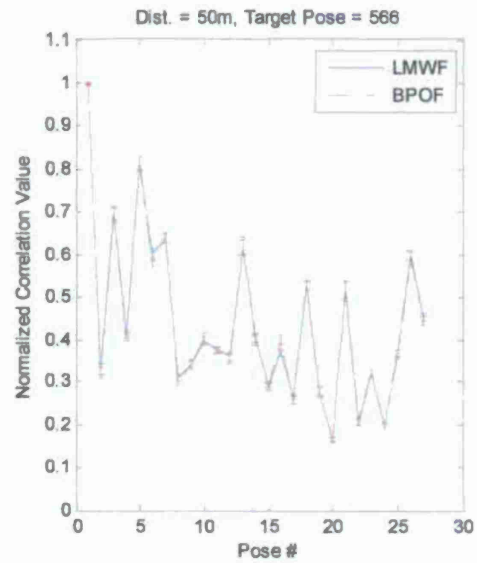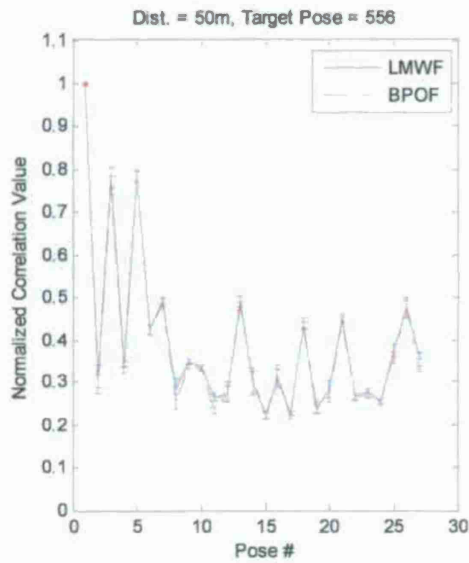
Figure A - 11 Auto and cross correlation peak values for craft at 50m. Target pose is labeled on graph. Neighboring poses are in Table A - 1
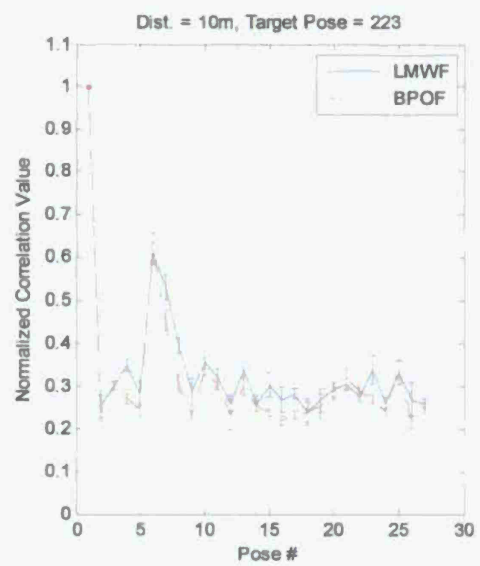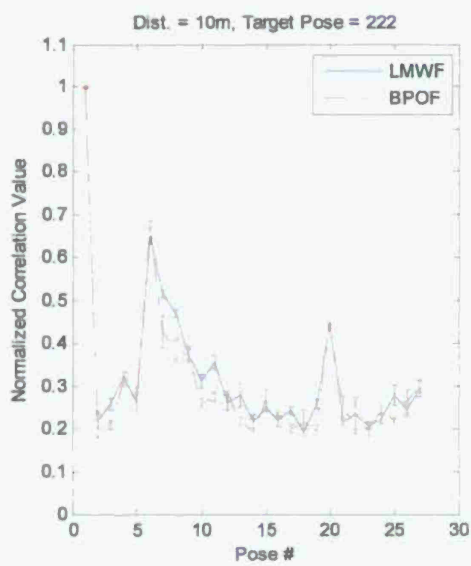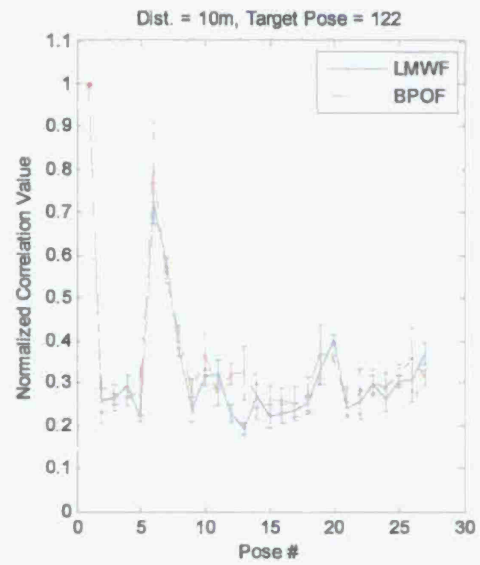
110
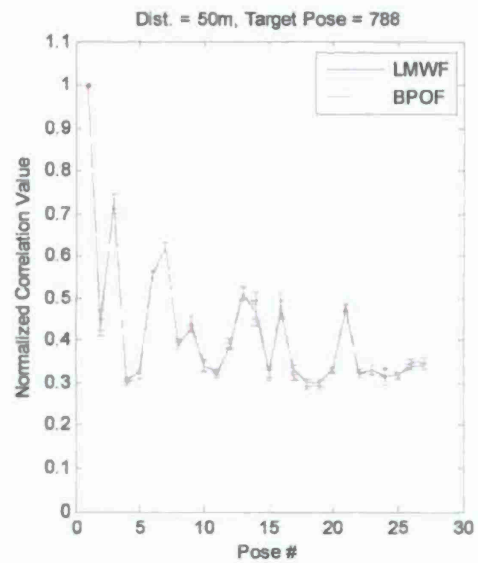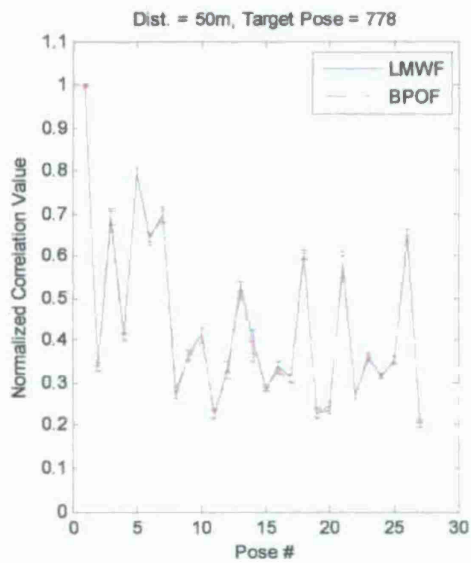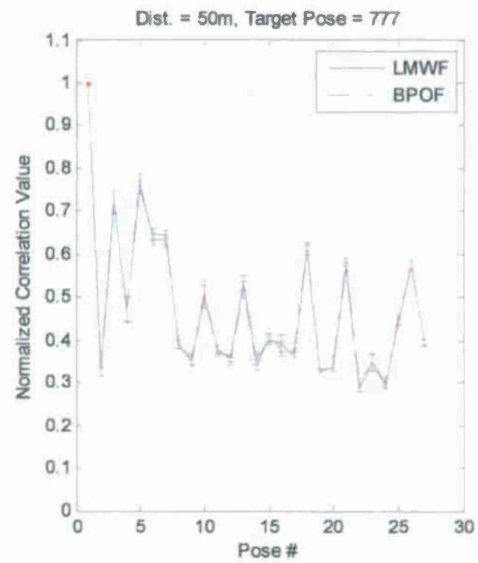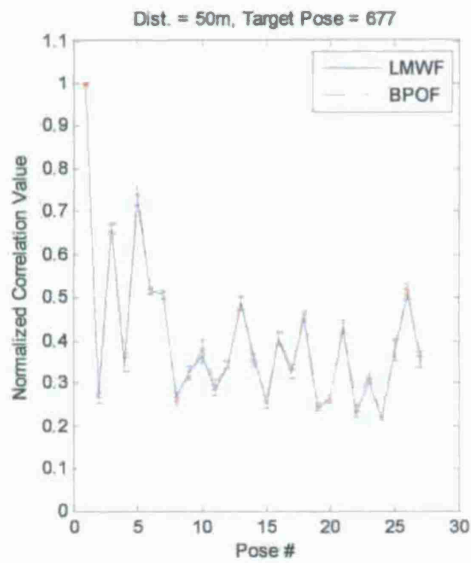
Figure A - 12 Auto and cross correlation peak values for craft at 50m. Target pose is labeled on graph. Neighboring poses are in Table A - 1
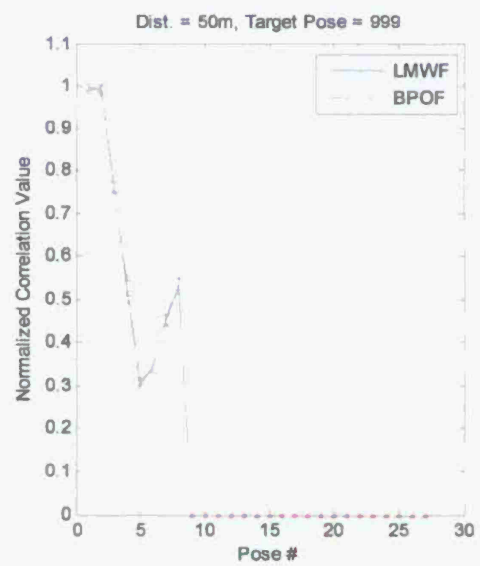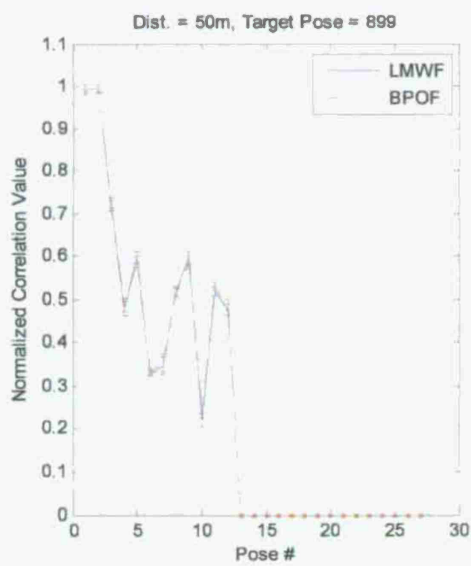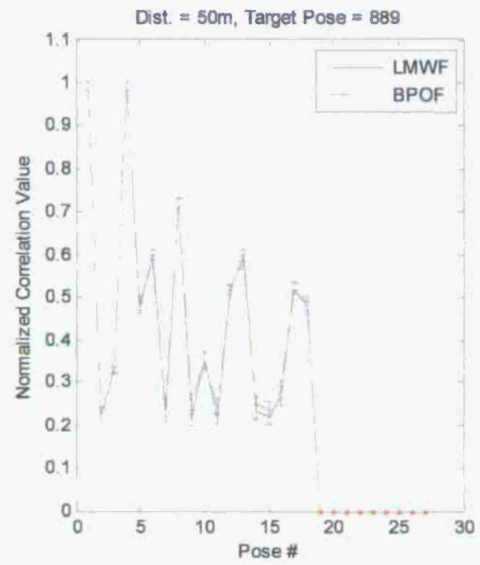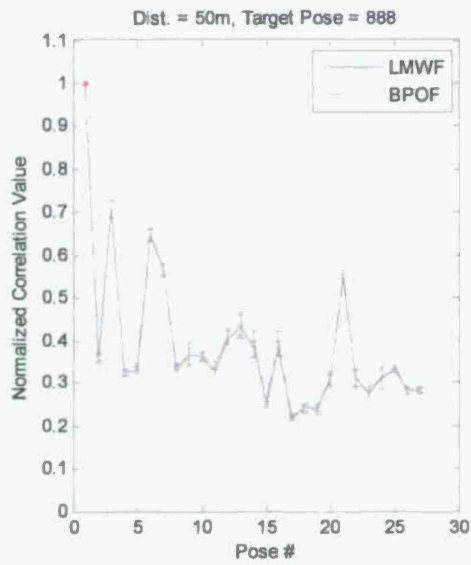
Figure A - 13 Auto and cross correlation peak values for craft at 50m. Target pose is labeled on graph. Neighboring poses are in Table A - 1
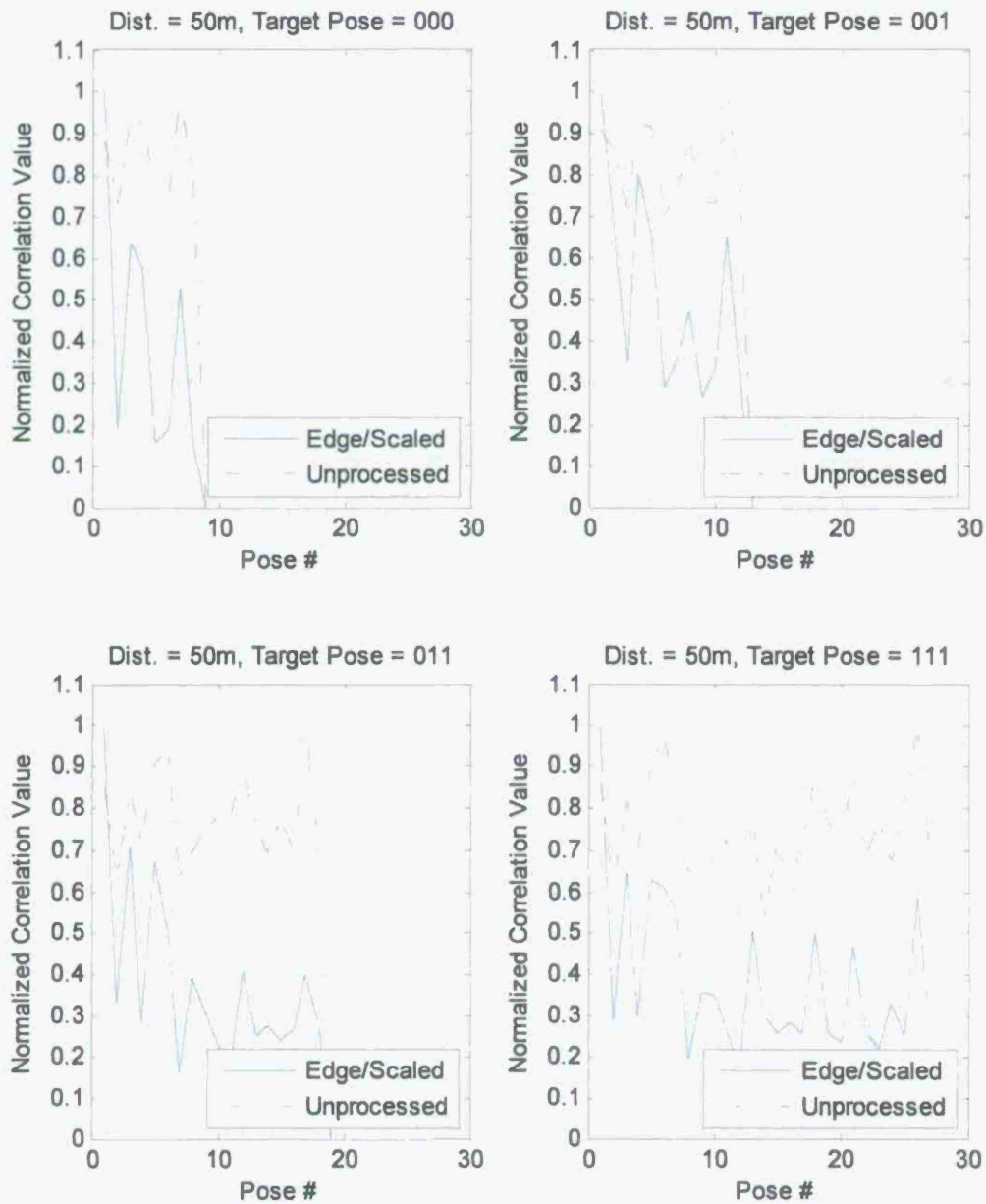
Figure A - 14 Comparison of edge detected and unprocessed image correlations at 50m. The target pose is as indicated. Neighboring poses are in Table A - 1

113
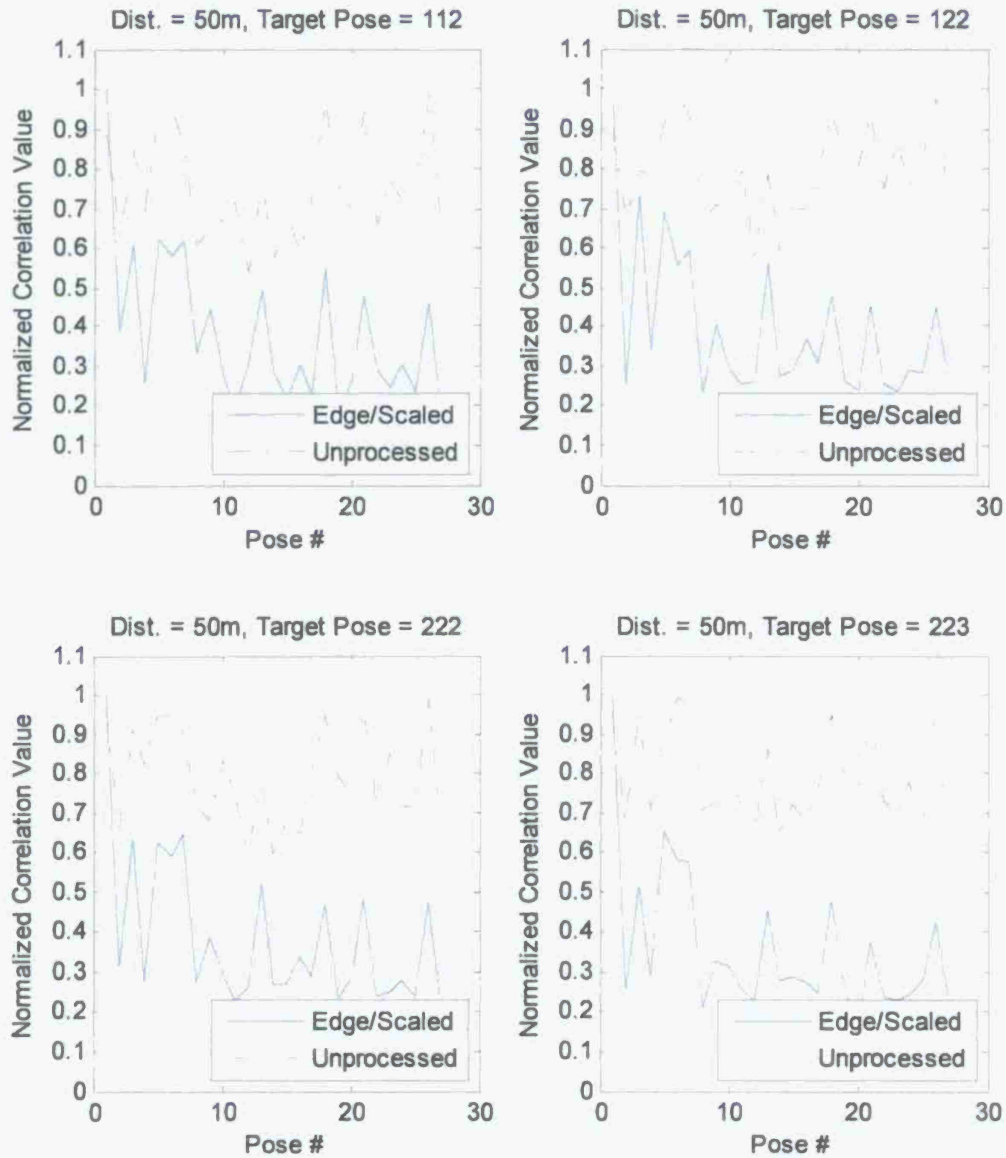
Figure A - 15 Comparison of edge detected and unprocessed image correlations at 50m. The target pose is as indicated. Neighboring poses are in Table A - 1

114
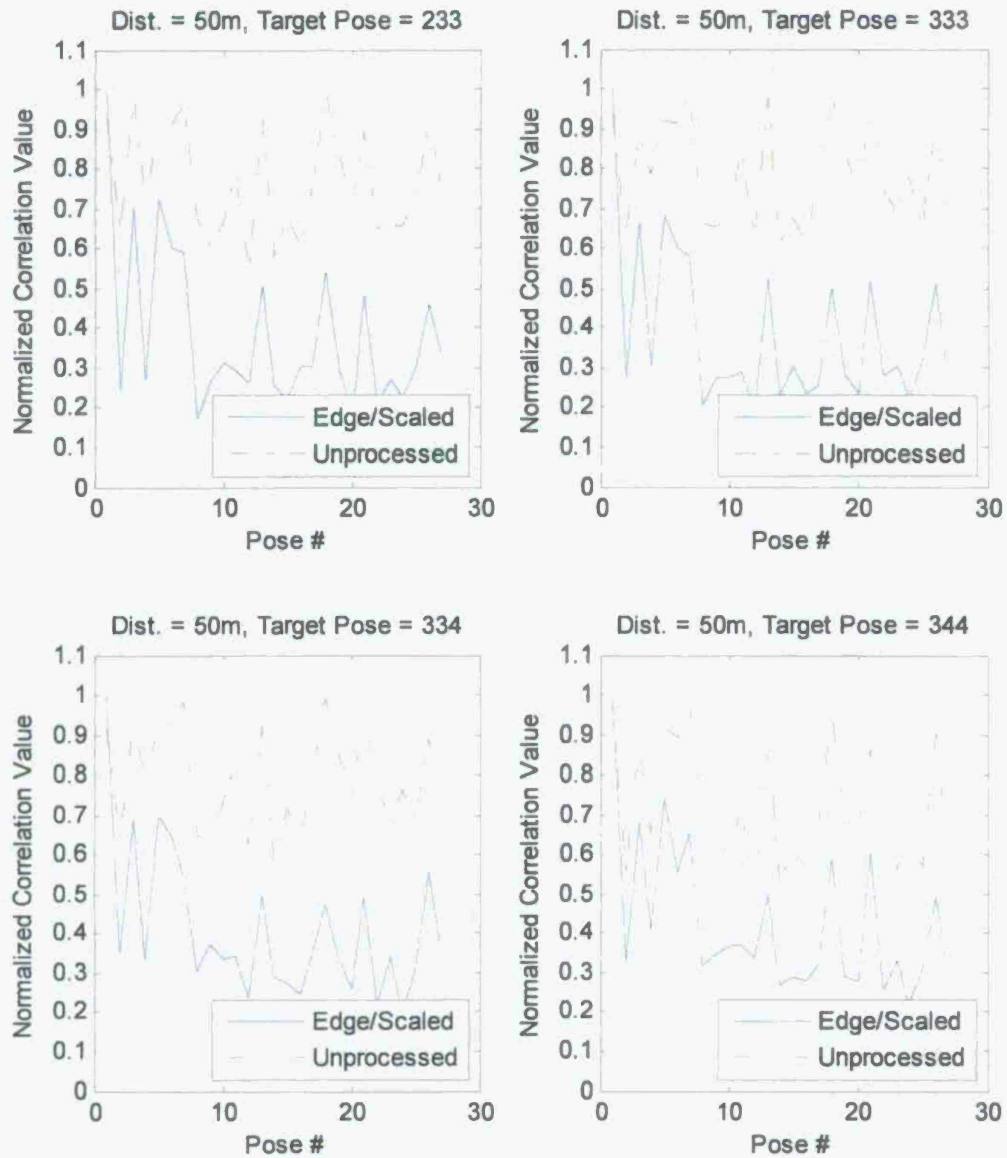
Figure A - 16 Comparison of edge detected and unprocessed image correlations at 50m. The target pose is as indicated. Neighboring poses are in Table A - 1
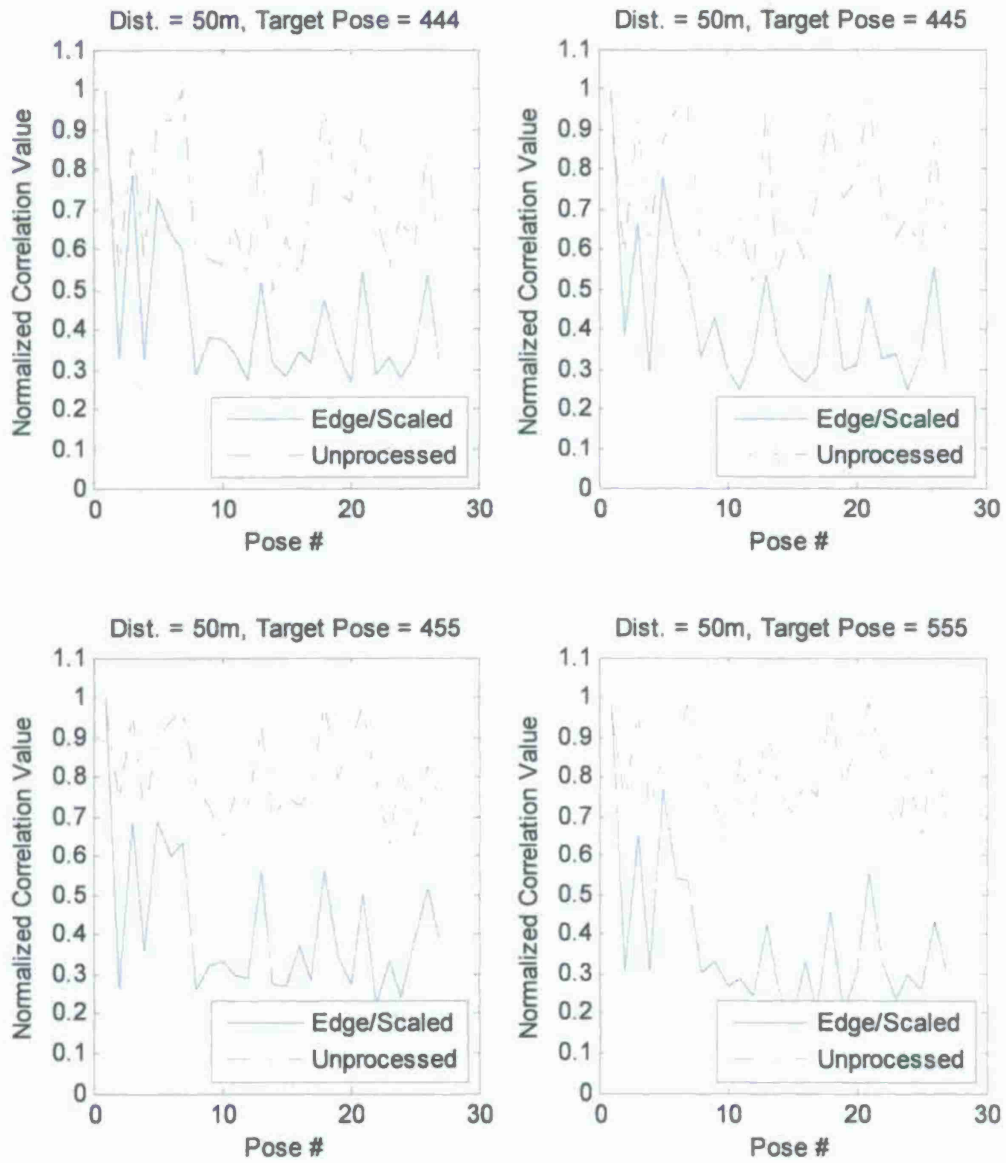
Figure A - 17 Comparison of edge detected and unprocessed image correlations at 50m. The target pose is as indicated. Neighboring poses are in Table A - 1
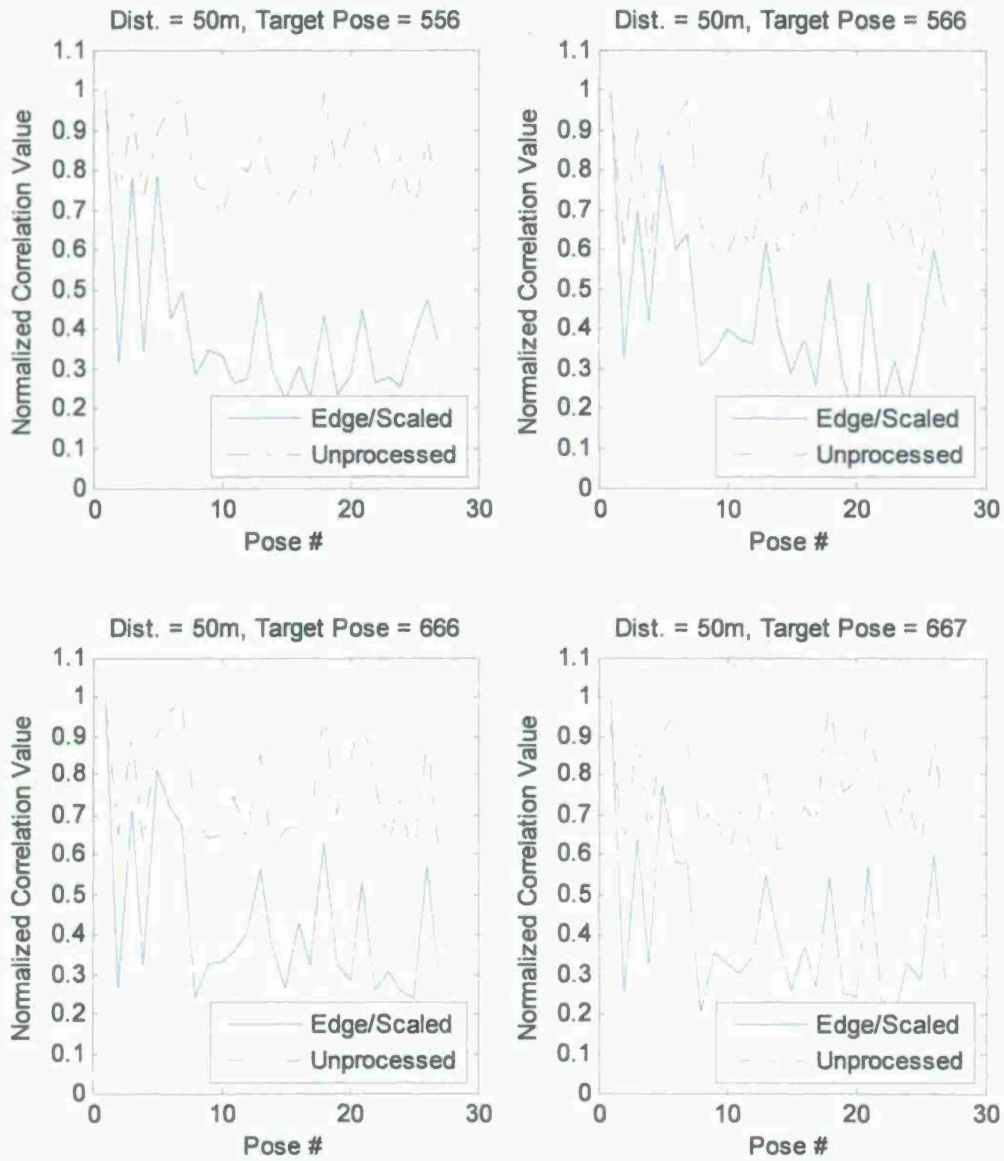
Figure A - 18 Comparison of edge detected and unprocessed image correlations at 50m. The target pose is as indicated. Neighboring poses are in Table A - 1
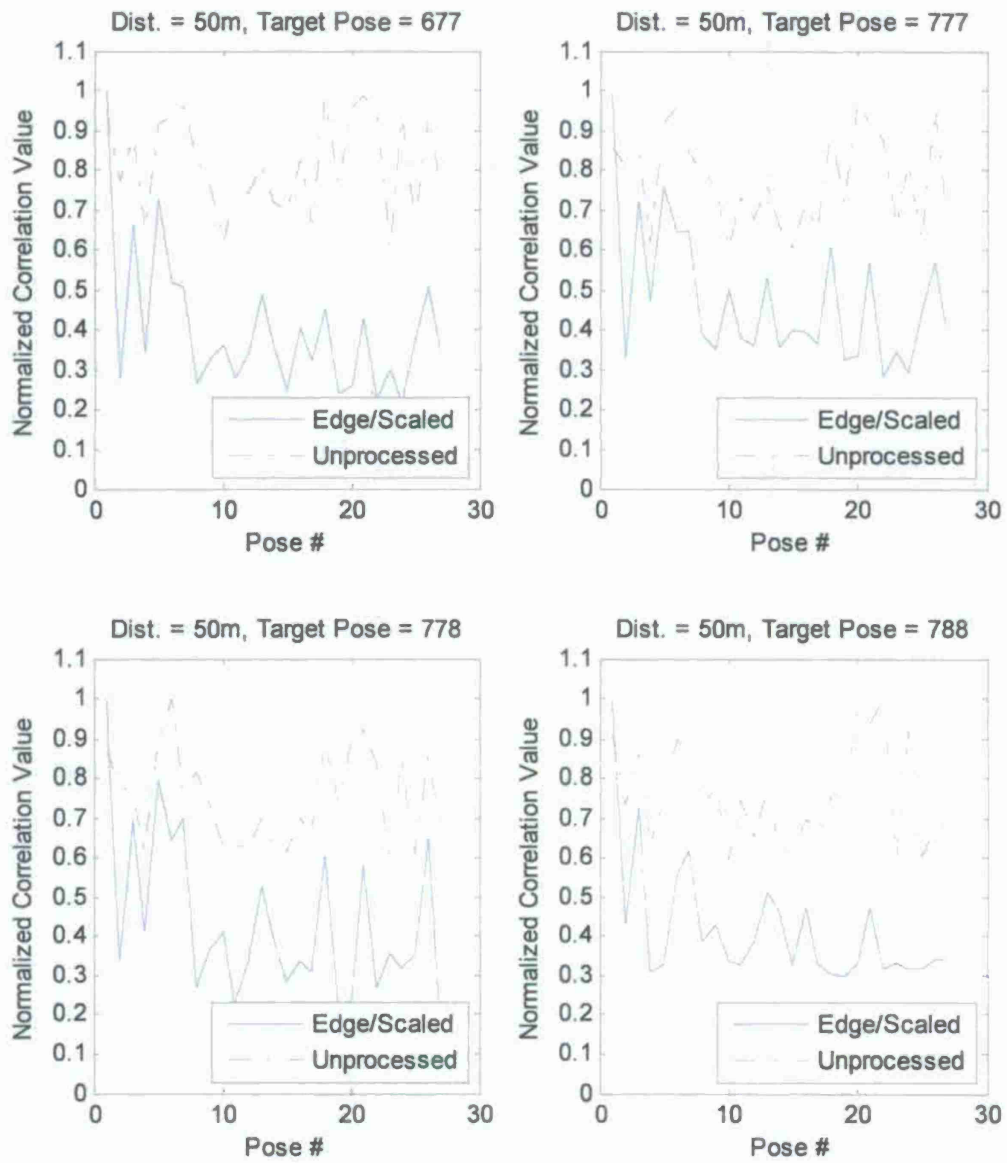
Figure A - 19 Comparison of edge detected and unprocessed image correlations at 50m. The target pose is as indicated. Neighboring poses are in Table A - 1
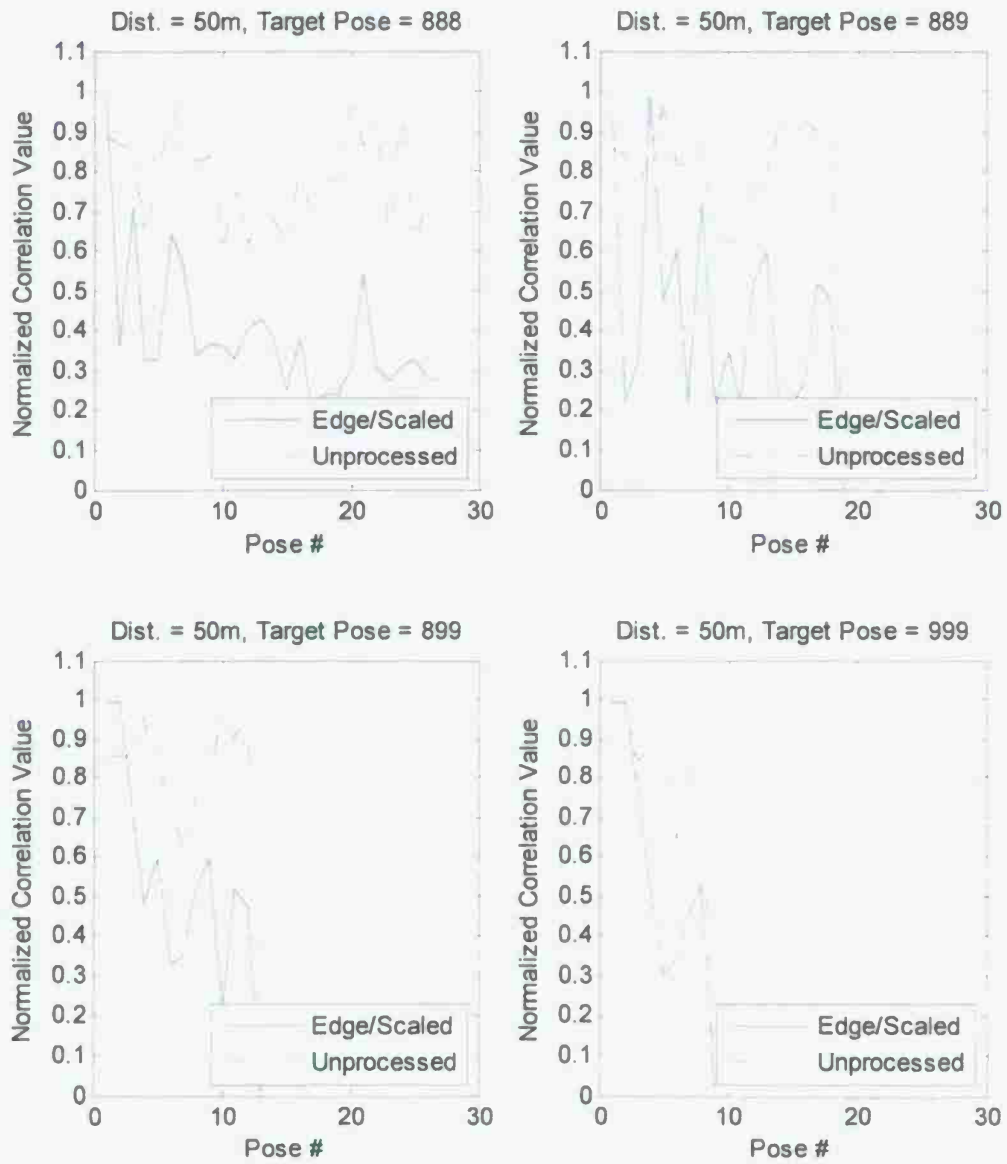
Figure A - 20 Comparison of edge detected and unprocessed image correlations at 50m. The target pose is as indicated. Neighboring poses are in Table A - 1
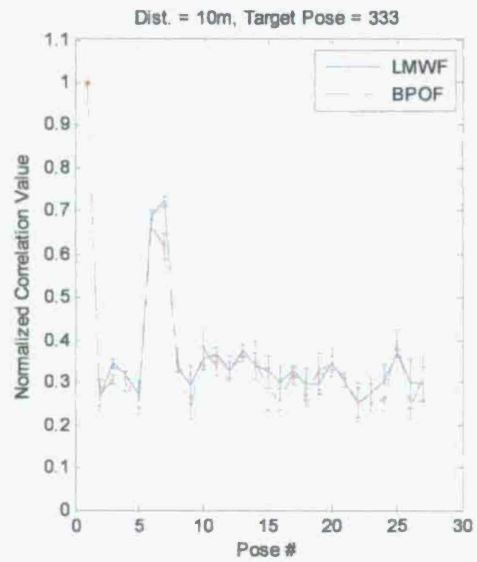
119
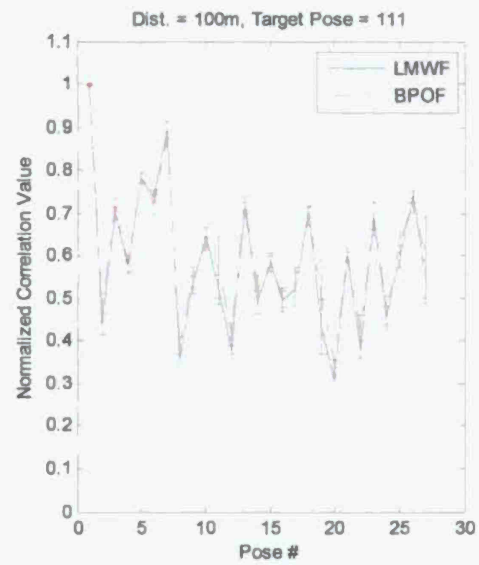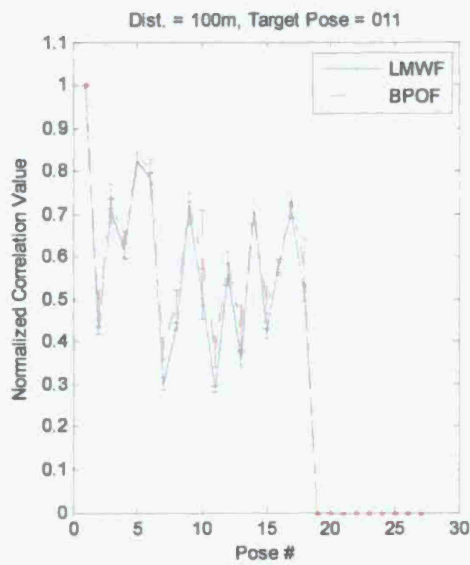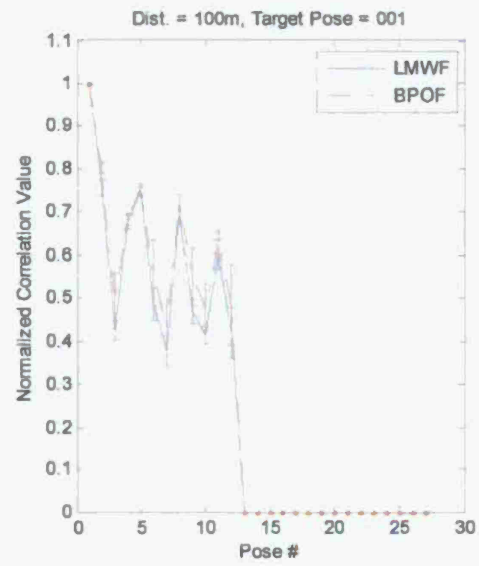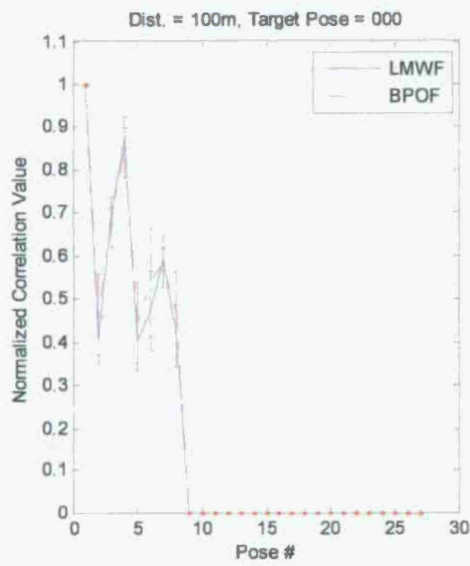
Figure A - 21 Auto and cross correlation peak values for craft at 100m. Target pose is labeled on graph. Neighboring poses are in Table A - 1
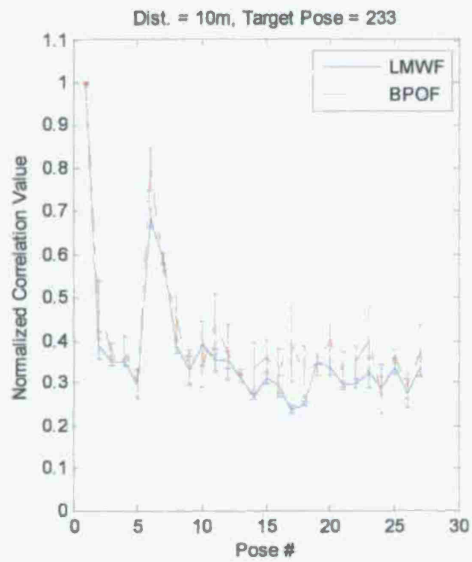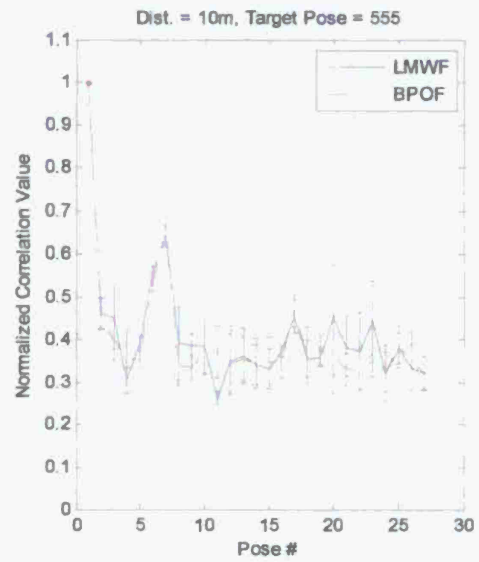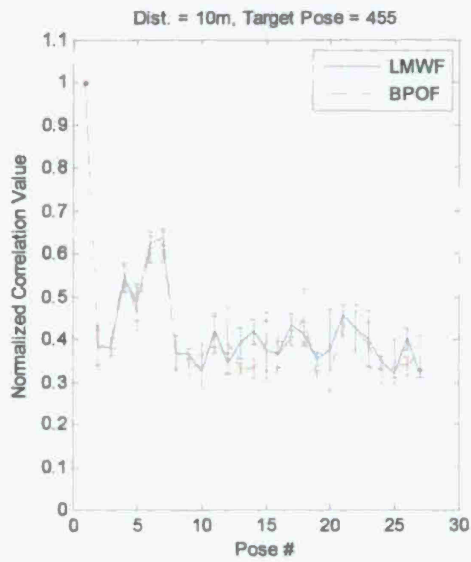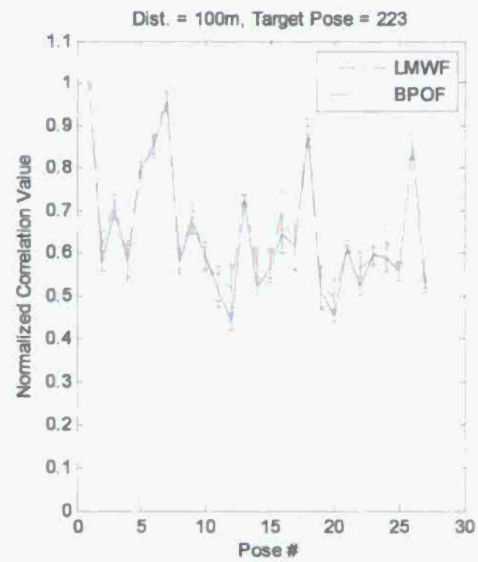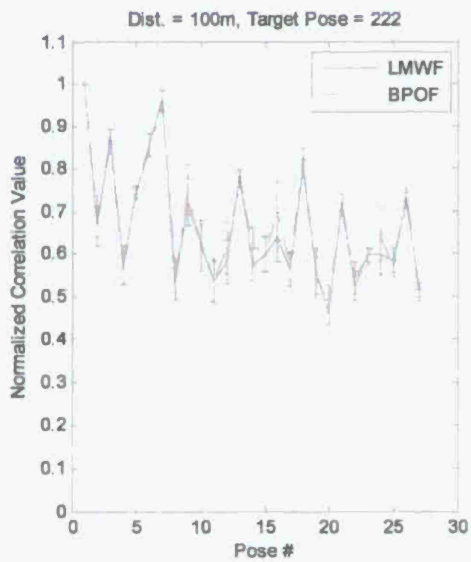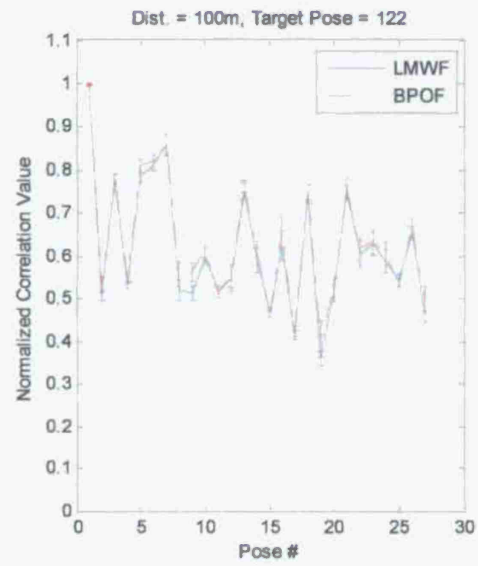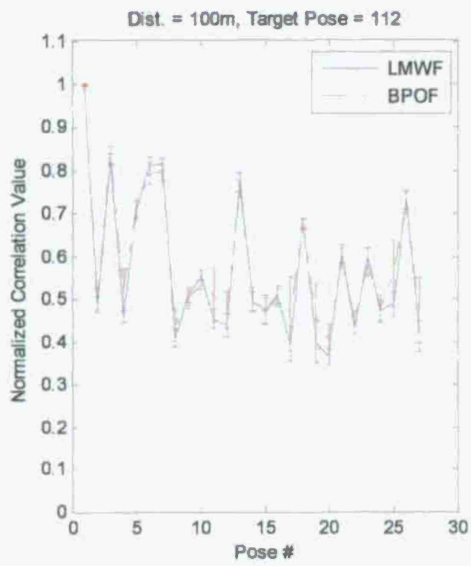
Figure A - 22 Auto and cross correlation peak values for craft at 100m. Target pose is labeled on graph. Neighboring poses are in Table A - 1
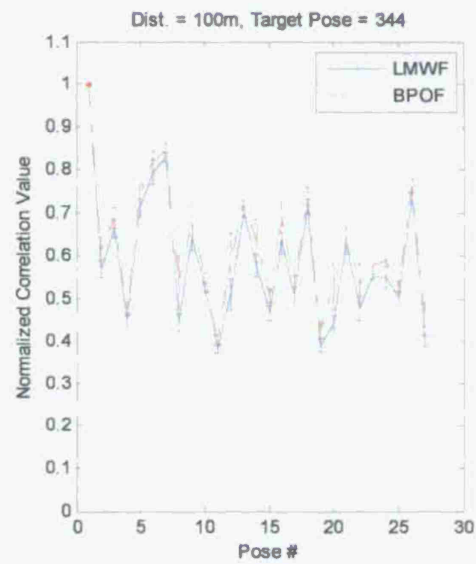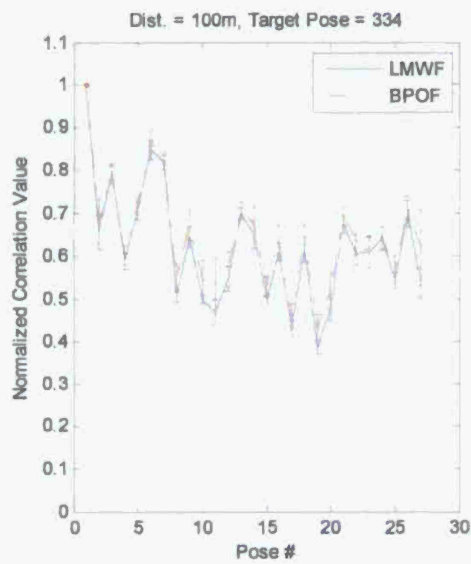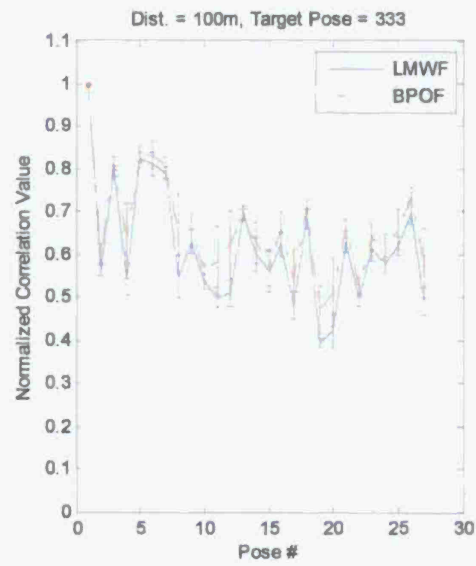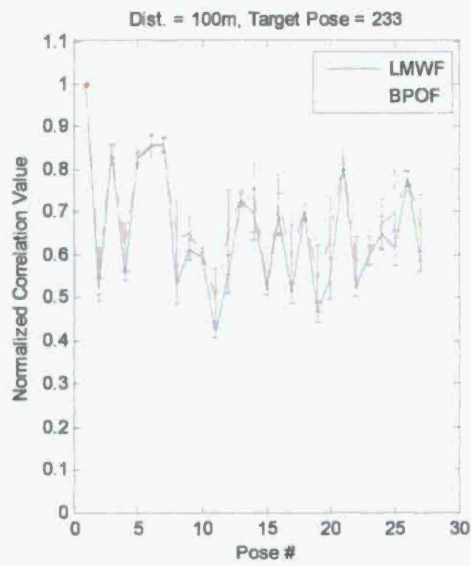
Figure A - 23 Auto and cross correlation peak values for craft at 100m. Target pose is labeled on graph. Neighboring poses are in Table A - 1
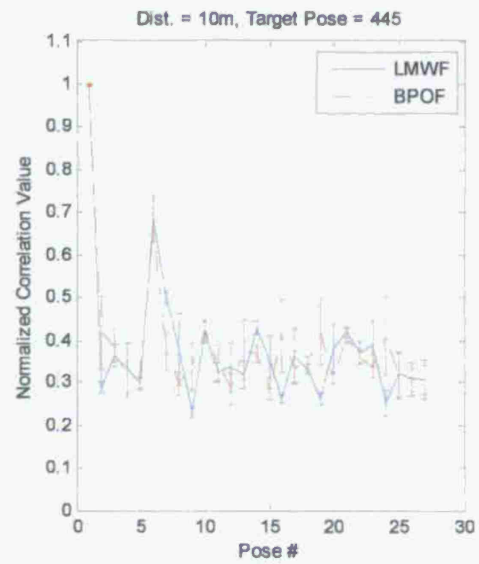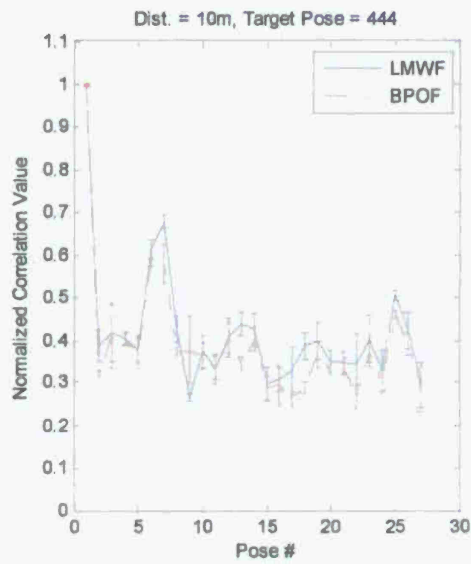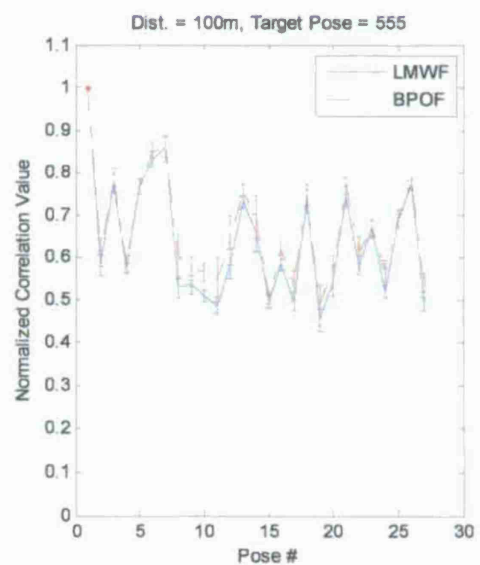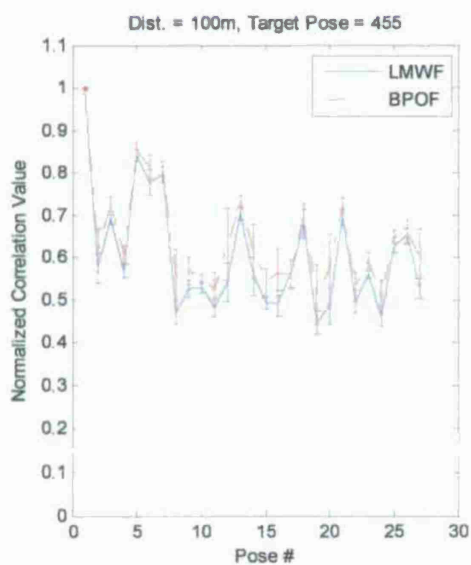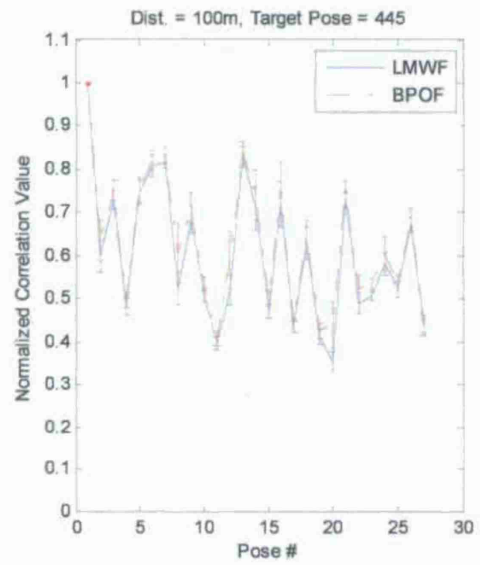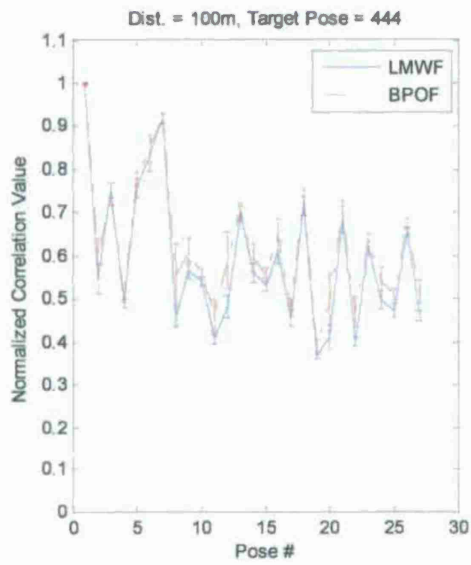
Figure A - 24 Auto and cross correlation peak values for craft at 100m. Target pose is labeled on graph. Neighboring poses are in Table A - 1
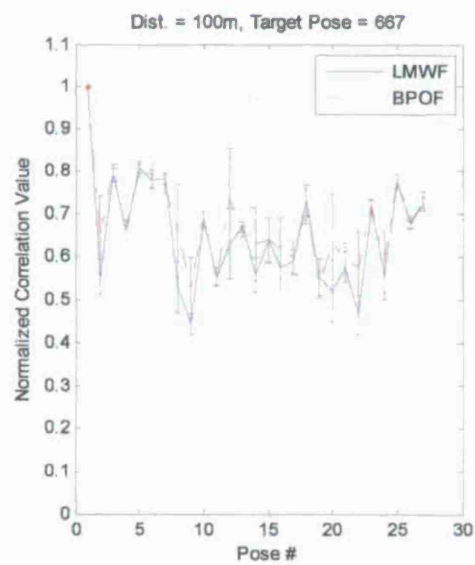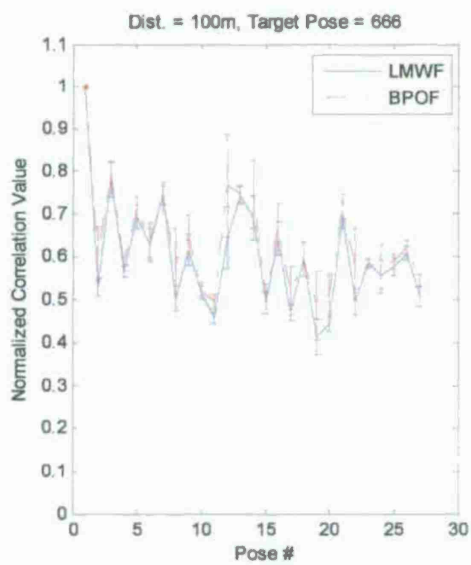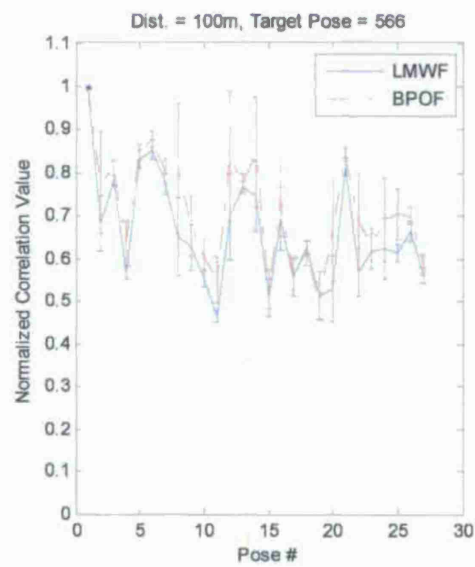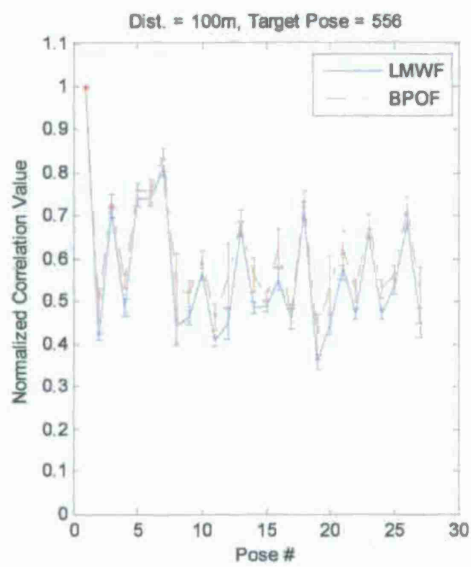
Figure A - 25 Auto and cross correlation peak values for craft at 100m. Target pose is labeled on graph. Neighboring poses are in Table A - 1
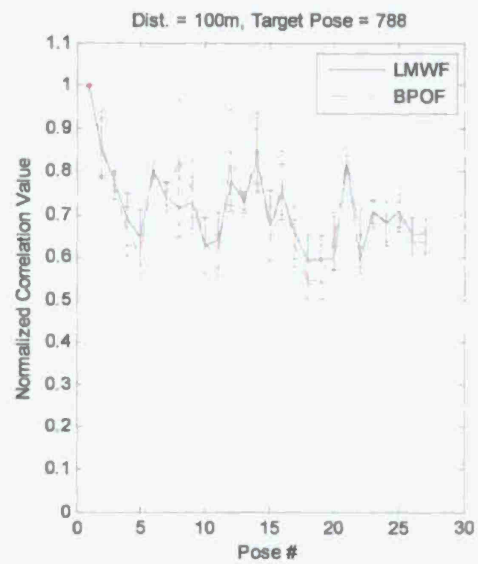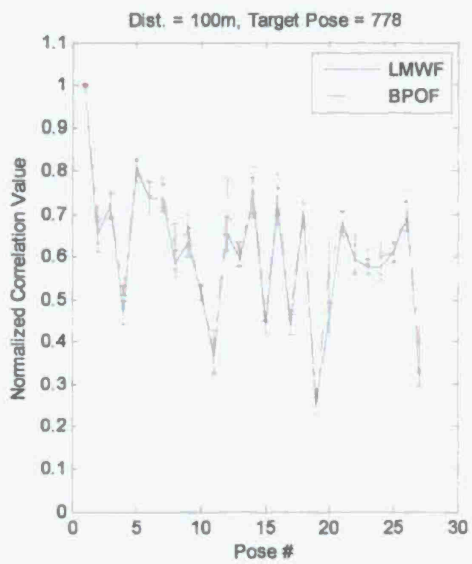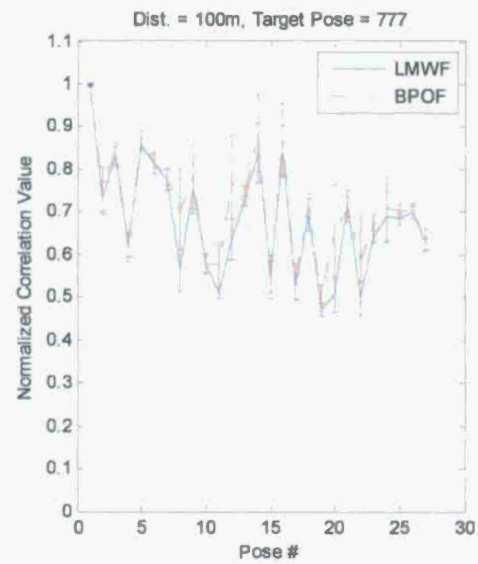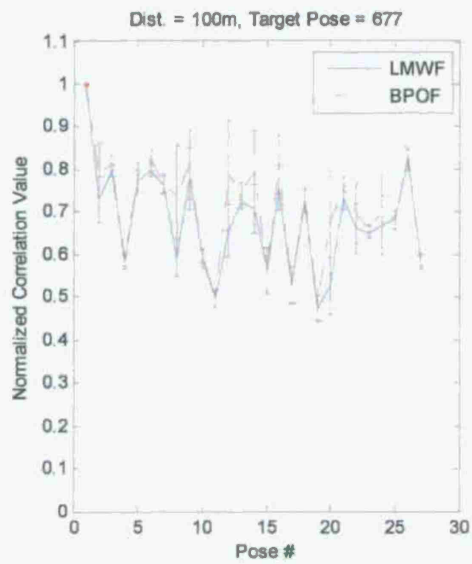
Figure A - 26 Auto and cross correlation peak values for craft at 100m. Target pose is labeled on graph. Neighboring poses are in Table A - 1
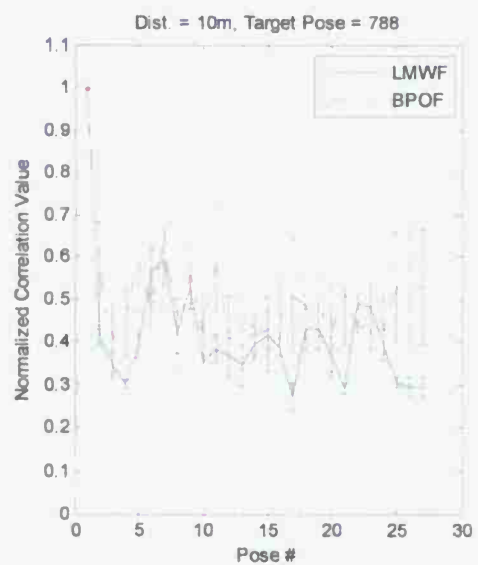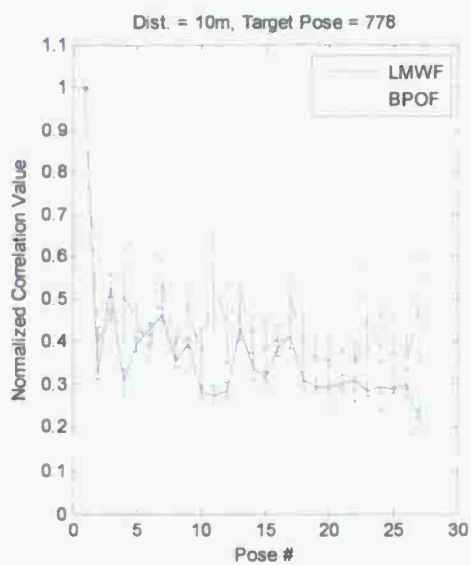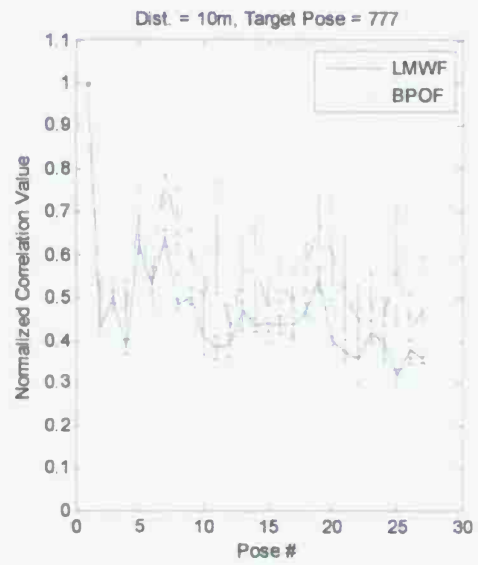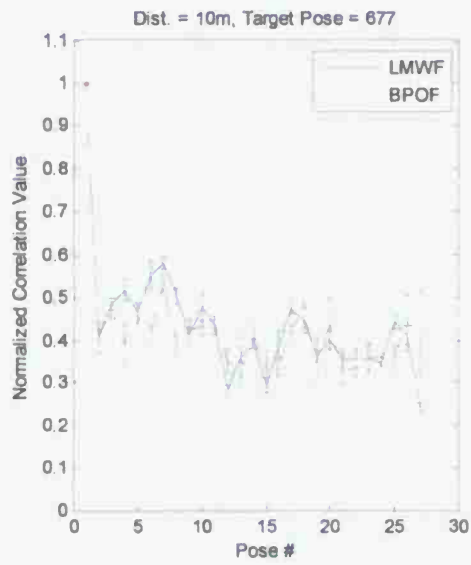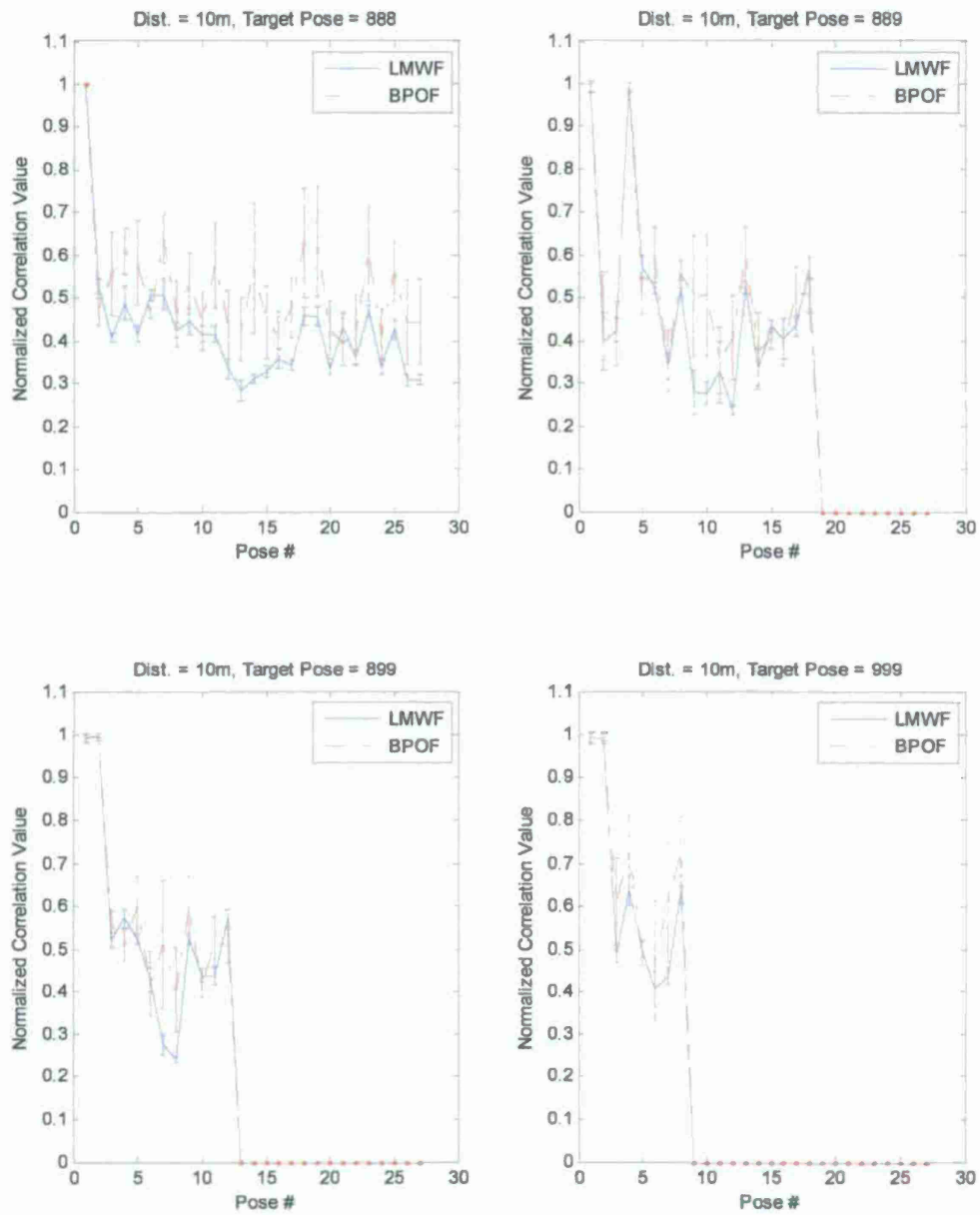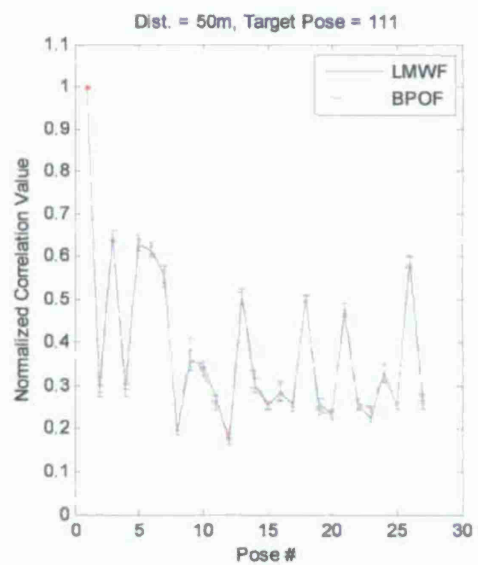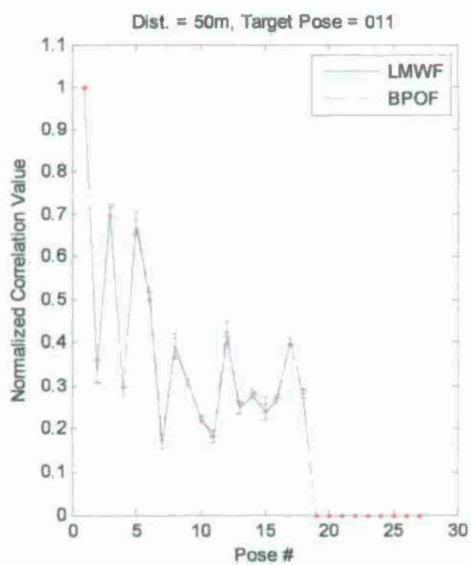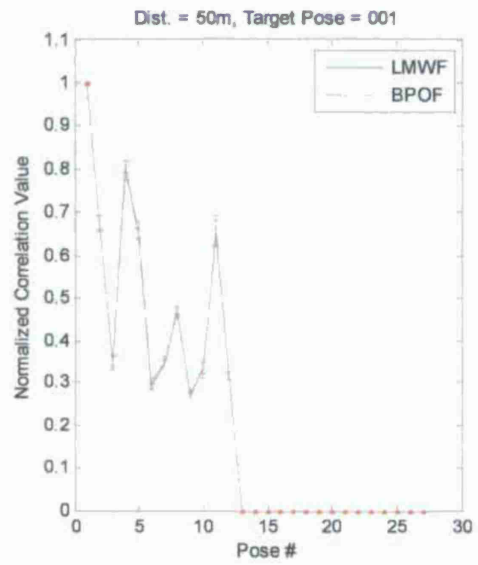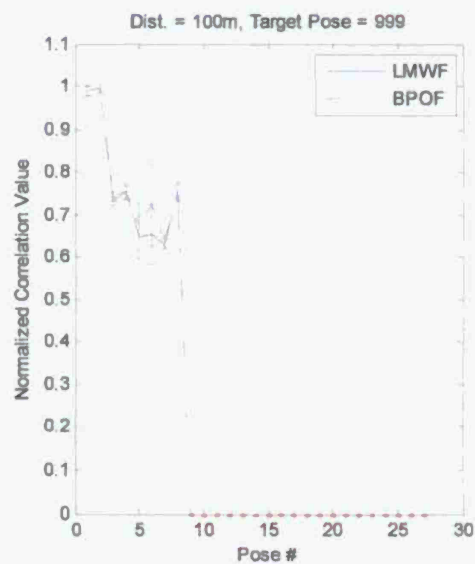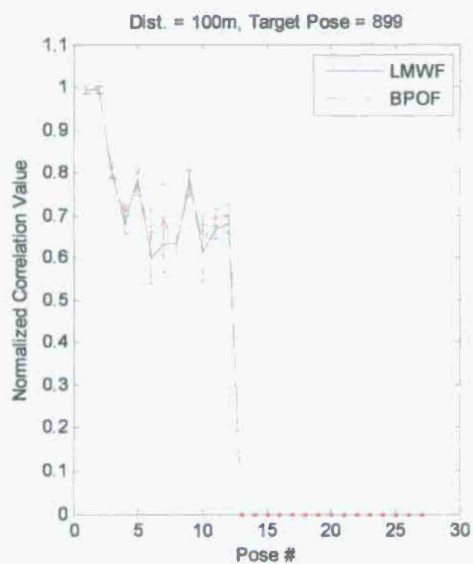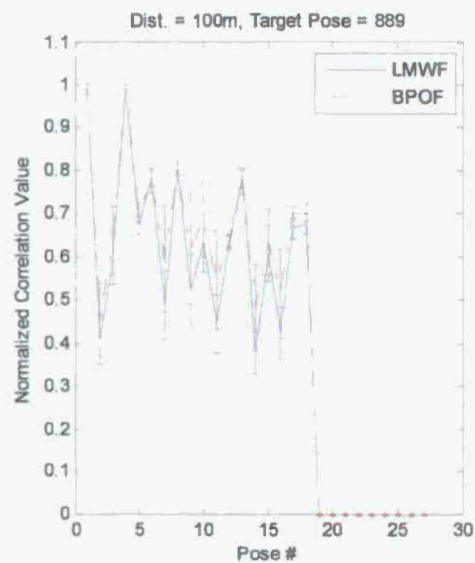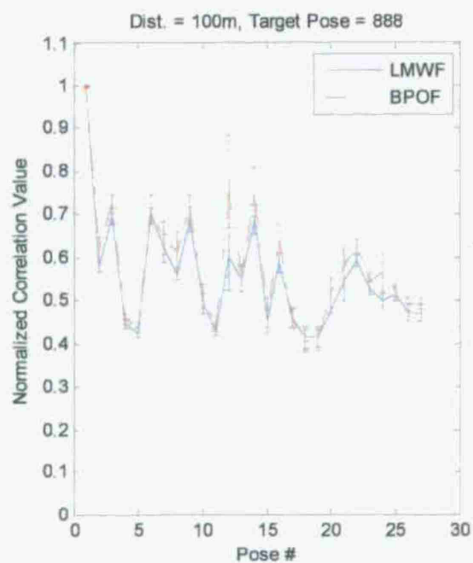
Figure A - 27 Auto and cross correlation peak values for craft at 100m. Target pose is labeled on graph. Neighboring poses are in Table A – 1

	1	2	3	4	5	6	7	8	9	10	11	12	13	14	15	16	17	18	19	20	21	22	23	24	25	26	27
P	0	0	0	1	0	1	1	1	NA	NA	NA	NA	NA	NA	NA	NA	NA	NA	NA	NA	NA	NA	NA	NA	NA	NA	NA
Y	0	1	0	0	1	1	0	1	NA	NA	NA	NA	NA	NA	NA	NA	NA	NA	NA	NA	NA	NA	NA	NA	NA	NA	NA
R	0	0	1	0	1	0	1	1	NA	NA	NA	NA	NA	NA	NA	NA	NA	NA	NA	NA	NA	NA	NA	NA	NA	NA	NA
	0	0	0	0	1	0	0	1	1	1	1	1	NA	NA	NA	NA	NA	NA	NA	NA	NA	NA	NA	NA	NA	NA	NA
	0	0	1	0	0	1	1	0	1	1	0	1	NA	NA	NA	NA	NA	NA	NA	NA	NA	NA	NA	NA	NA	NA	NA
	1	0	1	2	1	0	2	0	0	1	2	2	NA	NA	NA	NA	NA	NA	NA	NA	NA	NA	NA	NA	NA	NA	NA
	0	0	0	0	0	1	0	0	0	0	1	1	1	1	1	1	1	1	NA	NA	NA	NA	NA	NA	NA	NA	NA
	1	0	1	2	1	1	0	0	2	2	0	1	0	2	0	2	1	2	NA	NA	NA	NA	NA	NA	NA	NA	NA
	1	1	0	1	2	1	0	2	0	2	0	0	1	0	2	1	2	2	NA	NA	NA	NA	NA	NA	NA	NA	NA
	1	1	1	1	1	2	0	1	1	1	1	0	0	0	0	0	0	0	0	2	2	2	2	2	2	2	2
	1	0	1	2	1	1	1	0	0	2	2	0	1	0	2	0	2	1	2	0	1	0	2	0	2	1	2
	1	1	0	1	2	1	1	0	2	0	2	0	0	1	0	2	1	2	2	0	0	1	0	2	1	2	2
	1	1	1	1	1	2	0	1	1	1	1	0	0	0	0	0	0	0	0	2	2	2	2	2	2	2	2
	1	0	1	2	1	1	1	0	0	2	2	0	1	0	2	0	2	1	2	0	1	0	2	0	2	1	2
	2	2	1	2	3	2	2	1	3	1	3	1	1	2	1	3	2	3	3	1	1	2	1	3	2	3	3
	1	1	1	1	1	2	0	1	1	1	1	0	0	0	0	0	0	0	0	2	2	2	2	2	2	2	2
	2	1	2	3	2	2	2	1	1	3	3	1	2	1	3	1	3	2	3	1	2	1	3	1	3	2	3
	2	2	1	2	3	2	2	1	3	1	3	1	1	2	1	3	2	3	3	1	1	2	1	3	2	3	3
	2	2	2	2	2	3	1	2	2	2	2	1	1	1	1	1	1	1	1	3	3	3	3	3	3	3	3
	2	1	2	3	2	2	2	1	1	3	3	1	2	1	3	1	3	2	3	1	2	1	3	1	3	2	3
	2	2	1	2	3	2	2	1	3	1	3	1	1	2	1	3	2	3	3	1	1	2	1	3	2	3	3

Table A- 1 Table of neighboring poses for each target Pose # 1

127

Pose #

	1	2	3	4	5	6	7	8	9	10	11	12	13	14	15	16	17	18	19	20	21	22	23	24	25	26	27
P	2	2	2	2	2	3	1	2	2	2	2	1	1	1	1	1	1	1	1	3	3	3	3	3	3	3	3
Y	2	1	2	3	2	2	2	1	1	3	3	1	2	1	3	1	3	2	3	1	2	1	3	1	3	2	3
R	3	3	2	3	4	3	3	2	4	2	4	2	2	3	2	4	3	4	4	2	2	3	2	4	3	4	4
	2	2	2	2	2	3	1	2	2	2	2	1	1	1	1	1	1	1	1	3	3	3	3	3	3	3	3
	3	2	3	4	3	3	3	2	2	4	4	2	3	2	4	2	4	3	4	2	3	2	4	2	4	3	4
	3	3	2	3	4	3	3	2	4	2	4	2	2	3	2	4	3	4	4	2	2	3	2	4	3	4	4
	3	3	3	3	3	4	2	3	3	3	3	2	2	2	2	2	2	2	2	4	4	4	4	4	4	4	4
	3	2	3	4	3	3	3	2	2	4	4	2	3	2	4	2	4	3	4	2	3	2	4	2	4	3	4
	3	3	2	3	4	3	3	2	4	2	4	2	2	3	2	4	3	4	4	2	2	3	2	4	3	4	4
	3	3	3	3	3	4	2	3	3	3	3	2	2	2	2	2	2	2	2	4	4	4	4	4	4	4	4
	3	2	3	4	3	3	3	2	2	4	4	2	3	2	4	2	4	3	4	2	3	2	4	2	4	3	4
	4	4	3	4	5	4	4	3	5	3	5	3	3	4	3	5	4	5	5	3	3	4	3	5	4	5	5
	3	3	3	3	3	4	2	3	3	3	3	2	2	2	2	2	2	2	2	4	4	4	4	4	4	4	4
	4	3	4	5	4	4	4	3	3	5	5	3	4	3	5	3	5	4	5	3	4	3	5	3	5	4	5
	4	4	3	4	5	4	4	3	5	3	5	3	3	4	3	5	4	5	5	3	3	4	3	5	4	5	5
	4	4	4	4	4	5	3	4	4	4	4	3	3	3	3	3	3	3	3	5	5	5	5	5	5	5	5
	4	3	4	5	4	4	4	3	3	5	5	3	4	3	5	3	5	4	5	3	4	3	5	3	5	4	5
	4	4	3	4	5	4	4	3	5	3	5	3	3	4	3	5	4	5	5	3	3	4	3	5	4	5	5
	4	4	4	4	4	5	3	4	4	4	4	3	3	3	3	3	3	3	3	5	5	5	5	5	5	5	5
	4	3	4	5	4	4	4	3	3	5	5	3	4	3	5	3	5	4	5	3	4	3	5	3	5	4	5
	5	5	4	5	6	5	5	4	6	4	6	4	4	5	4	6	5	6	6	4	4	5	4	6	5	6	6

Table A-1 Cont.

128

	1	2	3	4	5	6	7	8	9	10	11	12	13	14	15	16	17	18	19	20	21	22	23	24	25	26	27
P	4	4	4	4	4	5	3	4	4	4	4	3	3	3	3	3	3	3	3	5	5	5	5	5	5	5	5
Y	5	4	5	6	5	5	5	4	4	6	6	4	5	4	6	4	6	5	6	4	5	4	6	4	6	5	6
R	5	5	4	5	6	5	5	4	6	4	6	4	4	5	4	6	5	6	6	4	4	5	4	6	5	6	6
	5	5	5	5	5	6	4	5	5	5	5	4	4	4	4	4	4	4	4	6	6	6	6	6	6	6	6
	5	4	5	6	5	5	5	4	4	6	6	4	5	4	6	4	6	5	6	4	5	4	6	4	6	5	6
	5	5	4	5	6	5	5	4	6	4	6	4	4	5	4	6	5	6	6	4	4	5	4	6	5	6	6
	5	5	5	5	5	6	4	5	5	5	5	4	4	4	4	4	4	4	4	6	6	6	6	6	6	6	6
	5	4	5	6	5	5	5	4	4	6	6	4	5	4	6	4	6	5	6	4	5	4	6	4	6	5	6
	6	6	5	6	7	6	6	5	7	5	7	5	5	6	5	7	6	7	7	5	5	6	5	7	6	7	7
	5	5	5	5	5	6	4	5	5	5	5	4	4	4	4	4	4	4	4	6	6	6	6	6	6	6	6
	6	5	6	7	6	6	6	5	5	7	7	5	6	5	7	5	7	6	7	5	6	5	7	5	7	6	7
	6	6	5	6	7	6	6	5	7	5	7	5	5	6	5	7	6	7	7	5	5	6	5	7	6	7	7
	6	6	6	6	6	7	5	6	6	6	6	5	5	5	5	5	5	5	5	7	7	7	7	7	7	7	7
	6	5	6	7	6	6	6	5	5	7	7	5	6	5	7	5	7	6	7	5	6	5	7	5	7	6	7
	6	6	5	6	7	6	6	5	7	5	7	5	5	6	5	7	6	7	7	5	5	6	5	7	6	7	7
	6	6	6	6	6	7	5	6	6	6	6	5	5	5	5	5	5	5	5	7	7	7	7	7	7	7	7
	6	5	6	7	6	6	6	5	5	7	7	5	6	5	7	5	7	6	7	5	6	5	7	5	7	6	7
	7	7	6	7	8	7	7	6	8	6	8	6	6	7	6	8	7	8	8	6	6	7	6	8	7	8	8
	6	6	6	6	6	7	5	6	6	6	6	5	5	5	5	5	5	5	5	7	7	7	7	7	7	7	7
	7	6	7	8	7	7	7	6	6	8	8	6	7	6	8	6	8	7	8	6	7	6	8	6	8	7	8
	7	7	6	7	8	7	7	6	8	6	8	6	6	7	6	8	7	8	8	6	6	7	6	8	7	8	8

Table A-1 Cont

129

Pose #

	1	2	3	4	5	6	7	8	9	10	11	12	13	14	15	16	17	18	19	20	21	22	23	24	25	26	27
P	7	7	7	7	7	8	6	7	7	7	7	6	6	6	6	6	6	6	6	8	8	8	8	8	8	8	8
Y	7	6	7	8	7	7	7	6	6	8	8	6	7	6	8	6	8	7	8	6	7	6	8	6	8	7	8
R	7	7	6	7	8	7	7	6	8	6	8	6	6	7	6	8	7	8	8	6	6	7	6	8	7	8	8
	7	7	7	7	7	8	6	7	7	7	7	6	6	6	6	6	6	6	6	8	8	8	8	8	8	8	8
	7	6	7	8	7	7	7	6	6	8	8	6	7	6	8	6	8	7	8	6	7	6	8	6	8	7	8
	8	8	7	8	9	8	8	7	9	7	9	7	7	8	7	9	8	9	9	7	7	8	7	9	8	9	9
	7	7	7	7	7	8	6	7	7	7	7	6	6	6	6	6	6	6	6	8	8	8	8	8	8	8	8
	8	7	8	9	8	8	8	7	7	9	9	7	8	7	9	7	9	8	9	7	8	7	9	7	9	8	9
	8	8	7	8	9	8	8	7	9	7	9	7	7	8	7	9	8	9	9	7	7	8	7	9	8	9	9
	8	8	8	8	8	9	7	8	8	8	8	7	7	7	7	7	7	7	7	9	9	9	9	9	9	9	9
	8	7	8	9	8	8	8	7	7	9	9	7	8	7	9	7	9	8	9	7	8	7	9	7	9	8	9
	8	8	7	8	9	8	8	7	9	7	9	7	7	8	7	9	8	9	9	7	7	8	7	9	8	9	9
	8	8	8	8	9	7	8	8	7	7	7	7	7	9	9	9	9	9	NA	NA	NA	NA	NA	NA	NA	NA	NA
	8	7	8	9	8	8	7	9	7	8	7	9	9	7	8	7	9	9	NA	NA	NA	NA	NA	NA	NA	NA	NA
	9	9	8	9	9	9	8	8	8	8	9	8	9	8	8	9	8	9	NA	NA	NA	NA	NA	NA	NA	NA	NA
	8	8	8	9	7	8	7	7	7	9	9	9	NA	NA	NA	NA	NA	NA	NA	NA	NA	NA	NA	NA	NA	NA	NA
	9	8	9	9	9	8	8	9	8	8	9	8	NA	NA	NA	NA	NA	NA	NA	NA	NA	NA	NA	NA	NA	NA	NA
	9	9	8	9	9	8	8	8	9	8	8	9	NA	NA	NA	NA	NA	NA	NA	NA	NA	NA	NA	NA	NA	NA	NA
	9	9	9	8	9	8	8	8	NA	NA	NA	NA	NA	NA	NA	NA	NA	NA	NA	NA	NA	NA	NA	NA	NA	NA	NA
	9	8	9	9	8	8	9	8	NA	NA	NA	NA	NA	NA	NA	NA	NA	NA	NA	NA	NA	NA	NA	NA	NA	NA	NA
	9	9	8	9	8	8	8	9	NA	NA	NA	NA	NA	NA	NA	NA	NA	NA	NA	NA	NA	NA	NA	NA	NA	NA	NA

Table A-1 Cont

Ascending Cycle 10m

Mean Detected Pose

P	0	0	0	1	1	1	2	2	2	3	3	3	4	4	4	5	5	5	6	6	6	7	7	7	8	8	8	9
Y	0	0	1	1	1	2	2	2	3	3	3	4	4	4	5	5	5	6	6	6	7	7	7	8	8	8.3	9	8.6
R	0	.97	1	1	2	2	2	3	3	3	4	4	4	5	5	5	6	6	6	7	7	7	8	8	8	9	9	9

Target Pose

	0	0	0	1	1	1	2	2	2	3	3	3	4	4	4	5	5	5	6	6	6	7	7	7	8	8	8	9
	0	0	1	1	1	2	2	2	3	3	3	4	4	4	5	5	5	6	6	6	7	7	7	8	8	8	9	9
	0	1	1	1	2	2	2	3	3	3	4	4	4	5	5	5	6	6	6	7	7	7	8	8	8	9	9	9

Standard Deviation

	0	0	0	0	0	0	0	0	0	0	0	0	0	0	0	0	0	0	0	0	0	0	0	0	0	0	0	0
	0	0	0	0	0	0	0	0	0	0	0	0	0	0	0	0	0	0	0	0	0	0	0	0	0	0.4	0.5	0.5
	0	0.2	0	0	0	0	0	0	0	0	0	0	0	0	0	0	0	0	0	0	0	0	0	0	0	0	0	0

Descending Cycle 10m

Mean Detected Pose

P	9	8	8	8	7	7	7	6	6	6	5	5	5	4	4	4	3	3	3	2	2	2	1	1	1	0	0	0
Y	8.4	8	9	8	8	7	7	7	6	6	6	5	5	5	4	4	4	3	3	3	2	2	2	1	1	1	1	0	0
R	9	9	9	8	8	8	7	7	7	6	6	6	5	5	5	4	4	4	3	3	3	2	2	2	1	1	1	0

Target Pose

	9	8	8	8	7	7	7	6	6	6	5	5	5	4	4	4	3	3	3	2	2	2	1	1	1	0	0	0
	9	9	8	8	8	7	7	7	6	6	6	5	5	5	4	4	4	3	3	3	2	2	2	1	1	1	0	0
	9	9	9	8	8	8	7	7	7	6	6	6	5	5	5	4	4	4	3	3	3	2	2	2	1	1	1	0

Standard Deviation

	0	0	0	0	0	0	0	0	0	0	0	0	0	0	0	0	0	0	0	0	0	0	0	0	0	0	0	0
	0.5	0.5	0.5	0	0	0	0	0	0	0	0	0	0	0	0	0	0	0	0	0	0	0	0	0	0	0	0	0
	0	0	0	0	0	0	0	0	0	0	0	0	0	0	0	0	0	0	0	0	0	0	0	0	0	0	0	0

Table A- 2 Ascending and descending detected poses for 10m alignment plane

131

Ascending Cycle 50m

Mean Detected Pose

P	0	0	0	1	1	1	2	2	2	3	3	3	4	4	4	5	5	5	6	6	6	7	7	7	8	8	8	9
Y	0	0	1	1	1	2	2	2	3	3	3	4	4	4	5	5	5	6	6	6	7	7	7	8	8	8.4	8.3	8.6
R	0	1	1	1	2	2	2	3	3	3	4	4	4	5	5	5	6	6	6	7	7	7	8	8	8	9	9	9

Target Pose

	0	0	0	1	1	1	2	2	2	3	3	3	4	4	4	5	5	5	6	6	6	7	7	7	8	8	8	9
	0	0	1	1	1	2	2	2	3	3	3	4	4	4	5	5	5	6	6	6	7	7	7	8	8	8	9	9
	0	1	1	1	2	2	2	3	3	3	4	4	4	5	5	5	6	6	6	7	7	7	8	8	8	9	9	9

Standard Deviation

	0	0	0	0	0	0	0	0	0	0	0	0	0	0	0	0	0	0	0	0	0	0	0	0	0	0	0	0
	0	0	0	0	0	0	0	0	0	0	0	0	0	0	0	0	0	0	0	0	0	0	0	0	0	0.5	0.5	0.5
	0	0	0	0	0	0	0	0	0	0	0	0	0	0	0	0	0	0	0	0	0	0	0	0	0	0	0	0

Descending Cycle 50m

Mean Detected Pose

P	9	8	8	8	7	7	7	6	6	6	5	5	5	4	4	4	3	3	3	2	2	2	1	1	1	0	0	0
Y	8.6	8.4	8	8	8	7	7	7	6	6	6	5	5	5	4	4	4	3	3	3	2	2	2	1	1	1	0	0
R	9	9	9	8	8	8	7	7	7	6	6	6	5	5	5	4	4	4	3	3	3	2	2	2	1	1	1	0

Target Pose

	9	8	8	8	7	7	7	6	6	6	5	5	5	4	4	4	3	3	3	2	2	2	1	1	1	0	0	0
	9	9	8	8	8	7	7	7	6	6	6	5	5	5	4	4	4	3	3	3	2	2	2	1	1	1	0	0
	9	9	9	8	8	8	7	7	7	6	6	6	5	5	5	4	4	4	3	3	3	2	2	2	1	1	1	0

Standard Deviation

	0	0	0	0	0	0	0	0	0	0	0	0	0	0	0	0	0	0	0	0	0	0	0	0	0	0	0	0
	0.5	0.5	0.5	0	0	0	0	0	0	0	0	0	0	0	0	0	0	0	0	0	0	0	0	0	0	0	0	0
	0	0	0	0	0	0	0	0	0	0	0	0	0	0	0	0	0	0	0	0	0	0	0	0	0	0	0	0

Table A- 3 Ascending and descending detected poses for 50m alignment plane

Ascending Cycle 100m

Mean Detected Pose

P	0	0	0	1	1	1	2	2	2	3	3	3	4	4	4	5	5	5	6	6	6	7	7	7	8	8	8	9
Y	0	0	1	1	1	2	2	2	3	3	3	4	4	4	5	5	5	6	6	6	7	7	7	8	8	8.4	8.5	8.6
R	0	1	1	1	2	2	2	3	3	3	4	4	4	5	5	5	6	6	6	7	7	7	8	8	8	9	9	9

Target Pose

	0	0	0	1	1	1	2	2	2	3	3	3	4	4	4	5	5	5	6	6	6	7	7	7	8	8	8	9
	0	0	1	1	1	2	2	2	3	3	3	4	4	4	5	5	5	6	6	6	7	7	7	8	8	8	9	9
	0	1	1	1	2	2	2	3	3	3	4	4	4	5	5	5	6	6	6	7	7	7	8	8	8	9	9	9

Standard Deviation

	0	0	0	0	0	0	0	0	0	0	0	0	0	0	0	0	0	0	0	0	0	0	0	0	0	0	0	0
	0	0	0	0	0	0	0	0	0	0	0	0	0	0	0	0	0	0	0	0	0	0	0	0	0	0.5	0.5	0.5
	0	0	0	0	0	0	0	0	0	0	0	0	0	0	0	0	0	0	0	0	0	0	0	0	0	0	0	0

Descending Cycle 100m

Mean Detected Pose

P	9	8	8	8	7	7	7	6	6	6	5	5	5	4	4	4	3	3	3	2	2	2	1	1	1	0	0	0
Y	8.5	8.5	8.5	8	8	7	7	7	6	6	6	5	5	5	4	4	4	3	3	3	2	2	2	1	1	1	0	0
R	9	9	9	8	8	8	7	7	7	6	6	6	5	5	5	4	4	4	3	3	3	2	2	2	1	1	1	0

Target Pose

	9	8	8	8	7	7	7	6	6	6	5	5	5	4	4	4	3	3	3	2	2	2	1	1	1	0	0	0
	9	9	8	8	8	7	7	7	6	6	6	5	5	5	4	4	4	3	3	3	2	2	2	1	1	1	0	0
	9	9	9	8	8	8	7	7	7	6	6	6	5	5	5	4	4	4	3	3	3	2	2	2	1	1	1	0

Standard Deviation

	0	0	0	0	0	0	0	0	0	0	0	0	0	0	0	0	0	0	0	0	0	0	0	0	0	0	0	0
	0.5	0.5	0.5	0	0	0	0	0	0	0	0	0	0	0	0	0	0	0	0	0	0	0	0	0	0	0	0	0
	0	0	0	0	0	0	0	0	0	0	0	0	0	0	0	0	0	0	0	0	0	0	0	0	0	0	0	0

Table A- 4 Ascending and descending detected poses for 100m alignment plane

Works Cited

1. Beitrage zur Theorie des Mikroskops und der Mikroskopischen wahrnehmung. Abbe, E. 1873, Archiv. Microskopische Anat., Vol. 9, pp. 413-468.

2. Porter, A. B. On the diffraction theory of microscope vision. Phil. Mag. 6, 1906, Vol. 11, 6, p. 154.

3. Vander Lugt, A. B. Signal detection by complex spatial filtering. Institute of Science and Technology, University of Michigan. Ann Arbor, MI : s.n., 1963. Technical Report.

4. Arfken, G. Math Methods for Physicists. Orlando, FL : Academic Press, 2005.

5. Goodman, J. W. Introduction to Fourier Optics. New York : McGraw-Hill, 1996.

6. Two Dimensional Spatial Light Modulators: A tutorial. Neff, John A., Athale, Ravindra A. and Lee, Sing H. s.l. : IEEE, 1990. Proceedings of the IEEE. pp. 826-855.

7. Chigrinov, V. G. Liquid Crystal Devices: Physics and Applications. s.l. : Artech House Publishers, 1999.

8. Saleh, B.E.A. and Teich, M.C. Fundamentals of Photonics. New York : John Wiley & Sons, 1991.

9. Chigrinov, V. G. and Blinov, L. M. Electro optic Effects in Liquid Crystal Materials. New York : Springer, 1996.

10. Secretary, Office of the Press. The White House. Whitehouse. [Online] January 14, 2004. [Cited: 5 12, 2008.] Office of the Press Secretary.

11. Correlation techniques as applied to pose estimation in space station docking. Johnson, Kristina M., Juday, Richard D. and Monroe Jr, Stanley E. s.l. : Proceedings of SPIE, 2002. Signal and Data Processing of Small Targets. Vol. Vol. 4728, pp. 218-229.

12. Correlation-Based Target Detection for the Navy's SHARP Sensor Suite. Pankaj, Topiwala and Casasent, David. [ed.] Firooz A. Sadjadi. Bellingham : Proceedings of SPIE, 2004. Automatic Target Recognition XIV. Vol. 5426.

13. Three-dimensional attitude estimation and tracking by multi- correlation technique with normalized optimal trade-off filters . Tonda, S. and Refregier, P. USA : Proc. SPIE, 1996. Vol. 2751, pp. 207-18.

14. Minimum average correlation energy filters. Mahalanobis, A., Kumar, B.V.K. Vijaya and Casasent, and D. 5, s.l. : Applied Optics, 1987, Vol. 26, pp. 3633-40.

15. Estimating object rotation and scale using correlation filters. B.V.K. Vijaya Kumar, A. Lee, and J. Connelly. 5, s.l. : Optical Engineering, 1989, Vol. 28, pp. 474-481.

16. K. A. Al-Ghoneim and B.V.K. Vijaya Kumar, "Combining focused mace filters for target detection," submitted to Automatic Target Recognition Conference, Proc. SPIE -Int. Soc. Opt. Eng. (USA), 1998.

17. J. Homer and H. Caulfield, "Parameter extraction by holographic filtering," Applied Optics 21(9), pp. 1599—601, 1 May 1982.

18. G. Ravichandran and D. Casasent, "Minimum noise and correlation energy optical correlation filter," Applied Optics 31(11), pp. 1823—33, 10 April 1992.

19. M. Bennett and P. Rajan, "Comparison of five types of synthetic estimation filters for pose parameter estimation," in Proc. SPIE - mt. Soc. Opt. Eng. (USA), vol. 1702, pp. 121—31, 1992.

20. L. Hassebrook, M. Lhamon, M. Wang, and J. Chatterjee, "Distortion parameter estimation using complex distortion- invariant correlation filter bank responses," in Proc. SPIE -mt. Soc. Opt. Eng. (USA), vol. 2490, pp. 64—76, SPIE-Int. Soc. Opt. Eng, 1995.

21. L. Hassebrook, M. Rahmati, and B.V.K. Vijaya Kumar, "Hybrid composite filters for general distortion-invariant optical pattern recognition," in Proc. SPIE - mt. Soc. Opt. Eng. (USA), vol. 1701, pp. 217—28, 1992.

22. S. Tonda and P. Refregier, "Three-dimensional attitude estimation and tracking by multi- correlation technique with normalized optimal trade-off filters," in Proc. SPIE - mnt. Soc. Opt. Eng. (USA), vol. 2751, pp. 207—18, SPIE-Int. Soc. Opt. Eng, 1996.

23. Tonda and P. Refregier, "Three-dimensional attitude estimation and tracking with linear normalized optimal filtering," Optical Engineering 36(4), pp. 1145—51, April 1997.

24. B.V.K. Vijaya Kumar, A. Lee, and J. Connelly, "Estimating object rotation and scale using correlation filters," Optical Engineering 28(5), pp. 474—81, May 1989.

25. Kumar, Vijaya B.V.K., Mahalanobis, A., Juday, Richard D., Correlation Pattern Recognition. New York : Cambridge University Press, 2005.

26. T-H. Chao, Y. Park, and G. Reyes, "High-speed camera-sized optical wavelet processor," SPIE 3073, pp. 194-200, 1997.

27. T-H. Chao, G. Reyes, andY. Park, "Grayscale optical correlator," SPIE 3386, pp. 60-64, 1998.

28. T-H. Chao, G. Reyes, and H. Zhou, "Automatic target recognition field demonstration using a grayscale optical correlator," SPIE 3715. pp. 399-406. 1999.

29. H. Zhou and T-H Chao. "MACH Filter Synthesizing for Detecting Targets in Cluttered Environment for Grayscale Optical Correlator, "SPIE 3715, pp. 394-398. 1999.

30. V. Kumar, "Tutorial survey of composite filter designs for optical correlators," Appl. Opt. 31, 4773–4801 (1992).

31. A. Castro, Y. Frauel, E. Tepichín, and B. Javidi, "Pose Estimation from a Two-Dimensional View by Use of Composite Correlation Filters and Neural Networks," Appl. Opt. **42**, 5882-5890 (2003)

32. Richard D. Juday, "Optimal realizable filters and the minimum Euclidean distance principle", Applied Optics 32, 5100-5111 (10September 1993).

33. Minimum Euclidean distance optimal filter (MEDOF): version 2.0, R. Shane Barton and Richard D. Juday, Proc. SPIE 2490, 14 (1995), DOI:10.1117/12.205771

34. D. Psaltis, E. G. Paek, and S. S. Venkatesh, "Optical image correlation with a binary spatial light modulator",Opt. Eng. 23, 698-704, 1984.

35. J. L. Horner, and J. Leger, "Pattern recognition with binary phase-only filters", Appl. Opt., 24, 609-611, 1985.

36. R. R. Kallman, "Optimal Low-Noise Phase-Only and Binary Phase-Only Optical Correlation Filters for Threshold Detectors," Appl. Opt. 25, 4216 (1986).

37. J. L. Horner and H. 0. Bartelt, "Two-Bit Correlation," Appl. Opt. 24, 2889 (1985).

38. W. E. Ross, D. Psaltis, and R. H. Anderson, "Two-dimensional magneto-optic spatial light modulator for signal processing," Optical Engineering, 22, 485—490 (1983).

39. D. L. Flannery, J. S. Loomis, and M. E. Milkovich, "Design elements of binary phase-only correlation filters," Applied Optics, 27, 4231—4235 (1988).

40. D. Casasent, "Unified synthetic discriminant function computational formulation," Appl. Opt. **23**, 1620-1627 (1984)

41. Fisher, J.W., III; Principe, J.C., "Formulation of the MACE filter as a linear associative memory," Neural Networks, 1994. IEEE World Congress on Computational Intelligence., 1994 IEEE International Conference on , vol.5, no., pp.2934-2937 vol.5, 27 Jun-2 Jul 1994

42. H. Zhou, T. S. Chao, "MACH filter synthesizing for detecting targets in cluttered environment for gray-scale optical correlator," in Optical Pattern Recognition X, D. P. Casasent and T.-H. Chao, eds. SPIE 3715, 394–398 (1999).

43. A. Castro, Y. Frauel, E. Tepichín, and B. Javidi, "Pose Estimation from a Two-Dimensional View by Use of Composite Correlation Filters and Neural Networks," Appl. Opt. **42**, 5882-5890 (2003)

44. Empirical performance of binary phase-only synthetic discriminant functions. Gary W. Carhart, Bret F. Draayer, Paul A. Billings, and Michael K. Giles, Proc. SPIE 1564, 348 (1991), DOI:10.1117/12.49724

45. Practical filter dynamic range compression for grayscale optical correlator using bipolar-amplitude SLM. Hanying Zhou, Tien-Hsin Chao, and George F. Reyes, Proc. SPIE 4043, 90 (2000)

46. Serati, Steve. *High Speed Multi-level Spatial Light Modulator*. Lafayette : Boulder

Nonlinear Systems.